Doctoral Dissertation

Doctoral Program in Physics (35.th cycle)

Functional patterning of dielectric multilayers supporting Bloch Surfaces Waves

Niccolò Marcucci

* * * * *

Supervisors

Prof. Emiliano Descrovi, Supervisor

Prof. Antonio Gliozzi, Co-supervisor

Prof. Fabrizio Giorgis, Co-supervisor

Doctoral examination committee

Prof. Alessandro Belardini, Referee, University of Rome, La Sapienza

Prof. Carlo Forestiere, Referee University of Napoli, Federico II

Dr. Silvia Soria, National Research Council, CNR IFAC

Dr. Paolo Traina, National Institute of Metrology, INRIM

Prof. Francesco Raffa, Politecnico di Torino

Politecnico di Torino

18-09-2023

I hereby declare that, the contents and organisation of this dissertation constitute my own original work and does not compromise in any way the rights of third parties, including those relating to the security of personal data.

. . . . . .

Niccolò Marcucci

Turin, 18-09-2023

Summary

In recent years, there has been a growing interest in the use of photonic devices, partly due to the physical limitations that prevent further size reduction of electronic integrated circuits. This has led to the exploration of different physical phenomena/mechanisms that can be exploited in similar ways. Dielectric multilayers hosting Bloch surface waves (BSW) have emerged as a promising platform for nanophotonic devices due to their unique characteristics, which make them suitable for creating optical sensors and bidimensional photonic devices. Photo-responsive polymers have also gained interest in the manipulation of light in nanophotonic structures, as they have demonstrated their capabilities in responding to light stimuli in various ways [1–5]. They are, therefore, a promising platform for manipulating electromagnetic radiation.

Optical angular momentum is an interesting property of light that has found numerous applications in photonic systems. Angular momentum can be found either in the form of spin or in the form of Orbital Angular Momentum (OAM). In recent years, many nanophotonic devices have been developed to interact with and manipulate angular momentum [6–10]. However, it is becoming increasingly important to engineer photon sources directly[11, 12], especially in quantum applications where Single Photon Emitters (SPEs) are necessary [6–10]. Creating and engineering SPEs can be challenging, but recent research on two-dimensional materials such as Transition Metal Dichalcogenides (TMDs) and hexagonal Boron Nitride (h-BN) has shown promise. TMDs like MoS_2 and WS_2 have shown great reliability in

generating SPEs, but they mainly operate at very low temperatures [13–15]. Recent research on h-BN has shown that it is capable of overcoming this issue, and SPEs can be engineered by inducing or activating lattice defects in the material, despite its very high band-gap, which results in almost null photo-luminescence at room temperature [16–22].

In the aforementioned context, the aim of this project was to explore the possibilities offered by BSW-driven nano-photonic systems to manipulate light in new, unprecedented ways. The focus of this research is on the study of all-dielectric structures that enable subwavelength control of the spatial propagation of electromagnetic waves. This thesis is divided into three main activities presented in three different chapters, namely Chapters 2, 3, and 4.

One activity was aimed at exploring the use of photo-responsive polymers to control the resonance inside surface nanocavities. The optical anisotropy induced by polarized radiation was used to optically tune the resonance frequency of a circular nanocavity. This activity is detailed in Chapter 2.

A second part of this project is focused on the exploitation of BSW platforms for the manipulation of light emitted by dipole-like sources, with the goal of imparting an arbitrary angular momentum to the generated field. Specifically, we designed particular metasurfaces to generate circularly polarized vortex beams from dipole-like sources. This activity is reported in Chapter 3.

To test these platforms with actual dipole-like sources, our focus was directed towards researching reliable single photon emitter sources (SPE) that could be embedded into the designed photonic structures. We explored the use of hexagonal Boron Nitride as a means of providing SPEs by inducing defects on the crystal using localized focused ion beam damage. This activity is reported in Chapter 4.

In Chapter 1 instead, the theoretical and technical background useful for the understanding of the numerical and experimental methods utilised in this thesis is presented. In particular, the focus is placed on the mathematical implications of

Fourier optics, heavily exploited in the experiments, and on the description of the numerical methods utilised for modeling the structures.

Contents

List of Figures

Chapter 1

Theoretical framework

The opening chapter of this thesis proposes a comprehensive review of the theoretical background upon which it is founded. It begins with a brief introduction to Maxwell's equations, which form the cornerstone of Fourier Optics. This allows for the presentation of some of its most interesting results that will be utilized throughout this work, including the Rayleigh-Sommerfeld propagation formula and diffraction from periodic planar structures. Following this, the chapter provides a short description of the angular momentum properties of light. Subsequently, a brief analysis on photonic crystals is presented, with particular emphasis on one-dimensional photonic crystals. The behavior of these devices when approximated with finite-sized dielectric multilayers is described in detail. These dielectric structures are shown to be capable of hosting Bloch surface waves, which serve as the foundational platform for the activity of this thesis. Finally, in a concluding section, the numerical methods utilized to study and design the devices proposed in the following chapters are presented. This includes a self-implemented version of the Transfer Matrix method, along with an explanation of the basic tools utilized for finite difference time domain simulations.

1.1 From Maxwell to D'Alambèrt

Starting from classical Electromagnetism, the electric $\vec{E}$ and magnetic $\vec{B}$ fields can be related to each other by means of Maxwell's equations:

$$\begin{aligned} \nabla \cdot \vec{D} &= \rho, \\ \nabla \cdot \vec{B} &= 0, \\ \nabla \wedge \vec{E} &= -\frac{\partial \vec{B}}{\partial t}, \\ \nabla \wedge \vec{H} &= \vec{j} + \frac{\partial \vec{D}}{\partial t}, \end{aligned} \tag{1.1}$$

where $\vec{D} = \epsilon_0 \epsilon_r \vec{E}$, $B = \mu_0 \mu_r \cdot \vec{H}$ and ρ is the charge density. $\vec{j}$ is the current density, related to the electric and magnetic field by means of the conductivity σ and the charges velocity $\vec{v}$: $\vec{j} = \sigma(\vec{E} + \vec{v} \wedge \vec{B})$; with the contribution of $\vec{B}$ typically negligible, due to the low velocity of the charges involved. The relative dielectric and magnetic constants can depend on the direction of the electric and magnetic fields. In these cases the material is said to be anisotropic, and the two constants are expressed in a tensorial form. While, especially in optics, most materials have a scalar μ_r and equal to 1, it is not uncommon to see a tensorial dielectric constant:

$$\boldsymbol{\epsilon}_r = \begin{bmatrix} \epsilon_{11} & .. & .. \\ : & . & : \\ : & .. & \epsilon_{33} \end{bmatrix}. \tag{1.2}$$

The shape of the matrix obviously depends on the orientation of the material with respect to the system of reference (thus the electric field), but when the anisotropy is aligned with the base vectors of the system of reference, the matrix takes a diagonal form. Anisotropic optical materials are called *birefringent* and they have may interesting properties when interacting with polarised radiation.

Maxwell's equations describe the interconnectedness of magnetic and electric fields in various ways, making it possible to combine them to find a relation between the temporal and spatial variations of either field, leading to a wave equation. To derive the wave equation, one can manipulate the equations by taking the curl of the curl of the electric field:

$$\nabla \wedge (\nabla \wedge \vec{E}) = \nabla \wedge -\frac{\partial \vec{B}}{\partial t}. \tag{1.3}$$

Since the curl operator does not depend on time and using the property of algebraic vectors which says that $\vec{A} \wedge (\vec{B} \wedge \vec{C}) = \vec{B}(\vec{A} \cdot \vec{C}) + (\vec{A} \cdot \vec{B})\vec{C}$, we can rewrite (1.3) as:

$$\nabla(\nabla \cdot \vec{E}) - \nabla^2 \vec{E} = -\mu_0 \mu_r \frac{\partial}{\partial t}\big(\vec{j} + \frac{\partial \vec{D}}{\partial t}\big).$$

In a homogeneous medium with no spatial charges, where the relative permittivity is constant, the divergence of the electric displacement ($\vec{D}$) is zero, and therefore the divergence of the electric field ($\vec{E}$) is also zero[1]. Expressing both $\vec{j}$ and $\vec{D}$ as a function of $\vec{E}$ we can write:

$$\nabla^2 \vec{E} = \mu_0 \mu_r \sigma \frac{\partial \vec{E}}{\partial t} + \mu_0 \mu_r \epsilon_0 \boldsymbol{\epsilon}_r \frac{\partial^2 \vec{E}}{\partial t^2}. \tag{1.4}$$

The obtained result can be considered a generalized wave equation, with the term in σ acting as a dissipative term and behaving as a sort of viscosity. But considering a non-conductive medium we can neglect the additional term, finally obtaining the electromagnetic equivalent of the D'Alambèrt equation:

$$\nabla^2 \vec{E} = \frac{\mu_r \boldsymbol{\epsilon}_r}{c^2} \frac{\partial^2 \vec{E}}{\partial t^2}, \tag{1.5}$$

[1] In mathematical terms, $\nabla \cdot \vec{D} = 0 \Rightarrow \nabla \cdot (\boldsymbol{\epsilon}\vec{E}) = (\nabla \boldsymbol{\epsilon}) \cdot \vec{E} + \boldsymbol{\epsilon}(\nabla \cdot \vec{E}) = 0$. Here, $\nabla \boldsymbol{\epsilon}$ denotes the generalized divergence operation applied to the permittivity tensor. While the permittivity tensor would describe a tensor field if it were dependent on space coordinates, since it is constant, its divergence is null. Thus, we can conclude that $\nabla \cdot \vec{D} = 0 \Rightarrow \nabla \cdot \vec{E} = 0$.

where $c^2 = 1/(\mu_0\epsilon_0)$. This wave equation actually represent a set of three equations where the vectorial components are related to each other. When we consider an isotropic material instead we can define the refractive index $n = \sqrt{\mu_r\epsilon_r}$ and consider Eq. (1.5) as set of three independent equations.

In order to simplify the analysis, from this point forward we will consider only isotropic materials. In such case, it is possible to find solutions to the D'Alambèrt equation in the form of a product of a space dependent component and a time dependent component.

$$\vec{E}(\vec{r},t) = \begin{pmatrix} E_{0x} \\ E_{oy} \\ E_{0z} \end{pmatrix} U(\vec{r})F(t). \tag{1.6}$$

where $\vec{r}$ is a general position in space. In order to solve differential equations by means of Fourier analysis, one can assume the time dependence to be harmonic $F(t) = e^{-i\omega t}$, that simplifies Eq. (1.5) into a space only equation:

$$\nabla^2 U(\vec{r}) = \frac{n^2}{c^2}(-\omega^2)U(\vec{r}). \tag{1.7}$$

Also for the $U(r)$ we may use an harmonic approach, but, thanks to its dependence on three coordinates, there a multiple types of solutions which describe different types of waves. The most common forms are plane waves, cylindrical waves and spherical waves.

Plane waves

The easiest solution for the wave equation is found in the form of plane waves.

$$U(\vec{r}) = e^{i\vec{k}\cdot\vec{r}}. \tag{1.8}$$

Here the harmonic dependence is given by the wavevector $\vec{k}$, that represent a form of spatial frequency. They are called plane waves because the scalar product between the wavevector and the position vector ensures the function to assume the same value for all the points laying on a plane orthogonal to $\vec{k}$. In facts, if

$$\vec{k} \cdot \vec{r'} = \vec{k} \cdot \vec{r''} \Rightarrow \vec{k} \cdot \vec{\Delta r} = 0,$$

meaning that $\vec{k} \perp \vec{\Delta r}$. These waves have therefore a planar wavefront and propagate in the direction given by $\vec{k}$.

Spherical waves

A nice solution to the wave equation in spherical coordinates is provided by spherical waves.

$$U(\vec{r}) = \frac{1}{r} e^{ikr}. \tag{1.9}$$

where the harmonic term depends on the product between the modulus of the wavevector $k = |\vec{k}|$ and the distance from the origin $r = |\vec{r}|$. This solution is valid only for scalar fields and, in such case, it can actually be considered as a one dimensional wave. For vector fields like the EM field, the amplitude of the three components needs to be dependent on the two angular coordinates in order to avoid singularities in the field:

$$\begin{aligned} E_r &= 0, \\ E_\phi &= f(\phi, \theta), \\ E_\theta &= g(\phi, \theta). \end{aligned}$$

Cylindrical waves

Solution of the wave equation for cylindrical waves are slightly more complex and require the involvement of complex mathematical functions, such as Bessel, Henkel or Neumann functions. The general expression for cylindrical waves can be written as:

$$U(r, \phi, z) = h_m(kr)e^{i(kz-m\phi)}, \tag{1.10}$$

with m being the azimuthal modal number and $h_m(kr)$ being, for instance, a Bessel function of the first kind. Although complex, far from the origin these solutions can all be approximated as $h_m(kr) \approx\propto \frac{1}{\sqrt{r}}e^{ikr}$.

1.1.1 The photon dispersion

Considering a solution to the wave equation in Cartesian coordinates, i.e plane waves, we can insert the proposed form into (1.7) and find a relation between the spatial and temporal frequencies. We can in fact write the Laplacian of $U(\vec{r})$:

$$\nabla^2 U(\vec{r}) = \frac{\partial^2 e^{i\vec{k}\vec{r}}}{\partial x^2} + \frac{\partial^2 e^{i\vec{k}\vec{r}}}{\partial y^2} + \frac{\partial^2 e^{i\vec{k}\vec{r}}}{\partial z^2} = -(k_x^2 + k_y^2 + k_z^2)U(\vec{r}). \tag{1.11}$$

We therefore substitute into the wave equation and obtain:

$$-k^2\vec{U}(\vec{r}) = -\frac{n^2}{c^2}\omega^2\vec{U}(\vec{r})$$

$$k = \frac{n}{c}\omega. \tag{1.12}$$

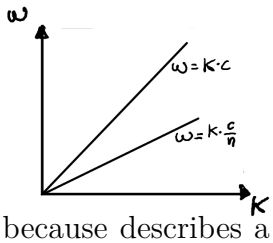

That relates the speed of an electromagnetic wave to its temporal and spatial frequency. This is very interesting because describes a dispersion relation for photons that is linear, contrary to the one of electrons in free space, which is parabolic.

Since the temporal angular frequency is defined as $\omega = 2\pi/T$, and the wavelength as the wave speed times the temporal period $\lambda = (c/n)T$, the wave vector modulus can be considered a spatial angular frequency, expressed as

$$k = \frac{2\pi}{\lambda}.$$

1.2 Fourier Optics

It was mentioned that for an isotropic material the wave equation takes the form (1.7), to which plane waves are an allowed solution. Following the result proposed by the dispersion relation for plane waves, we may define the wavevector k as in (1.12) and rewrite the wave equation in the well-known form of Helmholtz equation:

$$\nabla^2 U(\vec{r}) + k^2 U(\vec{r}) = 0. \tag{1.13}$$

The Helmholtz equation is valid for a generic shape of the field $U(r) = U(x, y, z)$, but, knowing that for a plane wave $\vec{k}$ describes the direction of propagation of a wave, we may tray to decompose U into a combination of plane waves. Mathematically, this results in a simple Fourier transform of the field. This concept is at the foundation of Fourier optics, which provides a mathematical model for the propagation of an electromagnetic wave. Specifically, it offers a mean to describe a wave along a particular propagation direction, based on the field's knowledge in a given plane orthogonal to such direction. In other words, it provides a method for knowing $U(x, y, z)$ starting form $U(x, y,0)$.

In order to perform a Fourier transform (F.t.) it is necessary to define the base for the Fourier space. One may try to directly write the field U a sum of plane waves, where each plane wave is described by the wavevector $\vec{k}$ and an amplitude $A_{\vec{k}}$.

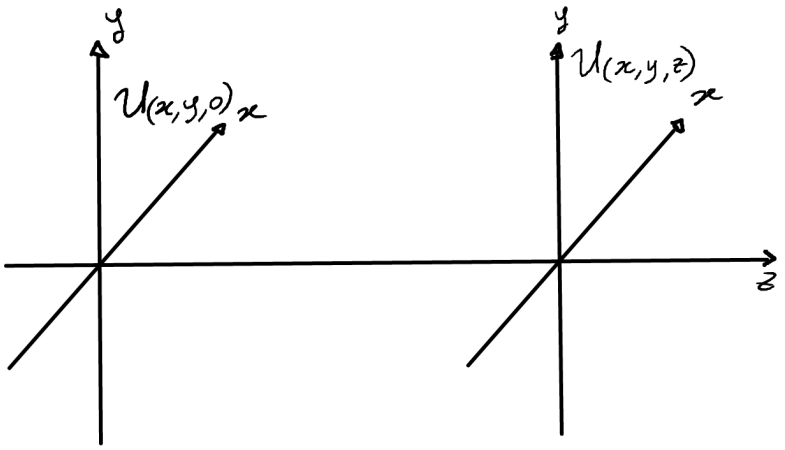

Figure 1.1: Graphical representation of the plane (on the left) where we know the expression of the field $U(x, y,0)$, and the plane where the field will propagate to.

$$U(\vec{r}) = \iiint_{-\infty}^{+\infty} A_{\vec{k}} e^{i\vec{k}\cdot\vec{r}} d\vec{k}; \qquad \vec{r} = (x, y, z), \quad \vec{k} = (k_x, k_y, k_z).$$

Assuming propagation is in the $z-$direction and the field U to be known at a given position $z = z'$, the term $k_z z$ can be considered as a constant phase term, and the integral over k_z can be ignored. The integral above resembles already a Fourier transform, with a base $e^{i(k_x x + k_y y)}$. To write the F.t. in a more familiar way we can consider

$$k_i = 2\pi f_i,$$

where f_i is referred to as angular frequency.

The decomposition of the field in plane waves would then be written as

$$U(x, y, z = z') = \iint_{-\infty}^{+\infty} A(f_x, f_y, z') e^{+i2\pi(f_x x + f_y y)} df_x df_y. \tag{1.14}$$

where $A(f_x, f_y, z')$ is the amplitude of each plane wave at position $z = z'$ and is called **angular spectrum**. This integral is now mathematically identical to an

inverse F.t., therefore the angular spectrum can be computed as:

$$A(f_x, f_y, z') = \iint_{-\infty}^{+\infty} U(x, y, z') e^{-i2\pi(f_x x + f_y y)} dxdy = \mathcal{F}\{U\} \tag{1.15}$$

The extremes of integration will be neglected from now on, unless different from ∞.

Another way of referring to the angular frequencies is by means of direction cosines (α, β, γ), that describe $\vec{k}$ as

$$\vec{k} = \frac{2\pi}{\lambda}(\alpha, \beta, \gamma), \tag{1.16}$$

where is always true that $\gamma = \sqrt{1 - \alpha^2 - \beta^2}$. Therefore the angular frequencies will be described as

$$f_x = \frac{\alpha}{\lambda}, \quad f_y = \frac{\beta}{\lambda}. \tag{1.17}$$

1.2.1 Propagation of the Fourier field

In order to understand how to propagate the field when performing this Fourier decomposition, it is important to first understand its effect on the wave equation. To do so one can simply insert the decomposition of (1.14) into the Helmholtz equation (1.13) and, after very few manipulations, find a new equation on the angular spectrum:

$$\frac{d^2 A_f(z)}{dz^2} + k^2 \left(1 - \alpha^2 - \beta^2\right) A = 0. \tag{1.18}$$

where $A_f(z)$ is just a more compact way to write $A(f_x, f_y, z)$. Solutions for this equation are in the form $A_0 e^{+i\alpha} + A_1 e^{-i\alpha}$ but $A_1 = 0$, since we are considering only propagation in one direction.

$$A_f(z) = A_0 e^{+ik\sqrt{(1-\alpha^2-\beta^2)}z}.$$

By substituting into the general solution, we get that $A_0 = A_f(0)$ and, since the field is known at the given position $z = z'$, one can simply choose the coordinate system so that $z' = 0$ and write:

$$A(f_x, f_y, z) = A(f_x, f_y,0)e^{+i\frac{2\pi}{\lambda}\gamma z}. \tag{1.19}$$

It should be noted that if $\alpha^2 + \beta^2 < 1$ then γ is real and the angular spectrum propagates normally, but if $\alpha^2 + \beta^2 > 1$ then γ is imaginary and the propagator becomes a decaying exponential, which is the characteristic description of an evanescent wave. For these values of the direction cosines, the wave would not actually be propagating in the z direction, hence they need to be excluded from the inverse F.t. when computing the field U at the coordinate z. Mathematically, this can be expressed by means of a *circ* function

$$circ(x) = \begin{cases} 1, & if \quad x < 1 \\ 0 & else, \end{cases}$$

Therefore writing the field as

$$U(x, y, z) = \iint circ(\alpha^2 + \beta^2)A(f_x, f_y, z)e^{+i2\pi(f_x x + f_y y)}df_x df_y. \tag{1.20}$$

1.2.2 Propagation of the wavefront

From Fourier analysis, it is known that a product in Fourier space can be converted into a convolution in the direct space (and vice versa):

$$F(\omega) = G(\omega) \cdot H(\omega), \quad \Rightarrow \quad f(x) = g(x) \otimes h(x) = \int g(x')h(x - x')dx,$$

with F,G, and H as the F.t. of the functions f,g and h respectively. Since in (1.19) we wrote that the angular spectrum in z can be computed as the product of two

functions, the angular spectrum in $z = 0$ and a propagator, we could also write the field $U(x, y, z)$ as a convolution between the field in $z = 0$ and the inverse F.t. of the propagator.

$$h(x, y, z) = \mathcal{F}^{-1}\left\{circ(\alpha^2 + \beta^2)e^{-i\frac{2\pi}{\lambda}\gamma z}\right\} = -\frac{i}{\lambda}\frac{e^{ikr}}{r^2}z, \tag{1.21}$$

where $r = \sqrt{x^2 + y^2 + z^2}$ and α, β and γ can be related to f_x, f_y and k by the usual formulas. Therefore, the final field can be written as

$$U(x, y, z) = U(x, y,0) \otimes h(x, y, z) = \frac{1}{i\lambda}\iint U(x', y',0)\frac{z}{r'}\frac{e^{ikr'}}{r'}dx'dy' \tag{1.22}$$

with $r' = \sqrt{(x - x')^2 + (y - y')^2 + z^2}$. This equation is the famous Rayleigh-Sommerfeld formula for propagation. The integral can be interpreted as a sum of spherical waves starting from the plane at $z = 0$ and reaching z. The term z/r' would represent a cosine projection of the field leaving from a point source in the origin plane, and propagating with a polarization tangential to the spherical wave wavefront.

To summarize, the mathematical propagation of the field can be computed as:

$$\begin{array}{ccc} U(x, y,0) & \xrightarrow{\mathcal{F}} & A_0 = A(f_x, f_y,0) \\ \downarrow_{\text{Rayleigh}} & & \downarrow \\ U(x, y, z) & \xleftarrow{\mathcal{F}^{-1}} & A = A_0 e^{+ik_z z} \end{array}$$

1.2.3 Bragg's Law for periodic objects

When a propagating field meets and object in space, the field after the object can be obtained by assigning a transfer function $t(x, y)$ to the object, such that

$$U(x, y, z_{after}) = U(x, y, z_{before}) \cdot t(x, y). \tag{1.23}$$

Considering the problem in Fourier space, the product becomes a convolution with the Fourier transform of the transfer function:

$$A(f_x, f_y, z_{after}) = A(f_x, f_y, z_{before}) \otimes \mathcal{F}\{t\}(f_x, f_y). \tag{1.24}$$

This very simple considerations on the transfer function of an object becomes particularly relevant when dealing with periodic objects. Indeed, the Fourier transform of a periodic object is reduced to a Fourier series, which can be expressed mathematically as a sum of Dirac delta functions:

$$\mathcal{F}\{t\}(f_x) = \sum_{m=-\infty}^{\infty} a_m \delta_{m f_0}. \tag{1.25}$$

where $f_0 = 1/\Lambda_t$ is the frequency of the fundamental harmonic (given by the inverse of the period of the object) and $m f_0$ is the frequency of the m^{th} harmonic. For simplicity, in the following the object is assumed to be periodic only in the $x-$coordinate and invariant on the other direction, but an extension to a second coordinate is trivial.

A convolution of a function with a Dirac delta function is equivalent to a translation of the function ($f(x) \otimes \delta_{x_0} = f(x - x_0)$), therefore the convolution in (1.24) becomes a simple sum.

$$A(f_x, z_{after}) = \sum_{m=-\infty}^{\infty} a_m A(f_x - n f_0, z_{before}). \tag{1.26}$$

In practical terms, this result suggests that when a wave interacts with a periodic object, it scatters in multiple directions corresponding to the harmonics of the object. In each of these directions, the angular spectrum, and therefore the shape, of the wave is perfectly replicated.

This concept can be better understood by considering incidence with a plane wave. From the very definition of angular spectrum, the angular spectrum of a plane wave is a Dirac delta function, which angular frequency is determined by the angle of propagation of the wave. The angular spectrum after the interaction then becomes a train of Dirac delta functions, and the field as the sum of plane waves propagating in We can write the field after the grating as

$$U(x, z_{after}) = \sum_{m=m_{min}}^{m_{max}} a_m e^{i2\pi[(f_x - nf_0)x + f_y y]}. \tag{1.27}$$

The extrema of the summation are determined considering again that those directions which transverse wavevector exceeds the modulus of the total wavevector ($\alpha^2 + \beta^2 > 1$) cannot propagate in free space, and can be found by imposing $(2\pi f_x - 2\pi m f_0)^2 + (2\pi f_y)^2 \leq k$.

Analysing the way the periodic structure affected a plane wave, one may associate to it a wavevector K_g and describe the diffraction directions using the following relation:

$$k_d^{(m)} = k_x - K_g^{(m)}, \qquad K_g^{(m)} = m\frac{2\pi}{\Lambda_t}, \tag{1.28}$$

where k_d refers to the transverse component of the wavevector for the various diffraction orders. This relation is very important for diffraction gratings and it is commonly referred to as Bragg's law.

1.3 Angular momentum properties of light

Angular momentum is a conserved quantity in many physical systems, including electromagnetic fields. Electromagnetic waves carry both energy and momentum during propagation, and this latter can by either linear momentum, in the direction of propagation, or angular momentum, in the form of a rotation of the wavefront about its propagation axis. One of the most intriguing aspects of the angular momentum of light is that it can be carried both by the polarization of the field and by its phase spatial distribution. These two types of momenta take commonly the name of spin and orbital angular momentum, respectively.

The spin of a wave is associated to a rotation of its field polarization. Such rotation can arise from e phase delay between two orthogonal components of the propagating vector field. In particular, if these two components have the same modulus, and are phase shifted by a factor of $\pm\pi/2$, than the polarization is said to be circular. Obviously, the rotation can be either clockwise or anticlockwise, in

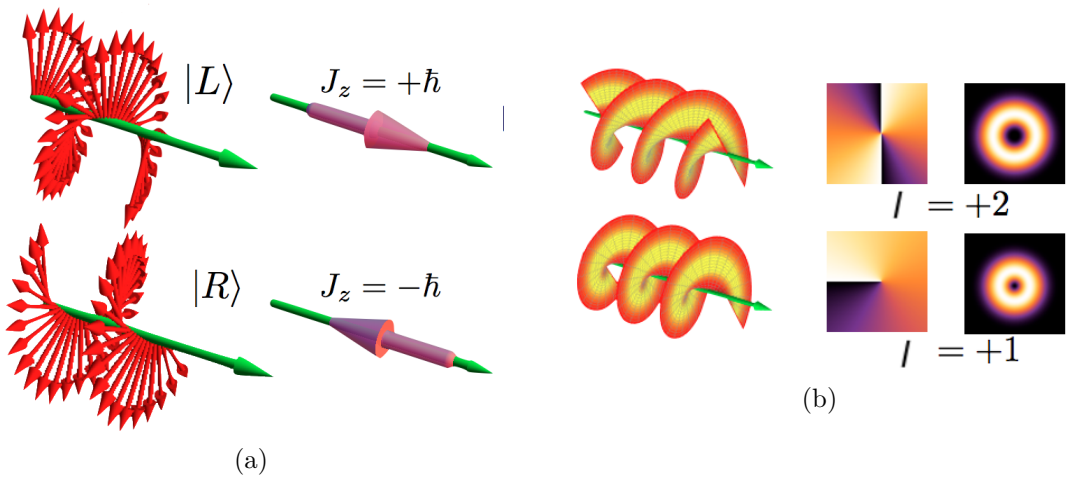

(a) (b)

Figure 1.2: (a) Graphic representation of the spin angular momentum (SAM) related to a rotation of the polarization vector. (b) Graphic representation of the orbital angular momentum (OAM) related to the phase helical shape. Images taken from [23, 24]

which case we speak of left handed circular (LHC) polarization and right handed circular (RCH) polarization, depending on the frame of reference. When the phase difference is not exactly $\pm\pi/2$, or the two orthogonal components do not have same intensity, the polarization is said to be elliptical.

From a quantum mechanical perspective, the angular momentum is an intrinsic property of particles, and it is described by the concept of spin. Photons, which are the quanta of electromagnetic radiation, are spin-1 particles, which means they have an intrinsic angular momentum of $\sigma\hbar$, where $\hbar$ is the reduced Planck constant and σ is the spin number which can assume values of ± 1. The spin of a photon is always aligned with its direction of motion, and it was proven that it can be associated with the circular polarization of the electromagnetic field which is part of. I.e. a circularly polarized field will carry photons with angular momentum

$$\vec{J}_\sigma = (\sigma\hbar)\vec{u}_k,$$

while a linearly polarized field will carry photons which momentum state is a superposition of LHC and RHC polarizations.

Another way that an electromagnetic wave can carry angular momentum is by means of its phase spatial distribution. In particular, when the phase of the wavefront winds around a point in space it creates a helical wavefront shape, with a resulting intensity distribution of the beam having a dark region in the center, surrounded by a bright ring. This helicoidal structure is known as a vortex. The angular momentum then carried by the wave is related to the topological charge of such vortex (the latter being a measure of the winding of the wavefront phase around the vortex core) and it is usually referred to as orbital angular momentum (OAM).

From a quantum mechanics perspective it has been shown that the wavefunction

for an electromagnetic wave can be written as a superposition of different waves with different azimuthal phases, where each wavefront has an associated OAM. For a single photon, the angular momentum associated to different OAM is quantized and can be expressed in the form:

$$\vec{J}_{oam} = (l\hbar)\vec{u}_k,$$

where l is the OAM number and it can assume any integer value, positive or negative. The OAM number l is equal to the topological charge of the optical vortex it is been carried by, and it is equal to the number of arms of the helix forming the vortex.

To summarize, the total angular momentum $\vec{J}$ of a photon carried by a generic field can be expressed in the form

$$\vec{J} = (\sigma + l)\hbar\ \vec{u}_k \tag{1.29}$$

1.4 EM confinement in dielectric structures

Up to this point we haven't really discussed the behaviour of light when interacting with dielectric materials. As mentioned in the first section, when a wave propagates inside a material its speed is reduced. Considering the example of a plane wave propagating into an isotropic homogeneous material, we can relate the speed inside the material to the material refractive index: $v = c/n$. In terms of wavelength instead we can use the relation of Eq. (1.12) in order to deduce that also the wave spatial periodicity is reduced, while the wavevector is increased:

$$\lambda = \lambda_0/n, \qquad k = k_0 n, \tag{1.30}$$

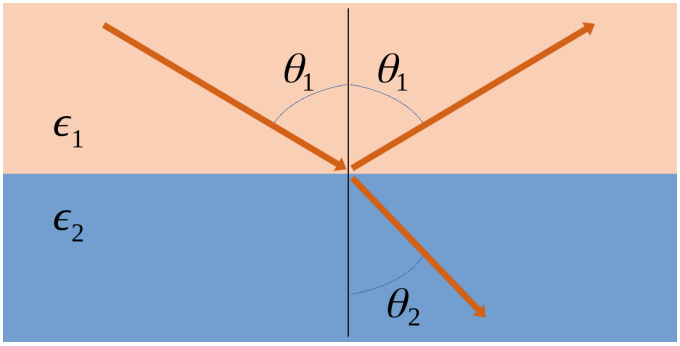

Figure 1.3: Schematic representation of a plane wave impinging at an interface between two materials with different dielectric constant, with angle of incidence θ_1.

with λ_0 and k_0 being the corresponding wavelength and wavevector in vacuum, respectively.

When a wave encounters an interface with a secondary material, the behavior of the field can be predicted by considering the boundary conditions. Specifically, the phase of the wave along the interface should be continuous, together with the tangential components of the electric ($E_{//}$) and magnetic ($H_{//}$) fields, as well as the normal component of the displacement field ($D_{\perp}$). This implies that the component of the wavevector parallel to the interface, $k_{//}$, should be the same on both sides of the interface.

$$\begin{aligned} k_{1//} &= k_{2//} & \qquad E_{1//} &= E_{2//} \\ \epsilon_1 E_{1\perp} &= \epsilon_2 E_{2\perp} & \qquad H_{1//} &= H_{2//} \end{aligned} \tag{1.31}$$

From the first relation one can immediately write down the Snell's law for refraction, which links the angle of incidence of a plane wave, to the angle of refraction after the interface:

$$n_1 sin(\theta_1) = n_2 sin(\theta_2), \tag{1.32}$$

where the angles θ_i are measured with respect to the interface normal. The most interesting aspect that arises from Snell's law is that, if $n_1 > n_2$ and the angle of

incidence is large enough, then the angle of refraction becomes an imaginary value and propagation through the interface is interdicted. If one relates again this angle to the wavevector, they would find that its orthogonal component $k_\perp$ (after the interface) becomes an imaginary number, which corresponds to a non-propagating, exponentially decaying field, signature of evanescent waves. The maximum angle of incidence that allows for propagation in the second material is called critical angle θ_c and when $\theta_1 > \theta_c$ we speak of total internal reflection.

The very existence of the total internal reflection is at the base of many dielectric devices. In facts, it allows to confine light within a region of space, and by carefully engineering the structure of these materials, it is possible to create optical cavities and waveguides that can trap and manipulate light in a pletora of ways.

Fresnel's coefficients

From the other relations in (1.31), one finds out that part of the energy of the wave is refracted, and part is reflected. To write down the coefficients for transmission and reflection it is necessary to decompose the incident wave into a component with the electric field parallel to the interface, transverse electric (TE) polarization, and a component with the magnetic field parallel to the interface, transverse magnetic (TM) polarization.

$$\begin{aligned} r_{te} &= \tfrac{n_1 cos\theta_1 - n_2 cos\theta_2}{n_1 cos\theta_1 + n_2 cos\theta_2}; & t_{te} &= 1 - r_{te}; \\ r_{tm} &= \tfrac{n_2 cos\theta_1 - n_1 cos\theta_2}{n_2 cos\theta_1 + n_1 cos\theta_2}; & t_{tm} &= 1 - r_{tm}. \end{aligned} \tag{1.33}$$

These are commonly referred to as Fresnel coefficients. The amplitudes of the reflected and refracted waves can be computed multiplying the amplitude of the impinging wave times the respective Fresnel coefficient (e.g. $E_{2//} = t_{te} \cdot E_{1//}$).

Very interesting from the Fresnel coefficients is to note that there is an angle,

called Brewster angle, for which the r_{tm} coefficient goes to zero, while the r_{te} doesn't.

$$\theta_b = arctan\left(\frac{n_2}{n_1}\right). \tag{1.34}$$

This difference in behaviour between the TE and TM polarizations can have very important consequences in optical devices such as lenses, coatings and, more interestingly, photonic crystals.

1.4.1 Guided modes

By exploiting the effect of total internal reflection, it is possible to confine light into narrow regions of space in such a way to control its propagation. The most famous example of this are optical fibers, where light is confined into a high refractive index wire surrounded by a low refractive index material. Since light is confined by means of multiple reflections, a phenomenon very similar to a resonances arises inside a waveguide and the constructive (or destructive) interference of the reflected waves allows only light with certain energy and momentum to propagate in the system.

To understand propagation inside a linear waveguide one can make the assumption of variables independence:

$$U(x, y, z) = f(x, z)g(y),$$

where y is aligned with the waveguide axis. With this conditions one can rewrite the Helmholtz equation (1.13), making a distinction between the TE and the TM case (depending on the symmetry of the system), and obtain a new equation on $g(y)$. Imposing some boundary conditions, and assuming a dependence on the y coordinate of the type $e^{ik_y y}$, one can solve this new equation and find a set of solutions that will represent the modes propagating inside the waveguide. More

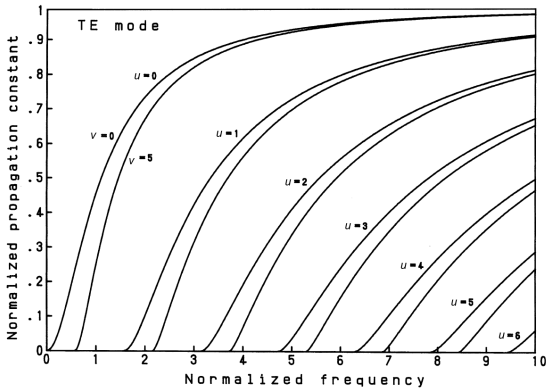

Figure 1.4: Dispersion of the modes inside a slab waveguide. Image taken from [25].

than the shape of the field, it is often interesting to find a relationship between the wavevector and the angular frequency of the wave by substituting the solution into the originating wave equation. This relation will be of the type

$$k_y = f(u, \nu, \omega),$$

where u, ν are integers called modal numbers that determine to which mode the dispersion refers to. An example of dispersion relation can be seen in Figure 1.4.

Most of the times it is not possible to find an analytical solution for the dispersion relations, therefore one must often rely on numerical methods. In comparison to the dispersion of a photon propagating in free space (1.12), where the linear dispersion allows us to relate the wavevector inside a material to the refractive index $k = nk_0$, the dispersion inside a waveguide is strongly non-linear. Nonetheless one may try to define an effective refractive index n_{eff}, such that the relation is written in the same form:

$$k_y = n_{eff}(\omega)k_0. \tag{1.35}$$

This relation allows to approximate propagation inside the waveguide like a planewave propagating inside an effective material with refractive index n_{eff}. The idea of using

an effective index to describe a guided mode comes very useful to model nanophotonic devices, because it allows to treat a problems that is originally tri-dimensional, into a much simpler model with reduced dimensionality.

1.4.2 Photonic crystals

Another extremely powerful method for confining waves is represented by crystals, which offer an efficient method for control by providing a periodic structure of the properties regulating their propagation. This concept can be applied to any wave propagation phenomena, from the electron propagation inside semiconducting crystals, to sound propagation in phononic crystal and, obviously, also to electromagnetic waves in photonic crystals (PC). The concept of photonic crystals was first proposed in 1987 by Eli Yablonovitch [26] and Sajeev John [27], who independently introduced the idea of using periodic dielectric structures to create a photonic band gap. Since the work proposed by Yablonovitch, research in photonics has made huge progresses with photonic crystal, especially since the technologies for fabrications have given an easy access to the creation of nanophotonic structures.

The simplest PC that one can create consists of a layered stack of two alternating dielectric materials, also referred to as one dimensional photonic crystal (1DPC). To study this medium one can use the same approaches proposed for semiconductors and write the solutions of Maxwell's equation using a (periodic) Bloch function

$$U_{n,k_z,k_{//}}(\vec{r}) = e^{i\vec{k}_{//}\cdot(x,y)} e^{ik_z z} u_{n,k_z,k_{//}}(z),$$

where $u_{n,k_z,k_{//}}(z+\Lambda) = u_{n,k_z,k_{//}}(z)$, with Λ being the period of the crystal. The Bloch decomposition defines an eigenvalue problem, which solutions provide the dispersion of the modes allowed to propagate in the structure. The first Brillouin zone for this crystal is limited in the range $-\pi/\Lambda < k_z < \pi/\Lambda$ and propagation

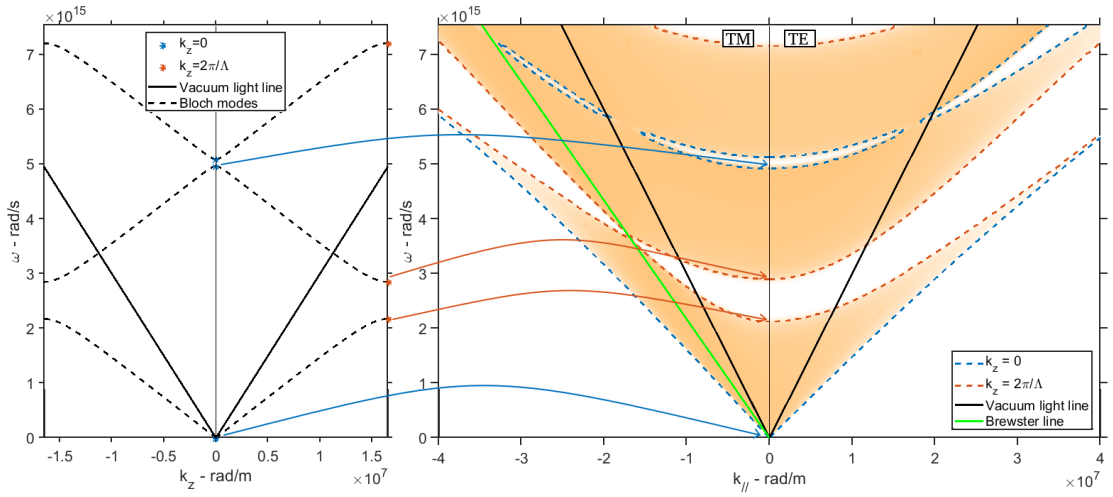

Figure 1.5: On the left, First Brillouin zone for a 1DPC, $k_{//} = 0$. One the right, corresponding band diagram where the band edges are highlighted. The part of the band diagram with negative $k_{//}$ corresponds to the TM modes, while the positive side correspond to TE modes. The 1DPC is composed of two layers, one made of Titania ($n_{Ti_2O_2} = 2.53$) of thickness $d_{Ti_2O_2} = 70$nm, and the other one made of Allumina ($n_{Al_2O_3} = 1.65$) of thickness $d_{Al_2O_3} = 120$nm. The codes for computing the first Brillouin have been provided by [28].

inside the structure is restricted only to certain energy ranges. This concept can be better understood by looking at Figure 1.5 (on the left), where an exemplary dispersion of the allowed modes for $k_{//} = 0$ is compared to the dispersion of a photon propagating in free space.

For $k_{//} > 0$ the band diagram changes shape, and therefore it is often useful to analyse the photonic response by looking at the dependence on the transverse wavevector $k_{//}$ for multiple values of k_z. More specifically, one can consider the extrema of the first Brillouin zone $(0, \pi/\Lambda)$ and plot the dispersion of the allowed modes. For any other value of $k_{//}$, the dispersion of the modes will lay in between the two extrema, thus these latter define a series of regions, or bands, where propagation is allowed and of which they represent the band edges. This concept can be summarized with the band diagram, where the allowed modes inside the photonic crystals are evidenced as a function of the $k_{//}$ and ω, like in Figure 1.5.

It is interesting to notice the difference in shape of the band diagram, between the TE and TM polarizations. In particular, while for TE polarization the bandgap edges tend to diverge, for the TM polarization the band gap edges converge to a point, to diverge again at greater $k_{//}$. The points are called Brewster points because they originate from the different behaviour of the reflection and transmission Fresnel coefficients (1.33) for the two different polarizations. The Brewster points are aligned along a line that, for a bi-layer 1DPC, is identified by the following relation [28]:

$$\omega_b = c_0 \cdot k_{//} n_1 sin(\theta_b) \qquad \longrightarrow \qquad \omega_b = c_0 \cdot k_{//} \frac{n_1 n_2}{\sqrt{n_1^2 + n_2^2}}. \tag{1.36}$$

Distributed Bragg reflectors

In real life an infinitely periodic structure does not exist, therefore one is always forced to create PC with a finite number of periods. The real-life 1DPC would therefore become a dielectric multilayer stack. It is safe to assume that the photonic response of a dielectric multilayer would approach the one of a 1DPC, the more layers are introduced. Therefore, the band diagram of a the finite structure can be expected to be similar to the one of the corresponding ideal PC.

Thanks to the existence of the energy band gaps, these periodic dielectric multilayers can be exploited as mirrors and reflectors that operate within specific frequency ranges. For these applications, they are commonly known as distributed Bragg reflectors (DBRs) or dichroic mirrors. The reflectivity map of a DBR can be associated with its band diagram map. The reflectivity map measures the proportion of light reflected by the multilayer when it is illuminated with specific energy and momentum. In facts, modes that lay within the light cone (air or vacuum) have access to free space propagation from the two interfaces with the external medium. This means that a plane wave impinging on the multilayer with specific ω and $\vec{k}$ values will propagate inside the multilayer through the mode at those coordinates

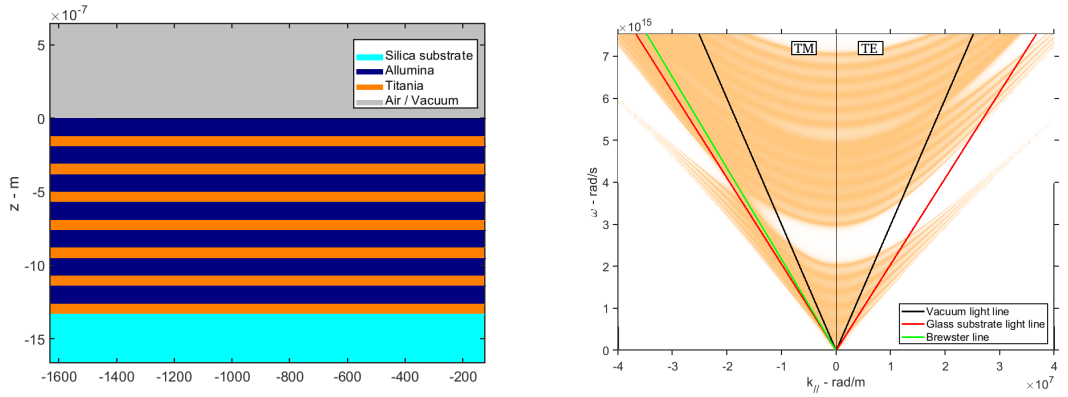

(a) (b)

Figure 1.6: (a) Example of a dielectric multilayer working as distributed Bragg reflector. The multilayer consist of 7 pairs of Titania and Allumina, which thicknesses are the same as for the 1DPC in Figure 1.5. The multilayer is placed on top of Silica glass substrate. (b) Band diagram of the DBR, where the vacuum and substrate light line are included.

and emerge on the other side, provided that the external medium allows it. For this reason, within the light cone, there is a one-to-one correspondence between the reflectance map and the band diagram.

The reflectance map of the DBR can be easily computed by means of the transfer matrix method TMM. This is a numerical technique that uses a decomposition into plane waves (very similarly as in Fourier optics) in order to find the transmission and reflection coefficients through the structure. See Section 1.5.1 for more information on the TMM.

Particularly interesting is the application of DBRs to guided modes. As it was mentioned in Section 1.4.1, it is possible to associate an effective index to a guided mode. Since this effective index depends on the thickness of the waveguide, one could inscribe a corrugation over its surface and define a region where the system can be represented by an alternating sequence of effective indices. If this sequence is periodic, one could use the methods developed for dielectric multilayers, such

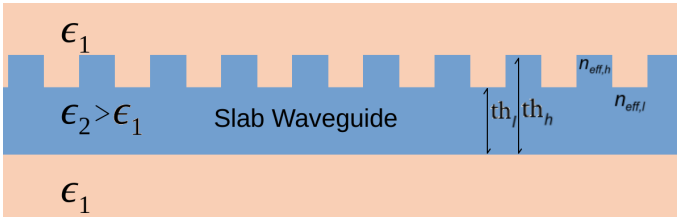

Figure 1.7: DBR on a waveguide.

as the TMM, in order to design a DBR using the full dispersion of these effective indices. This allows to create mirrors inside nanophotonic structures, without the need for metallic components.

By placing two DBRs in front of each other, one can create a resonant structure, which resonance would depend on the distance between the two mirrors. This type of cavity is generally referred to as Fabry-Pérot cavity and it represents the easiest way to create a resonant device inside a nanophotonic structure. This type of cavities can also be considered as created by introducing a defect into a 1DPC, therefore their resonances can be studied also using the tools developed for studying defects inside crystals.

Another interesting parallelism can be done between DBR structures in the effective index approximation and diffractive gratings. In facts, a corrugation on the surface of a waveguide can be accounted to a diffractive periodic grating. Treating this structure following Bragg's law one can find the corresponding diffraction orders $k_d^{(m)}$ and predict the direction of scattering by assigning a wavevector K_g to the grating. In order to obtain reflection on the waveguide, the grating needs to have a scattering order (m) which wavevector is equal to the guided mode wavevector (k_{wg}), but with opposite sign (propagating backwards). From Bragg's law (1.28), $k_d = k_{wg} - K_g^{(m)}$, therefore:

$$k_d = k_{wg} \qquad \Rightarrow \qquad K_g^{(m)} = 2n_{eff}(\omega)k_0. \tag{1.37}$$

In this way the grating would be acting as a mirror on the waveguide and, and the corresponding DBR dispersion diagram would find a band gap centred around the wavelength for which the diffraction order was designed. It should be noted that the effective index on the region of the grating is not uniquely defined, but, in a first approximation, it is possible to consider a weighted average of the effective refractive index over one period of the grating. For instance, for a rectangular grating over a slab waveguide one could write

$$n_{eff}(\omega) = n_{eff,h}(\omega) \cdot FF + n_{eff,l}(\omega) \cdot (1 - FF), \tag{1.38}$$

where $n_{eff,h}$ and $n_{eff,l}$ are the effective indices in the thickest and in the thinnest parts of the waveguide, respectively. FF is the fill factor and corresponds to the ratio between the length of the rectangle over the period of the grating.

With very similar reasoning one may design a diffractive grating that scatters light from the guided mode into free space, at the angles provided by the diffraction orders. And the same grating could be used to couple light propagating from free space at such angle, directly into the waveguide.

1.4.3 Bloch Surface Waves

When an infinitely extended material is truncated, a surface interacting with an external medium arises. When a infinitely periodic crystal is truncated in half, surface states can arise at the interface with the external medium in the form of defects in the band gaps of the crystal. In the case of a 1DPC, these defect states are called Bloch surface waves (BSWs) and they are characterized by having the field intensity confined in a narrow region around the surface and by having a dispersion relation confined beyond the light cone and inside one of the band gaps.

In recent decades, there has been an increased interest towards Bloch surface waves. Unlike conventional guided modes, BSWs have a long exponential decay

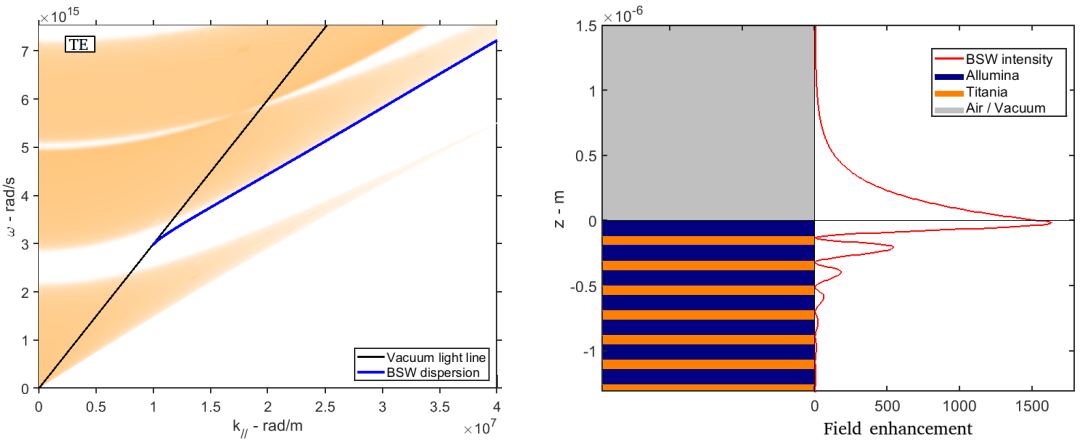

(a) (b)

Figure 1.8: (a) Dispersion of a BSW inside the band diagram. (b) Field intensity distribution at a given frequency. The semi-infinite 1DPC is the same as of Figure 1.5, where the periodicity has been interrupted at a Silica layer. The corresponding BSW is TE polarized

tail that extends into the external medium, rendering them highly sensitive to the optical properties of surfaces. This property makes them a suitable candidate not only for sensing applications, but also for a variety of nanophotonic devices where light manipulation is performed at the surface level. For these reasons, the devices proposed in this thesis have been designed and studied based on BSWs due to their unique optical properties.

When considering a periodic dielectric multilayer versus the semi-infine structure presented above, the surface state mainains its position in the band gap, but the quality of the BSW dispersion could be reduced. In particular, when placing the multilayer on top of a dielectric substrate, such as glass, the exponential tail of the BSW extending beyond the multilayer and into the substrate may offer a channel for a leakage of radiation from the BSW to the substrate. This could happen because the BSW dispersion, even though it lays beyond the vacuum light cone, it may not lay beyond the light cone of the substrate. The light line of the substrate

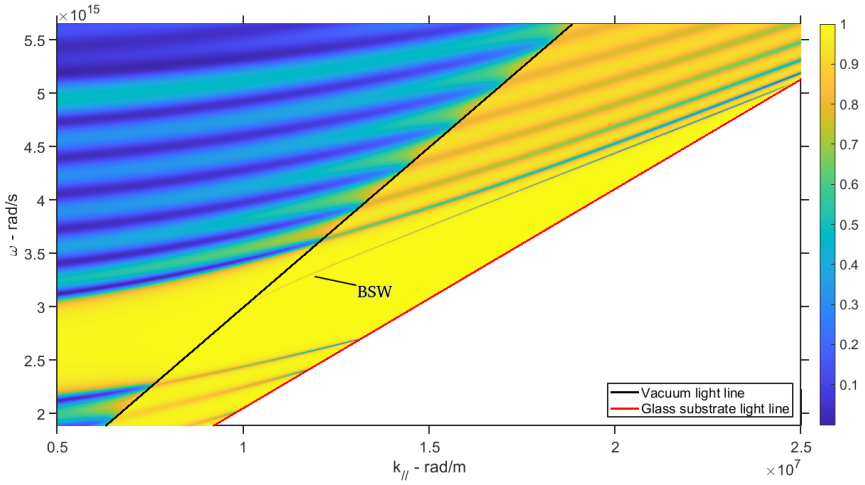

Figure 1.9: Reflectivity map for a the dielectric multilayer of Fig. 1.6. The BSW dispersion appears as a dip in reflectivity.

is simply described by the relation $k_{//} = n_s k_0$, with n_s being the substrate refractive index. Although the leakage channel reduces the quality of the BSW, it also provides an easy method for accessing (i.e. injecting energy into) the mode.

Since the BSW dispersion is located beyond the vacuum light line, it is not possible to utilise the reflectivity map to sample a surrounding region on the band diagram. When impinging from the air side of the multilayer, the maximum transverse momentum that can be used to probe the multilayer is limited by the vacuum light line itself. When impinging from the substrate side instead, it is possible to match both energy and momentum of the BSW, but transmission would be still prevented since on the other side the wave would not be able to propagate in air, resulting in total internal reflection for any point in the reflectivity map beyond the air light line.

Although the one-to-one correspondence between the reflectance map and the band diagram is lost, it is still possible to extract information about the band diagram beyond the light line. When analyzing a real material, it is necessary to take into account for losses caused by absorption or material imperfections, even when they are very small. In the presence of losses, a portion of the energy is dissipated

within the multilayer, and the sum of the reflected and transmitted wave intensities no longer equals the impinging wave intensity. Thus, even in cases of total internal reflection, where the transmitted wave intensity is null, it is still possible to measure the effect of absorption on the reflected wave. When light with a momentum and energy that matches that of a mode propagating within the multilayer, such as a BSW, impinges on the multilayer beyond the light line (i.e., from the substrate), a significant amount of energy is lost due to absorption by the various materials encountered during mode propagation. Consequently, modes lying beyond the light line appear as dips in the reflected intensity within the reflectivity map, as for the BSW in Figure 1.9.

BSWs are often compared to surface plasmon polaritons (SPPs), since these latter offer another method to bind electromagnetic propagation on the surface. SPPs exploit the surface resonances arising at the interface between a metal and a dielectric and, for this very reason, they represent an extremely lossy method for propagation. BSWs instead offer much greater propagation lengths, since most of the losses are represented by the leakage radiation, and this latter can be ideally reduced to zero by increasing the number of periods in the multilayer, thus isolating the surface from the substrate, or by utilising the BSW only with momentum beyond the substrate light line.

It should be noted that contrary to surface states in semiconductors, to the author's knowledge there is not an analytical solution for the BSWs dispersion, therefore their analysis and design relies on numerical methods, such as the TMM discussed in the following sections.

1.5 Computational methods

To simulate and numerically study photonic and optical devices there are multiple methods, some of which involve the solution of the wave propagation differential equation, either by means of finite difference time domain (FDTD) simulations or finite elements methods (FEM), while others involve some assumptions on the mathematical form of the solution, like for the plane wave expansion method (PWEM) the transfer matrix method (TMM) or the beam propagation method (BPM). These are only some of the numerical methods amongst the many that are available. For this thesis, in order to simulate the devices that where under study, numerical simulation where focused around TMM and the FDTD simulations.

The first one was self-implemented and it was used to analyse the dispersion relation of the dielectric multilayer stacks. It allows to evaluate the quality of the surface mode resonance, compute its effective refractive index, together with the field distribution inside the multilayer. The TMM was implemented both for MATLAB[29] and Python computing languages, and it is available on Github in [30, 31].

The second method, FDTD simulations, was used in order to perform full-device simulations by solving Maxwell's equations using a direct Euler's approach. There are multiple FDTD solvers available, for this thesis two softwares were used, one is a proprietary software called Lumerical [32], from the homonym company, and the other is an open source library called Meep [33], initially developed at MIT, that can be used both in C++ and in Python. For this second method the source codes for generating the simulations are available in [34, 35] for Lumerical, and in [36] for Meep.

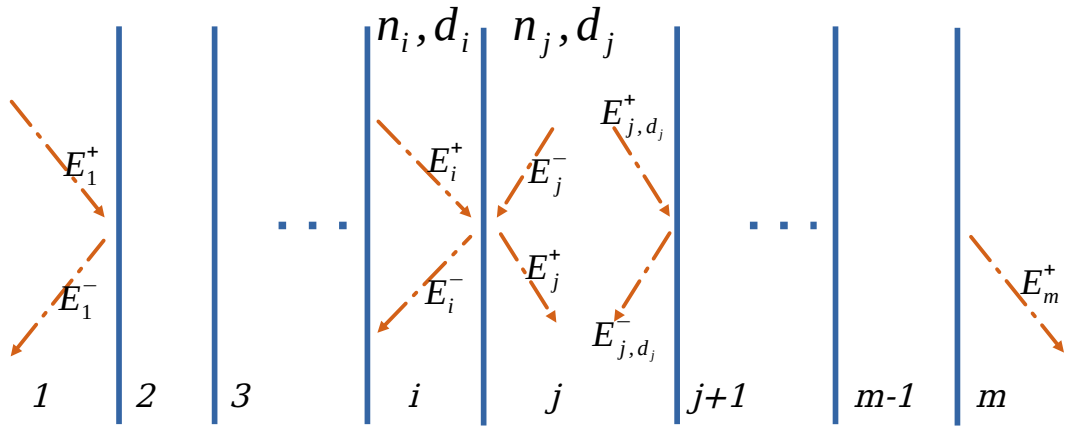

Figure 1.10: Schematic representation of propagation in a dielectric multilayer

1.5.1 Transfer Matrix Method

From all the theoretical background presented so far, it is very clear that plane waves represent an ideal basis for analysing the behaviour of light propagating inside a dielectric structure. The transfer matrix method (TMM) is a technique that uses this fact in order to study the behaviour of layered structures. The computation analyses the response of the multilayer structure by assuming a plane wave impinging on the stack from the first layer, with a given energy (ω) and at given angle (θ_{in}). Then, by means of a matrix product, reflection and transmission through the whole stack is computed. By repeating this operation for different values of energies and angles of incidence, one can retrieve the whole reflectance map of the multilayer.

The TMM is based on the fact that refraction from a planar interface can be described by a matrix product between the field on one side of the interface and a matrix which elements are determined by the Fresnel coefficients (1.33). In particular, one can decompose the total field of a wave propagating inside the structure into a component propagating forward (E^+) and a component propagating backward

(E^-). The technique works by assigning a transfer matrix $T_{i,j}$ to each interface between layer i and layer j of the stack, in such a way to write

$$\begin{pmatrix} E_j^+ \\ E_j^- \end{pmatrix} = T_{i,j} \begin{pmatrix} E_i^+ \\ E_i^- \end{pmatrix}. \tag{1.39}$$

Then, by using a matrix P_j to describe propagation, it is possible to relate the field on layer i to the field before the next interface with layer $j+1$: $E'_j = P_j T_{i,j} E_i$. By applying this reasoning recursively, and performing all the matricial products, it is possible to express the field on the right most side of the multilayer to the field on the left most side

$$E_m = M\ E_0 = T_{m-1,m} \left(\prod_{i=0}^{m-1} P_{i+1} T_{i,i+1} \right) E_0 \tag{1.40}$$

where m is the number of layers. By assuming the input to be only on the left side ($E_0^+ = 1$ and $E_m^- = 0$), one can compute the reflected field E_0^- and the transmitted field E_m^+, by using the elements of the matrix M

$$E_0^+ M_{21} + E_0^- M_{22} = E_m^- = 0 \quad \longrightarrow \quad E_0^- = -E_0^+ M_{21}/M_{22}, \tag{1.41}$$

$$E_0^+ M_{11} + E_0^- M_{12} = E_m^+ \quad \longrightarrow \quad E_m^+ = -E_0^+ \left(M_{11} - M_{12} M_{21}/M_{22}\right) \tag{1.42}$$

The reflectivity is the ratio between the modulus of the reflected wave with the modulus of the impinging wave: $R = |E_0^-|^2$. And the same goes for the transmission $T = |E_m^+|^2$. If losses are neglected, i.e if the dielectric constants for all the layers are real valued, then $R + T = 1$.

Reflectivity maps computed with this technique will be dependent on the two parameters (θ_{in},ω). In order to convert these maps into band diagrams with parameters ($k_{//}$,ω), it is sufficient to remember that the transverse wavevector can

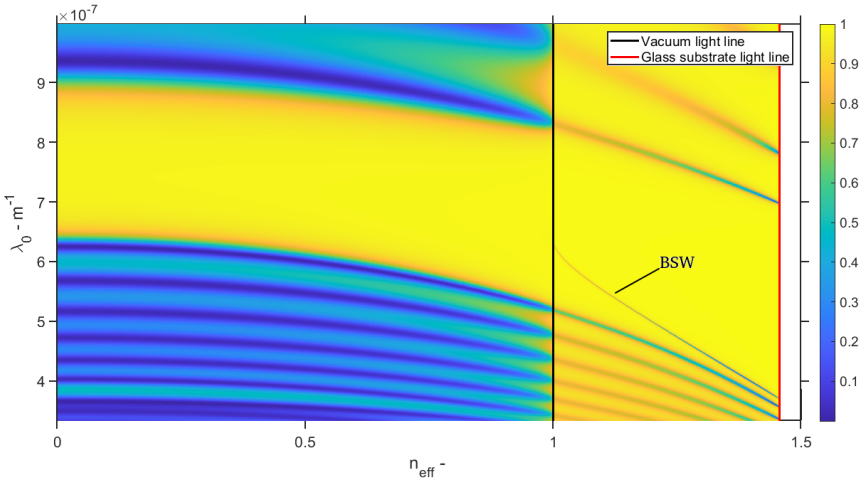

Figure 1.11: Reflectivity map for a the dielectric multilayer of Fig. 1.6 represented as a function of the effective index n_{eff} and the vacuum wavelength λ_0.

be expressed as $k_{//} = k \cdot sin(\theta_{in})$, and that for a plane wave the modulus of the wave vector is $k = n\omega/c$. $K_{//} = n_1\omega/c \cdot sin(\theta_{in})$, with n_1 being the refractive index of the first layer of the stack. Due to its relevance in spectroscopic applications, sometimes it is useful the represent the energy axis as a function of the vacuum wavelength λ_0, with $\lambda_0 = 2\pi/k_0 = 2\pi c/\omega$. When this method is applied to analyse Bloch surface waves, it is used to compute the surface mode dispersion and determine its effective index. For this reason it is often useful to plot the reflectivity map directly as a function of the effective index in lieu of the transverse wavevector $n_{eff} = k_{//}/k_0 = n_1 sin(\theta_{in})$, as in Figure 1.11.

Implementation of the TMM

In order derive the transfer matrix $T_{i,j}$, it necessary to look in detail the relations that link the forward and backward propagating waves through the Fresnel coefficients. At the interface between layer i and layer j one would write:

$$E_j^+ = E_i^+ t_{ij} + E_j^- r_{ji}$$
$$E_i^- = E_i^+ r_{ij} + E_j^- t_{ji}$$

where r, t are the Fresnel coefficients, referring either to TE or the TM polarization, and the subscripts ij, ji refer to the coefficients being computed either from i to j, or vice versa respectively. Rewriting the second equation to isolate E_j^-, and substituting in the first, one obtains

$$\begin{array}{l} E_j^- = \left(E_i^- - E_i^+ r_{ij}\right)/t_{ji} \\ E_j^+ = E_i^+ t_{ij} + \left(E_i^- - E_i^+ r_{ij}\right) r_{ji}/t_{ji} \end{array} \quad \Longrightarrow \quad \begin{array}{rcccccc} E_j^+ = & E_i^+ & \left(\frac{t_{ij}t_{ji} - r_{ij}r_{ji}}{t_{ji}}\right) & + & E_i^- & \frac{r_{ji}}{t_{ji}} \\ E_j^- = & E_i^+ & \left(-\frac{r_{ij}}{t_{ji}}\right) & + & E_i^- & \frac{1}{t_{ji}} \end{array}$$

By remembering the definitions of the Fresnel coefficients, it is immediate that $r_{ji} = -r_{ij}$ and that $t_{ij}t_{ji} - r_{ij}r_{ji} = 1$. The transfer matrix T_{ij} then takes the form:

$$\begin{pmatrix} E_j^+ \\ E_j^- \end{pmatrix} = T_{ij} \begin{pmatrix} E_i^+ \\ E_i^- \end{pmatrix} \quad \longrightarrow \quad T_{ij} = \frac{1}{t_{ji}} \begin{pmatrix} 1 & r_{ij} \\ r_{ji} & 1 \end{pmatrix} \tag{1.43}$$

Before connecting this result the following layer $(j+1)$, it is necessary to take into account for propagation into layer j. Since we are dealing with plane waves, propagation can be described as a simple phase shift along the $z-$direction,

$$E_{j,z}^+ = E_j^+ e^{ik_z^{(j)} z},$$

where the value of $k_z = \frac{2\pi}{\lambda_0} n_j cos(\theta_j)$ has to be determined using Snell's law.

$$cos(\theta_j) = \sqrt{1 - sin(\theta_j)^2} = \sqrt{1 - \left(\frac{n_i}{n_j} sin(\theta_i)\right)^2}.$$

Since all the interfaces are parallel to each other, the conservation of the transverse wavevector implies that the product $n_i sin(\theta_i) = \beta_k$ is constant for any value of i. β_k represents the transverse wavevector normalized with respect to the wavevector modulus.

$$n_j cos(\theta_j) = \sqrt{n_j^2 - \beta_k^2}. \tag{1.44}$$

Considering that the backward propagation can be described with a simple sign inversion, and that the following interface will be located at a distance d_j (thickness of layer j), we can write the propagation matrix in layer j as:

$$\begin{pmatrix} E^+_{j,d_z} \\ E^-_{j,d_z} \end{pmatrix} = P_j \begin{pmatrix} E^+_j \\ E^-_j \end{pmatrix} = \begin{pmatrix} e^{+id_z\sqrt{n_j^2-\beta_k^2}} & 0 \\ 0 & e^{-id_z\sqrt{n_j^2-\beta_k^2}}, \end{pmatrix} \tag{1.45}$$

with the transverse wavevector computed on the first layer $\beta_k = n_1 sin(\theta_{in})$.

1.5.2 FDTD Simulations

The finite difference time domain method discretizes the electromagnetic field equations in both space and time domains and updates the fields at each time step based on the values at the previous time step. The technique is based on finite difference approximations to the derivatives in the field equations, and it is very flexible and can handle complex geometries and material structures. As the discretization steps are made finer and finer, the computed solution becomes a closer and closer approximation for the true continuous equations. Time-domain methods possess the advantage of being capable of obtaining the complete frequency spectrum of responses or eigenfrequencies during a single simulation by means of Fourier-transforming the response to a short pulse or utilizing more advanced signal-processing approaches.

The FDTD simulations performed and presented in this thesis comprise of three main components:

- a dielectric structure defined in one, two or three dimensions,
- a source of electromagnetic waves,
- and some monitors to measure the field intensity in certain regions and possibly compute the Fourier transformed fields.

In electromagnetic simulations, wave sources can be created by simply introducing an oscillating current $\vec{j}(\omega)$ in a region of space. Even though simulating the oscillating electric field of a plane wave, or an electric dipole, with a current source might not seem physically correct, mathematically it is completely equivalent. An electric dipole, for instance, can be numerically described by a point source of current.

Depending on the purpose of a simulation, its numerical solution might involve all the three components of the electric fields and of the magnetic fields. For most problems though, simulating the Electric field component only is sufficient. The monitors in the simulation are therefore used to record the time evolution of such electric field in a specific region of space, and derive the other components of the field by means of Maxwell's equations. If one is interested in simulating the spectral response of the simulated structure, it is possible to set the monitors to compute the time Fourier transform of the evolving field. In such case the monitor accumulates the numerical transform at each time step, rather than saving the whole time evolved field and compute the F.t..

Sometimes nanophotonic devices are designed to generate a particular effect at a distance far from themselves. For instance, one may require to simulate a device that manipulates a propagating beam or maybe that generates a specific type of free space propagating beam. For these devices, it is necessary to determine the behaviour of the field propagating also at a very far distance from itself, but simulating the whole beam propagation with the FDTD would be impractical. If the beam propagation happens inside an homogeneous medium, one can utilise an electric field monitor to determine the time Fourier transform of the field at the device level. Then, this near-field can be numerically propagated at a far distance by simply applying the Rayleigh-Sommerfeld formula (1.22). In this way the far-field can be computed without the need of further simulation time.

Effective index method for 2D FDTD

Simulating tri-dimensional structures can be computationally expensive, therefore it is often useful to rely on approximations in order to perform quick testing of a desired device, especially at the initial stage. In the case of BSWs, this can be performed by exploiting the effective index approximation in order to simulate the nanophotonic structures by removing one dimension from the simulation domain. In facts, surface modes, by definition propagate in a direction parallel to the surface (while decaying exponentially in the normal direction), therefore within an effective index approximation one can neglect the multilayer, and perform only bi-dimensional simulations.

By introducing a proper spatial modulation in the mode effective index, it is then possible to create all sort of optical devices such as waveguides, Distributed Bragg Reflectors (DBR) or even more complex two-dimensional photonic crystals. To introduce a modulation in the effective index, it is sufficient to change the dielectric properties of the surface. In practical terms, increasing or reducing the thickness of the last layer shifts the dispersion of the surface mode inside the band gap, according to a well known phenomenon called dielectric loading. As a result, a multilayer with a corrugation on top can be simulated by associating a different effective index to different heights on the corrugation. E.g. a square grating (rectangular profile) would be represented by only two effective indices.

The main problem when using the effective index approach for FDTD simulations comes from the dispersion of the effective index itself ($n_{eff} = n_{eff}(\omega)$). Simulating dispersive materials in time simulations is not trivial, because the dispersion is defined as a function of the angular frequency ω, and it cannot easily be converted into a time simulation. For most of the real materials, it is possible to describe their dispersion by means of Lorentz and Drude models for the susceptibility of the material. But for an effective material, described by an effective index,

these models may not be sufficient to properly catch the material dispersion. Sometimes it is possible to use a linear combination of Lorentzian susceptibilities, to fit the dispersion model, but other times it is simply not possible to obtain a good fit. Nonetheless nanophotonic devices, like a resonant cavity, are often designed to work in specific frequency ranges. Therefore, if such range is sufficiently narrow, one may simply assume the effective index to be constant $n_{eff} = n_{eff}(\omega_{work})$. It is important to stress that the simulated device behaviour would therefore be correct only close to the working frequency. If the range is not sufficiently narrow, one may try to perform multiple simulations with multiple values of effective index, and combine the various results in post processing.

Chapter 2

Azobenzene polymers for Bloch Surface Waves control

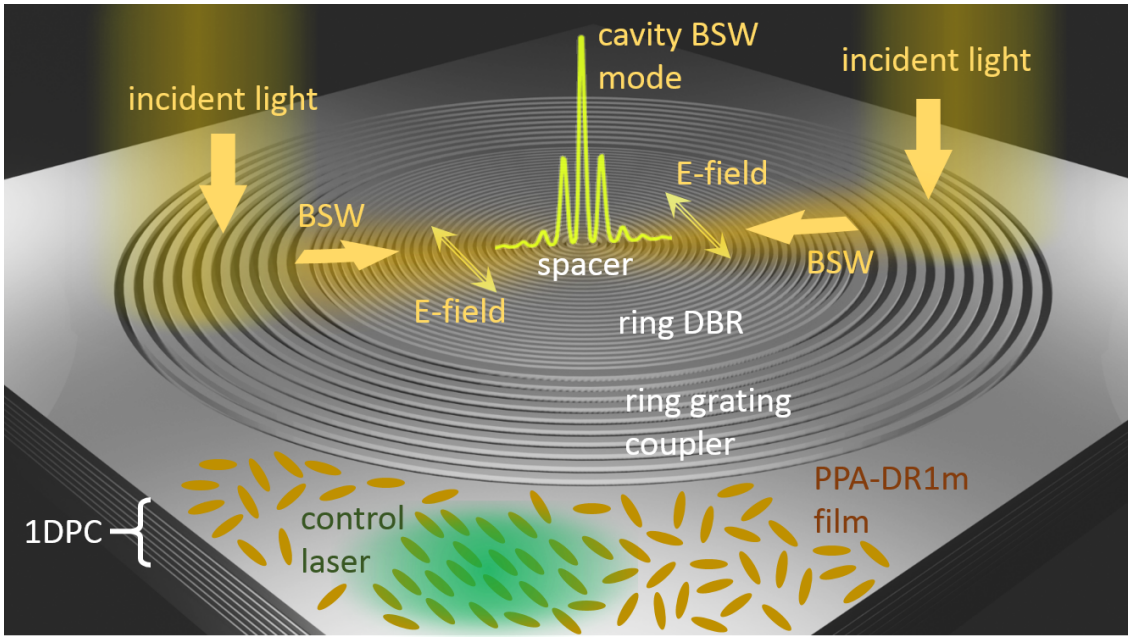

Figure 2.1: Illustrative 3D sketch of the resonant 1DPC patterned with the annular grating coupler and the BSW cavity constituted by a Distributed Bragg Reflector (DBR) surrounding an inner circular spacer.

Tunable photonics deals with micro and nanostructures able to modify some of their optical functions and properties upon external cues, which are typically

fed as control means in active devices or measurand in sensing architectures. In many active devices, changes in the refractive index of constituent materials can be obtained after providing an external luminous trigger [37], often in the form of focused laser beams. Modulation strategies involving all-optical control are particularly advantageous in integrated photonic chips as compared to other approaches (e.g. based on thermo-optical or photo-acoustic effects), since they allow reaching a considerable spatial selectivity and a minimal cross-talk with adjacent circuit parts. With this respect, intensive research efforts are presently directed towards new optical materials, such as transparent conductive oxides [38] and semiconductors [39], with tailored linear and non-linear properties enabling an optical modulation based on sufficiently strong, yet reversible, refractive index changes. Alternatively, polymeric compounds containing light-active units (e.g. azobenzenes [40] and dithienylethene [41]) represent a valuable option in hybrid organic-inorganic architectures, mainly because of the large variety of different light-responsive mechanisms available [42] and the moderate power required to the external radiation to trigger the photoswitching functionalities. As an example of integrated hybrid photonic device, azobenzene-functionalized silica toroidal resonators have been demonstrated to show a stable, reversible spectral tunability up to about 4 nm at telecom wavelengths, upon illumination with external laser sources in the visible [43]. While light-induced conformational changes in azobenzene molecules have been successfully used to produce refractive index variations [44] cyclic photoisomerization and the subsequent re-orientation of dipole momenta in azobenzene-containing polymeric films is well-known to result also into remarkable birefringence, whose spatial orientation is determined by the polarization state of the illuminating radiation. Such an optically-induced anisotropy offers intriguing opportunities to tune topological features in planar photonic structures, as recently demonstrated for metasurfaces in [45, 46].

In this chapter, we present a solid-state dielectric multilayer functionalized with a structured, optically active polymeric film which birefringence can be controlled via a properly polarized external laser radiation. This work is the result of a collaboration with the University of Genova and it has been published in [47].

Here, we demonstrate that the resonances associated to surface modes sustained by the structure can be spectrally modulated over a range of few nanometers in wavelength. The concept is better illustrated in Figure 2.1. A blend of an optically active azopolymer (DR1M) and a thermally-sensitive resist (PPA) is spun on a dielectric multilayer (one-dimensional Photonic Crystal -1DPC) to form a very thin film. The 1DPC sustains TE-polarized Bloch Surface Waves (BSWs) in the visible (details in the Experimental section). A resonant flat-optics nanocavity for BSWs is then fabricated on top of the DR1M-PPA film by means of a novel thermal-Scanning Probe Lithography approach. Thermal-Scanning Probe Lithography (t-SPL) has recently emerged as a very promising approach to locally tailor materials properties at the nanoscale level, thanks to a sharp conductive probe able to induce local and controlled heating of the surface [48]. In this way, high-resolution nanolithography can be performed onto polymeric layers possibly transferred onto other substrates, so that photonic architectures can be engineered to implement various optical functions [49]. An external laser beam with a controlled polarization state produces an optical anisotropy in the DR1M-PPA film that affects the BSW coupling and propagation. Being TE-polarized and mostly confined at the surface, BSWs are better candidates than Surface Plasmons [50] to sense the in-plane anisotropy [51] inscribed within thin functional azopolymeric films. In the illustrative application reported here and represented in Figure 2.1, an annular grating coupler and a circular bull's eye cavity are inscribed within the DR1M-PPA layer, with the twofold goal of coupling BSWs from free-space radiation and resonantly confining them within the cavity inner region. When a linearly polarized control laser (CW doubled-frequency Nd:YAG) forces the azobenzene molecules to orient,

thus resulting in birefringence, the BSW cavity modes experience spectral shifts that depend on their polarization state. Such a resonance shift is reversible and can be operated several times without significantly degrading the polymeric pattern, with photobleaching effects representing the intrinsic and more critical issue of the proposed tuning mechanism, in terms of repeatability.

2.1 Azobenzenes

In the framework of light responsive materials, it is typical to use chromophore molecules to induce the desired photo-responsivity. One of the most studied photochromic molecules is the so called *azobenzene*, together with its derivatives. These are aromatic molecules that contain two phenyl rings connected by a nitrogen double bond, which is usually referred as azobenzene group. Such bond is absorbent in the UV, and partially in the visible, part of the spectrum. These molecules exhibit the ability of switching between two conformational states, upon absorption of properly energized photons. These two states have distinct spectroscopic and physical properties and, when embedded inside the atomic structure of a material, a switch between the two states can induce a change in the bulk properties of the material [52]. Properties that could include shape, phase, wettability, permeability and solubility [53].

In order to incorporate the photochromic molecule into a polymer, there are few methods. The easiest way is to create a guest-host system by dissolving the molecule into the polymer matrix. Surely cost effective, it might not be very efficient in terms of effects transferred on the hosting polymer. Sometimes the chromophore and the polymer are not soluble in the same solvents or present a very poor solubility, which can induce aggregation or even macroscopic phase separation. Although the above mentioned methods can find applications where they are better suited, to overcome these problems sometimes is possible to chemically attach the azo-molecule to the

polymer backbone. For this activity we exploited a combination of polyphaldehide (PPA) and Dimethyl-red-1-methacrylate (DR1M) which blend together very well, without the need of chemical bonding.

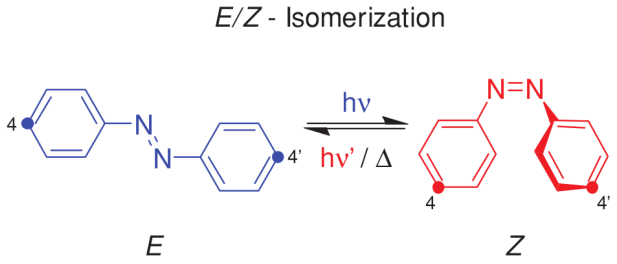

Figure 2.2: Geometrical representation of the photo-isomerization of azobenzene, from *trans* (E) to *cis* (Z). Image taken from [54].

The photo-isomerization of the benzene group occurs between a *trans* and a *cis* state [54], as illustrated in Figure 2.2. The *cis*-form is characterized by a twisting of the phenyl rings at a 90° angle relative to the plane of the azo-bond. These two states are situated in energy wells at slightly different energies, and the energy required to overcome the barrier between the two states can be provided either thermally or optically, depending on the absorption spectrum of the bond.

Since both states are absorbent in the green region of the visible spectrum, exposing the molecule to a green laser can induce a continuous transition between the two states, which can result in a reorientation of the chromophores within the guest polymer. The absorption of photons relies on their polarization orientation in relation to the molecules orientation. Therefore, when exposed to polarized radiation, the azo-molecules tend to reorient in space in such a manner as to minimize absorption. In facts, a molecule that is parallel to the impinging polarization is more likely to transition between the two isomeric states and change its orientation.

In summary, when exposed to a green laser, the molecules tend to align orthogonally with respect to the impinging polarization, thus inducing a preferred

orientation of the microscopic electric dipoles, i.e. inducing an optical anisotropy.

2.2 Bloch Surface Wave tuning by means of azobenzene-polymer blend

Bloch surface waves are renown for their sensitivity to the optical properties of the interfaces between the dielectric multilayer hosting them and the external medium. Therefore, the refractive index change caused by the induced optical anisotropy should be easily detected by their means. A more detailed description of BSWs and their properties can be found in Section 1.4.3. When covering the surface of the multilayer with a few tens of nanometres thick polymer layer, the BSW dispersion is red-shifted according to the well-known dielectric loading effect [55], the extent of which depends on the thickness and the refractive index of the additional layer.

The one-dimensional Photonic Crystal (1DPC) used for this project sustains a TE-polarized BSW and consists of a stack of Tantalia (Ta_2O_5) and Silica (SiO_2) layers on a glass coverslip. The stack sequence being $[Ta_2O_5-SiO2]\times 6-Ta_2O_5-SiO_2$. The Ta_2O_5 layer (refractive index 2.08) is $95nm$ thick, the SiO_2 layer (refractive index 1.46) is $137nm$ thick. The last SiO_2 layer of the stack has a reduced thickness of $127nm$ thick.

2.2.1 Measuring the BSW dispersion

An angularly-resolved spectral reflectivity map is commonly used to investigate the BSW dispersion (see Sections 1.4.3, 1.5.1). To measure it, a home-made setup based on a modified inverted microscope (Nikon Ti2-E) was built. With the sample mounted face-up, illumination is provided from the glass bottom, through an oil-immersion objective (Nikon, NA=1.49), in such a way to probe the BSW by

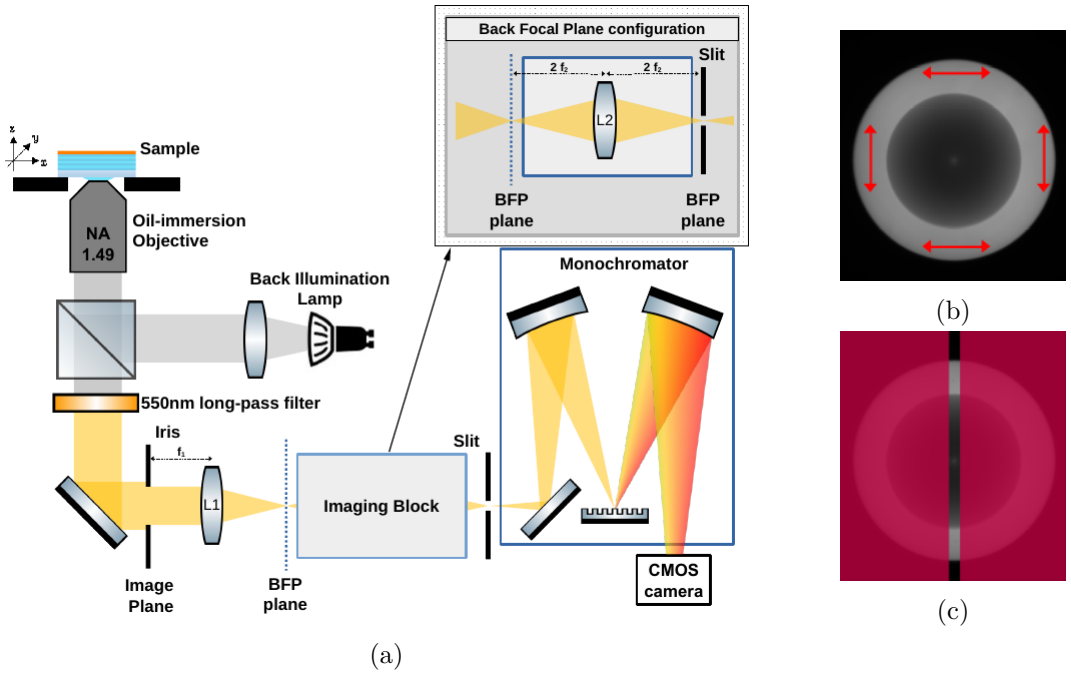

Figure 2.3: (a) Optical setup based on an inverted microscope mounting an oil-immersion objective. The setup allows a white-light illumination from below the sample (the glass substrate side) and collection of the reflected light. Measurements are performed in Back Focal Plane (BFP) imaging. A dispersive spectrometer allows for spectral measurements on selected areas of the collected image. (b) Image of the BFP where the red arrow indicate the polarization of the BSW in the respective regions of the BFP. (c) Image of the BFP where the regions blocked by the monochromator slit are highlighted in red.

tunnelling from the lower most interface of the substrate to the outer most surface, in a very similar way as in a Krestchmann coupling setup. By means of a beam splitter and some collection optics, it is then possible to retrieve the image of the surface of the multilayer and consequently recreate the Back Focal Plane (BFP).

From basic Fourier optics it is known that the BFP of an image contains an approximation of its spatial Fourier Transform. The $x-$ and $y-$ axis of the BFP can therefore be measured in units of normalized wave-vector ($k-space$) and, by projecting the BFP image onto the slit of a monochromator, it is possible to extract the full dispersion of the multilayer (selected along one of the $k-space$ axis by means of the entrance slit as in Figure 2.3c). In the reflectivity map the TE-

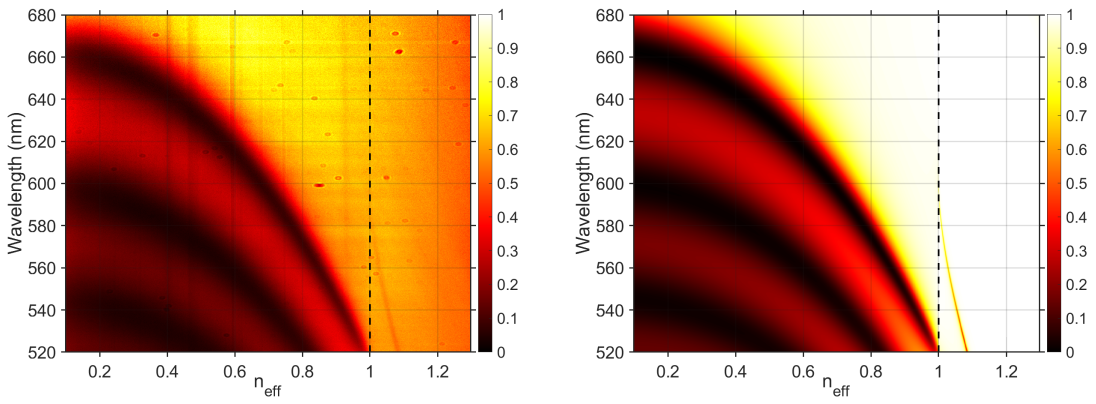

Figure 2.4: Measured (a) and computed (b) reflectivity maps of the 1DPC hosting the BSW. The dispersion of the TE-polarized BSW is shown as an intensity dip. The dielectric multilayer involved is described at the beginning of Section 2.2.

polarized BSW appears as an intensity dip located above the light line, as shown in Figure 2.4 for a bare 1DPC (without the additional layer). According to the reference axes of the optical setup 2.3, the collected light is polarization-filtered so that the reflectivity map and the corresponding BSW are polarized along the $x-$direction.

Upon spin coating the surface of the multilayer with the DR1M-PPA blend, the BSW dispersion shifts depending on the thickness and the refractive index of the new layer. An AFM analysis reveals a polymer film 65 ± 3nm thick. In this case, the refractive index of the polymer blend is unknown but it can be evaluated after quantifying the BSW shift itself. The calculated BSW dispersion showing the best matching with the experimental data (Figure 2.5) is obtained with a real refractive index $n_p = 1.615 \pm 0.022$, obtained after several computing iterations of the Transfer Matrix method.

The estimated refractive index value for the DR1M-PPA blend is in good agreement with a weighted sum of the DR1M and PPA refractive indexes, as seen from previous works [56–58].

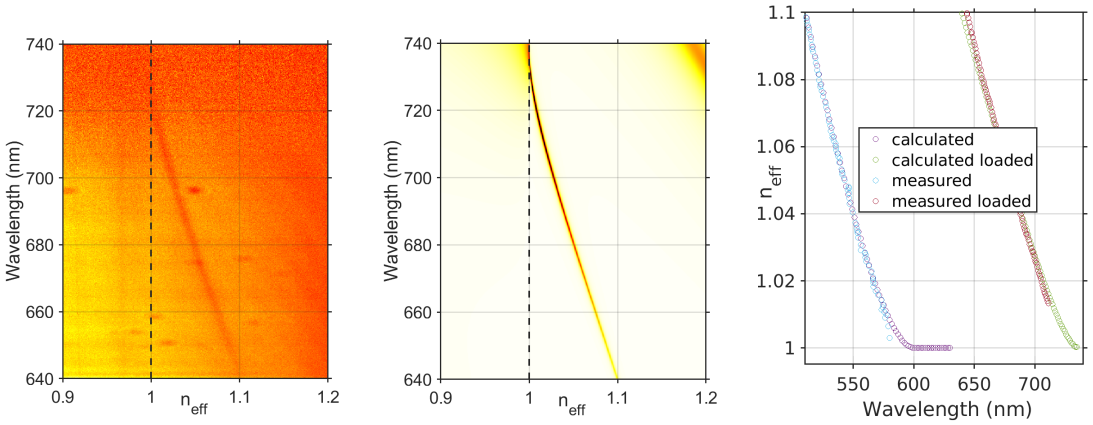

Figure 2.5: Measured (a) and computed (b) reflectivity maps of the 1DPC with a 65nm azo-doped polymeric layer (DR1M-PPA) spin coated on top. The BSW dispersion is show as an intensity dip. In (c) the computed and measured dispersions are compared to those of the multilayer without the additional polymer layer.

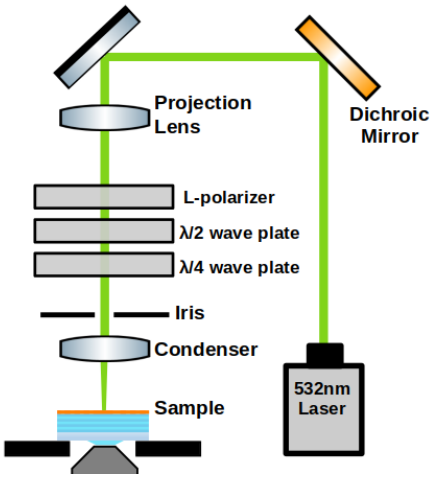

Figure 2.6: Scheme of the laser excitation from the top of the sample.

2.2.2 Excitation of the azopolymer

An expanded laser beam (CW Torus532 from Laser Quantum, now re-branded Novanta Photonics) is used to illuminate the full field-of-view of the collection objective from above the sample. This is needed in order to obtain a uniform optical anisotropy across the spatial domain which is Fourier-transformed onto the

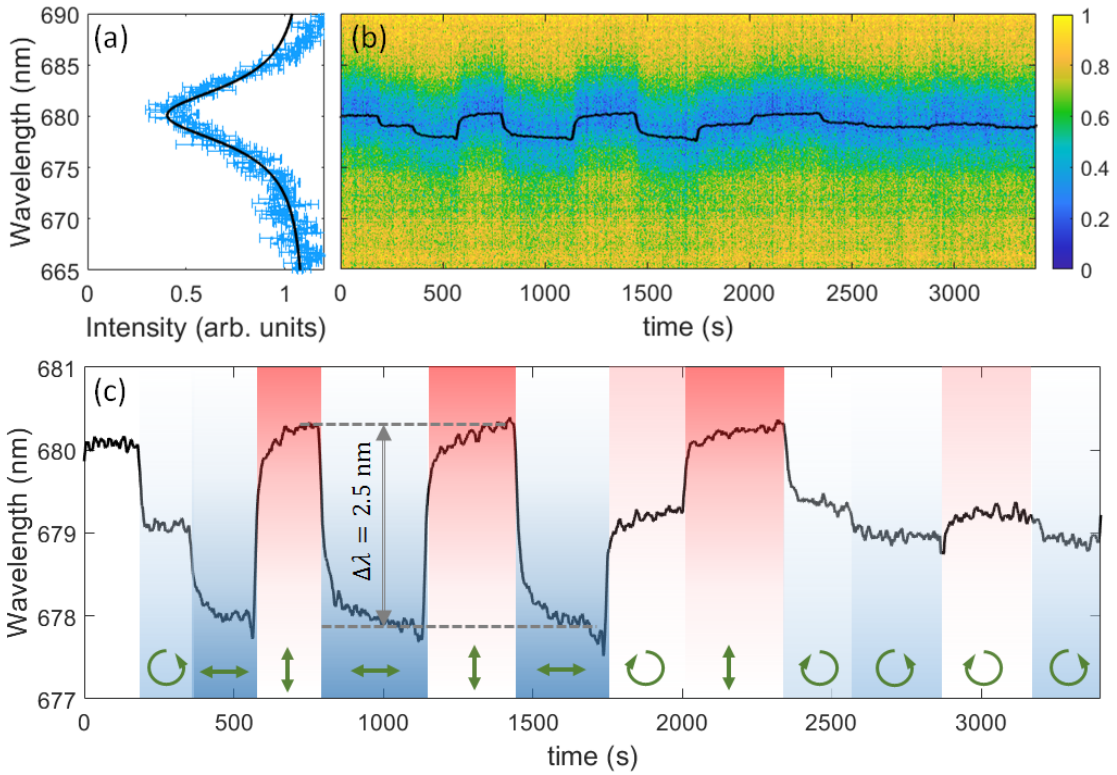

Figure 2.7: Spectral shift of the BSW resonance.(a) Measured spectral profile of the intensity dip associated to an $x-$polarized BSW of $lambda_0 = 680$nm. Uncertainties at each wavelength are evaluated by taking the maximum fluctuation of the intensity signal over 5 frame acquisitions (integration time 1s) in stationary conditions. A Lorentzian fit of the intensity profile is also shown. (b) Time evolution of the BSW resonance during laser irradiation. (c) Time evolution of the central wavelength of the BSW dip obtained after fitting with a Lorentzian function. Green arrows indicate the polarization state of the illuminating laser. An overall spectral range of about 2.5nm is observed in the BSW tuning.

Back Focal Plane (BFP). The laser polarization is controlled by means of a series of polarizers and wave plates, as per Figure 2.6. Measuring birefringence from BFP imaging has been proposed in a recent work involving Surface Plasmon coupling and detection [59]. The measured laser power hitting the sample is 0.88mW (with a spot radius of 2.5mm) and the polarization can be changed from linear (either $x-$ or $y-$oriented) to circular (either left- or right-handed).

An initial $x-$polarized BSW resonance peaked at $\lambda_0 = 680nm$ is monitored over time, as the laser polarization is varied. In Figure 2.7 such BSW resonance is

shown to shift depending on the laser illumination conditions. In order to better evaluate the spectral shift, the BSW dip profile is fitted with a Lorentzian function, whose centre wavelength is plotted over time. To better understand the figure, it is useful to analyse it step by step:

- At first, the laser is OFF.
- After about 180s, the laser is switched ON, in a circular polarization state and the BSW dip is observed to blue-shift by roughly 1nm. This shift is the symptom of a reduction of refractive index in the plane of the 1DPC and can be explained as a combination of two effects. The first results from the azobenzene dipoles driven by the rotating electric field of the laser to orient preferentially out of plane [60]. The second is a consequence of the thermal heating caused by absorption of the laser [1], but it can be ignored in all the other steps since the surface reaches thermal equilibrium very quickly.
- When the laser polarization is set as linear, along the $x-$direction (i.e. parallel to the BSW polarization), the BSW resonance further blue-shifts, as the population of azobenzene molecules oriented along the $x-$axis tends to be depleted. In such a situation, a significant optical anisotropy on the 1DPC plane is produced.
- As a consequence, when the laser linear polarization is rotated parallel to the $y-$axis, a red-shift of about 2.5nm is found.

In this framework, the DR1M-PPA coating behaves as a negative uni-axial crystal having $n_{\parallel} < n_{\perp}$ [61] where the extraordinary refractive index is parallel to the laser polarization direction and the ordinary refractive index is orthogonal.

[1] In facts, the refractive index of a material depends mostly on its density and polarizability Both of these properties tend to increase in most materials when the temperature is increased, reducing the refractive index of the material.

Overall, the observed BSW shift relies on a birefringence, which is in agreement with previous works [62] at comparable irradiation intensity levels ($\approx 18 mW/cm^2$). The red/blue-shift is rather reversible. Interesting to note, the BSW spectral position corresponding to the circular polarization of the laser is roughly located in the middle of the full spectral range of the modulation. However, a closer look reveals that left-handed and right-handed polarizations affect differently the dip position, probably due to some ellipticity of the laser that is not perfectly compensated or a non-perfect behaviour of the wave plates at the operating wavelength of the laser.

2.3 Optical tuning of BSW cavity resonances

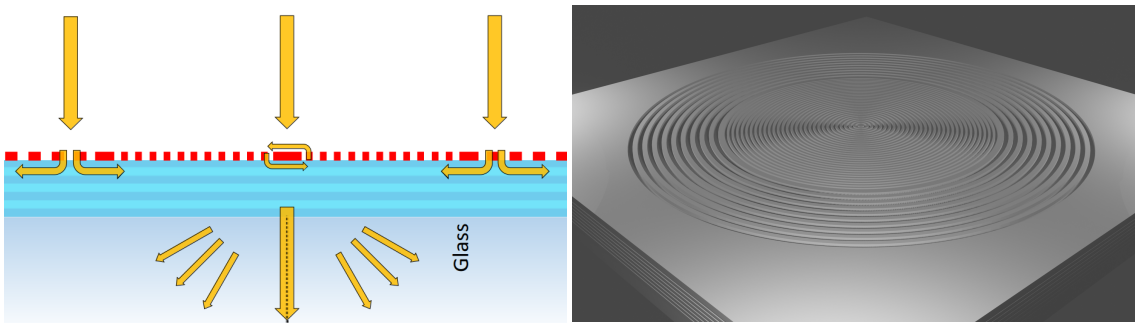

(a) (b)

Figure 2.8: Graphical representation of the gradings composing the coupler and the resonant cavity. In (a) the arrows aid the understanding of the role of each grating, while in (b) a 3D view on the structure is presented.

A major issue in BSW-based devices is represented by the mode coupling with free-space radiation, that is often performed by means of bulky oil-immersion optics, gratings [63–65] and, more recently, with 3D printed refractive couplers [66] and individual Mie scatterers [67]. In our case, an annular diffractive grating inscribed into the DR1M-PPA layer well accomplishes this task. Such a grating allows to couple a white-light beam, slightly focused by the microscope condenser above the sample surface, to BSWs at different wavelengths. Thanks to the grating shape,

BSWs are focused toward the center of the structure [68], where a resonant circular DBR cavity is placed (Fig. 2.8). The latter being similar to the coupling grating, though made of denser periodic corrugations, surrounds a circular central region (here called the spacer), that determines the spectral position of the resonance. Such a resonator represent a type of two-dimensional implementation of a BSW cavity in a nanobeam [69]. In the presented case, BSW coupled from free-space are band-filtered by the DBR during the propagation on the 1DPC surface and possibly resonate within the inner spacer, at specific wavelength(s).

2.3.1 Measuring the resonance

In order to measure the resonance of the proposed cavities, the setup proposed in the previous section is modified slightly. Figure 2.9a shows that illumination is provided from the top of the sample and that the collection optics is modified to observe the image of the direct plane (instead of the back focal plane as per before). The bright-field image of the cavity that we obtain is presented Figure 2.9b. Here, due to the strong transmitted light, the coupling of BSWs and the interaction with the structure cannot be detected. By placing a beam-blocker on the objective BFP (as shown in the inset of Fig. 2.9c), we implement a high-pass Fourier filter on the angular spectrum of the collected light, obtaining the direct plane image in Figure 2.9c. Contributions to this image come substantially from leakage and scattered light related to the BSW excitation. For example, the bright annular region corresponding to the grating reveals the in/out-coupling of BSWs from/to free-space. More interestingly, a bright spot in the cavity center appears as due to the scattering of the cavity modes, after radiation has tunneled from the grating through the DBR.

The central bright spot is then precisely aligned to the input slit of a monochromator, in order to analyse the spectral response of the cavity. The measured cavity spectrum can be observed in Figure 2.10, revealing a broad scattered background

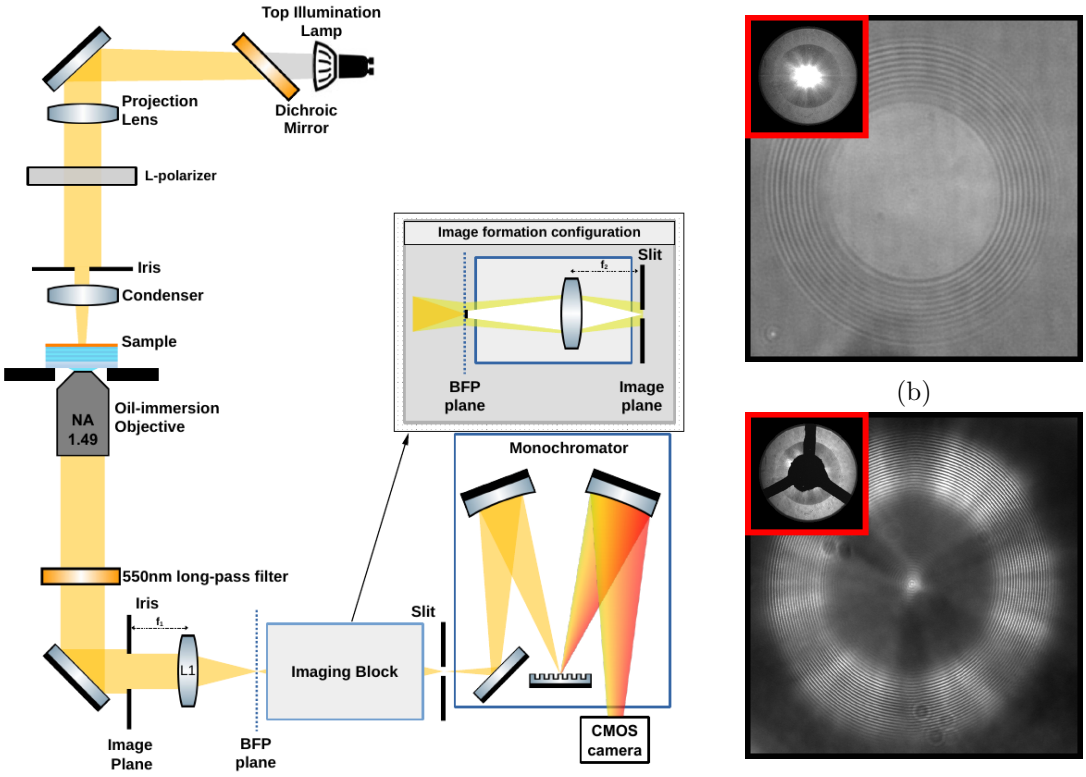

Figure 2.9: Measurements setup scheme. (a) Scheme of the modified optical setup used for measuring the resonance of the cavities. Notice the presence of a beam blocker (BB) at the centre of the back focal plane (BFP) along the optical path. (b) Bright-field image of the cavity obtained without the BB in the BFP. (c) Angularly filtered image of the cavity obtained with the BB in the BFP. Red insets show images of the BFP with (c) and without (b) beam blocker.

surmounted by two peaks. These two peaks are detected at $\lambda_B = 584.5$nm and $\lambda_R = 597$nm. After inserting a polarizer along the collection path, we found that the two peaks have maximum intensity corresponding to two orthogonal polarizations for the collected light. In facts, as the orientation of the polarizer is varied, the intensities of the two peaks are complementarily modulated, as illustrated in Figure 2.10c. Specifically, the short-wavelength mode ($\lambda_B = 584.5$nm) reaches the maximum of intensity when the transmissive axis of the polarizer is parallel to the $x-$axis ($\alpha = 0$). Conversely, the long-wavelength mode ($\lambda_R = 597$nm) has the

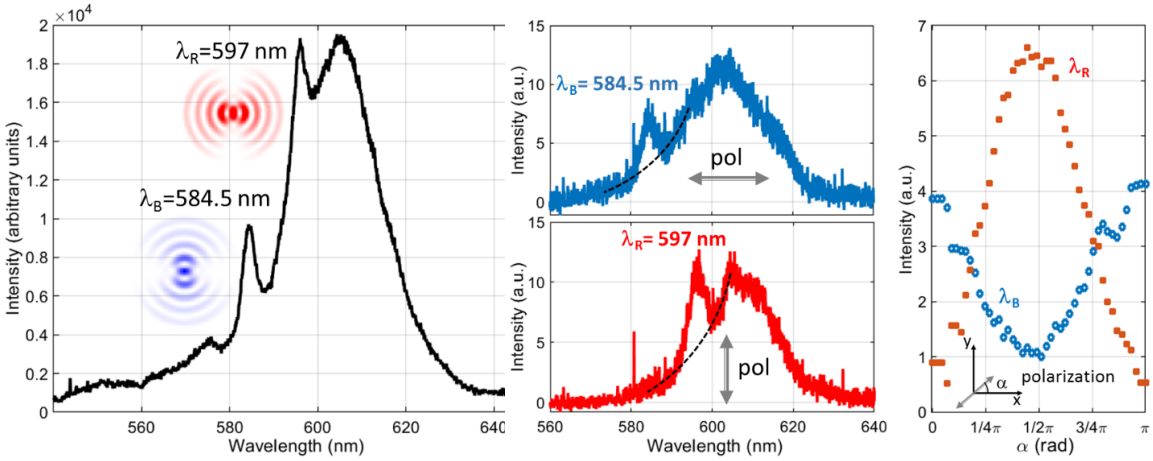

(a) (b) (c)

Figure 2.10: Measured spectrum of the bright spot resonating at the centre of the cavity highlighting the presence of two resonance peaks. (a) Unfiltered spectrum. (b) Spectum obtained by polarizing the illumination light showing that the two peaks can be excited independently, for two orthogonal polarizations. (c) Dependence of the intensity of each peak on the illumination polarization angle.

maximum at $\alpha = \pi/2$, indicating a polarization parallel to the $y-$axis.

AFM analysis of the cavity

The direct nanopatterning of the DR1M-PPA film has been possible by means of a novel thermal-Scanning Probe Lithography (t-SPL) that is able to control the local sublimation of the polymer layer thanks to the action of a sharp silicon tip providing temperature and time controlled heat pulses [70] (Nanofrazor Scholar system, Heidelberg Instruments). By exploiting this nanolithographic technique, all dielectric photonic cavities can be nanopatterned at the surface of functionalized polymer layers, achieving high spatial resolution at the subwavelength scale.

The PPA-DR1M layer is about 65 nm thick. This permits to obtain: (i) a BSW dispersion spectrally far enough from the DR1M absorption maximum; (ii) a good spatial resolution of the patterned features in t-SPL. In fact, for thinner films we observed a strong damping of the BSW resonant mode due to absorption losses, while for thicker films the quality of the lithographed structures was increasingly

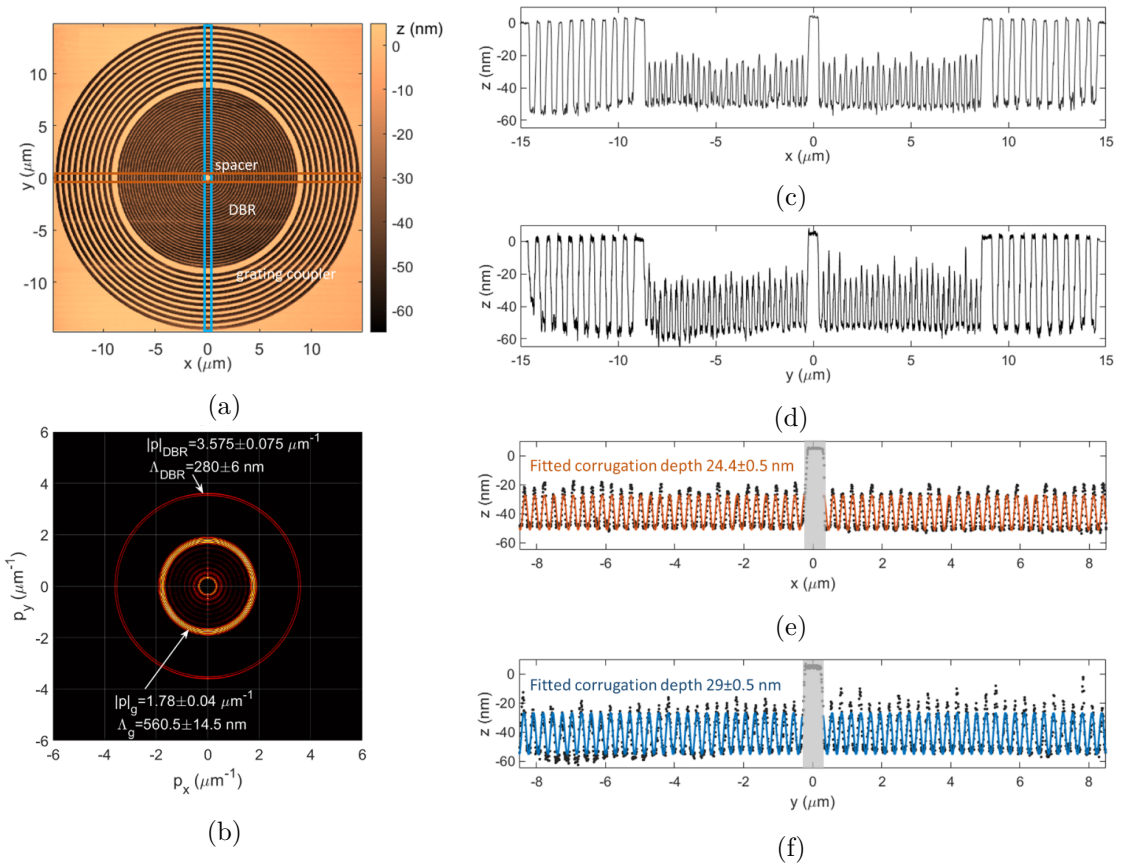

Figure 2.11: Topography of the DR1M-PPA structure. (a) Topography map. Blue and red boxes define the integration regions for plotting the cross sections; (c) horizontal ($x-$direction) and (d) vertical ($y-$direction) cross sections of the pattern; (b) modulus of the Fourier Transform (FFT) calculated from the topography map. The zero-order is masked to zero. The two modulations related to DBR and grating coupler are indicated together with the estimated periods; experimental data and fitted profiles of the DBR corrugation along (e) the $x-$direction and (f) the $y-$direction. The fitting curve is a single-frequency harmonic term. The modulation depths estimated after the fit are indicated for both orthogonal profiles

deteriorating.

Figure 2.11a shows the topographic image map acquired in-situ by the Nanofrazor system, exploiting the same tip to scan the patterned region in contact mode. The $xy-$ axis indicated in the figure define the reference system used throughout this work. In Figure 2.11c and 2.11d the horizontal ($x-$direction) and vertical ($y-$direction) profiles of the structure topography are shown. It is possible to appreciate a lower modulation amplitude of the DBR as compared to the outer grating coupler, which spans across almost the total film thickness (which is approximately 65nm thick). A two-dimensional Fast Fourier Transform (FFT2) of the topography map is calculated (Fig. 2.11b), revealing two bright rings associated to the periods of the grating coupler Λ_g and the DBR Λ_{DBR}. After the FFT2-based spatial frequency analysis, we estimate $\Lambda_g = 560.5 \pm 15.5$nm and $\Lambda_{DBR} = 280 \pm 6$nm, which are well matching the design parameters.

Worth to note that the FFT amplitude of the frequency term related to the DBR exhibits a slight anisotropy, suggesting that the modulation depth of the DBR may vary with the azimuthal angle, over the plane. Although very small, the depth modulation difference in the DBR along the two orthogonal directions is not negligible as it introduces a detectable optical anisotropy of the cavity, causing a splitting of the BSW resonances into two orthogonally polarized modes at different energies.

Computational modelling, FDTD

In order to evaluate the effect of the topological anisotropy, we carefully fitted the DBR AFM profiles along the $x-$ and $y-$ directions by using a single-frequency harmonic function given by a linear combination of a sine and a cosine (in addition to a baseline, constant term). Results are shown in Figure 2.11e and 2.11f. In the fitting procedure, the inner spacer has been excluded (shadowed region) and

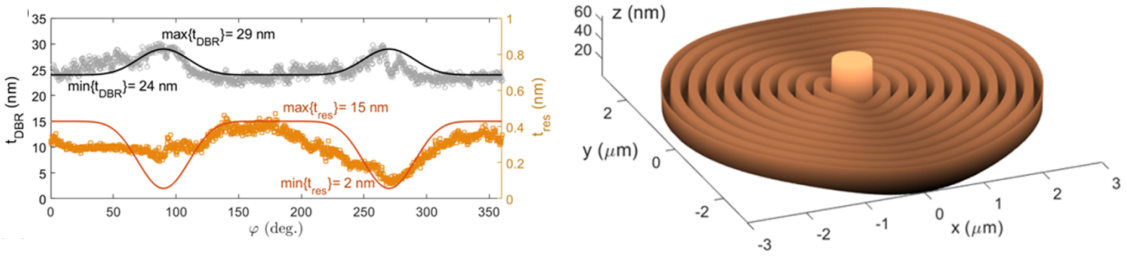

(a) (b)

Figure 2.12: (a) Azimuthal profile of the DBR modulation thickness (grey circles) and the residual layer thickness (orange squares) from the AFM analysis together with the analytical profile (black solid line) and (orange solid line) used in the FDTD model. (b) Topographic radial profile of the cavity spacer, averaged over. For clarity of illustration, only few DBR periods are shown in the image.

the profile portions beforehand and afterwards the spacer have been fitted separately. The average corrugation depths obtained from the fit along the $x-$ and $y-$ directions are $h_x = 24.4 \pm 0.5$nm and $h_y = 29 \pm 0.5$nm.

Then, a two-dimensional Finite Difference Time domain (FDTD) model based on the effective index approximation is used to compute the spectral response of the circular cavity only, without explicitly keeping into account the multilayer beneath and the outer annular grating. According to this 2D approximated model, each relief with a given thickness has an associated effective refractive index defined by the BSW dispersion on a flat 1DPC loaded with a uniform DR1M-PPA film with the same thickness. It is thus assumed that the effective refractive index of the reliefs is not affected by the lateral size of the reliefs themselves. In the present case, the effective refractive dispersion is modelled according to the structure topography, in order to take into account the anisotropy along the azimuthal angle φ on the $xy-$plane. The experimental DBR modulation and the residual layer thickness extracted from the AFM analysis are shown in Figure 2.12 together with the DBR modulation profile $t_{DBR}(\varphi)$ and the residual layer profile $t_{res}(\varphi)$ employed in the FDTD model. The spacer width is set to $W_{spacer} = 640$nm, which is consistent with the measured profile. Accordingly, the resulting cavity profile ($Z_{cavity}(r, \varphi)$)

in polar coordinates is:

$$Z_{cavity}(r,\varphi) = \begin{cases} \frac{A+B}{2} + \frac{A-B}{2} \cdot sign\left[cos\left(K_{DBR}\left(r - 0.5W_{spacer}\right)\right)\right] & \text{if } r > 0.5 \cdot W_{spacer}, \\ C & \text{if } r < 0.5 \cdot W_{spacer}, \end{cases} \tag{2.1}$$

with $K_{DBR} = 2\pi/\Lambda_{DBR}$, $A(\varphi) = (t_{res}^{max} + t_{res}^{min}) + (t_{res}^{max} - t_{res}^{min}) \cdot (1 - sin^8\varphi)$, $B(\varphi) = t_{res}^{min} + (t_{res}^{max} - t_{res}^{min}) \cdot (1 - sin^8\varphi)$, $C = 65$nm. The polar coordinates can be obtained as $r = \sqrt{x^2 + y^2}$, $\varphi = arctan(x/y)$.

In Figure 2.13 the modelled topographic profiles along the $x-$ and $y-$directions are presented as well. Cavity modes are excited by inserting an emitting dipole in the spacer centre, with momentum orientation either parallel to the $x-$axis $\vec{p}_{0^\circ} = (p,0)$ or parallel to the $y-$axis $\vec{p}_{90^\circ} = (0,p)$ and calculating the intensity of the radiation flowing out of the cavity, as detected by monitors M_φ at $\varphi = [0^\circ, 90^\circ]$ outside the DBR. Intensity $I(M_\varphi, \vec{p}_\theta)$ indicates the intensity detected at monitor M_φ emitted by the source $\vec{p}_\theta$.

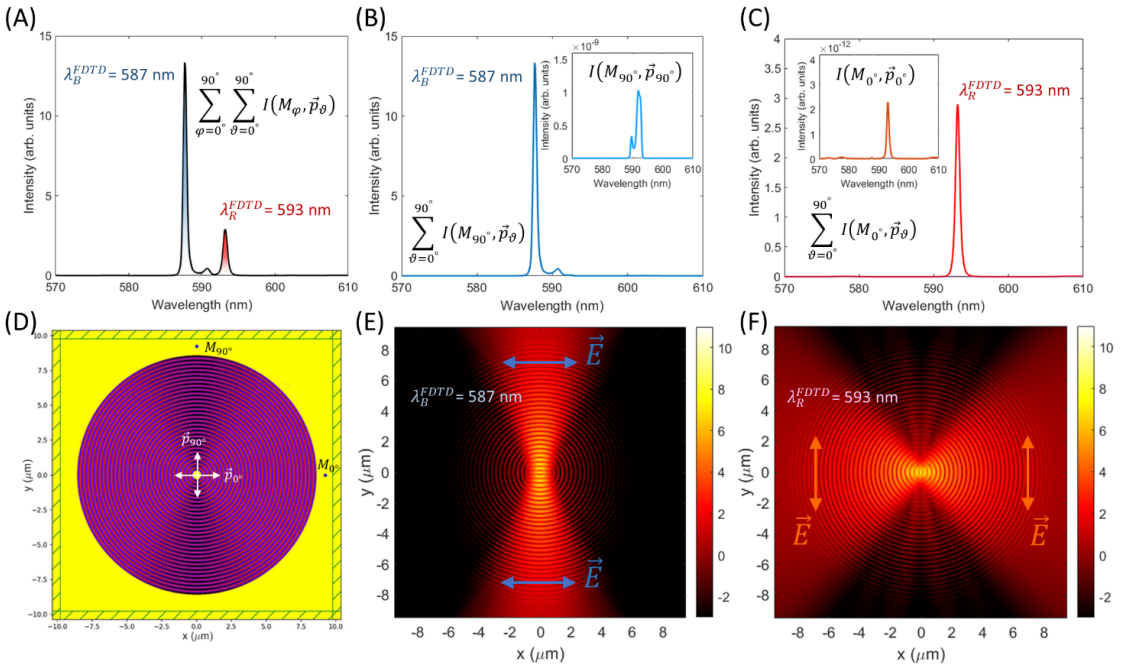

Figure 2.13: 2D FDTD model of the BSW cavity. (A) Sum of intensity spectra collected by M_{0° and M_{90° produced by an incoherent superposition of sources $\vec{p}_{0^\circ}$ and $\vec{p}_{90^\circ}$; (B) intensity spectrum collected by M_{90°, produced by $\vec{p}_{0^\circ}$ and $\vec{p}_{90^\circ}$ incoherently superposed. Inset: spectrum at M_{90°, produced by $\vec{p}_{90^\circ}$ showing a negligible contribution to the mode coupling at λ_R^{FDTD}; (C) intensity spectrum collected by M_{0°, produced by $\vec{p}_{0^\circ}$ and $\vec{p}_{90^\circ}$ incoherently superposed. Inset: spectrum at M_{0°, produced by $\vec{p}_{0^\circ}$ showing a negligible contribution to the mode coupling at λ_B^{FDTD}; (D) Geometry of the FDTD model with monitors M_{0° and M_{90° on the $x-$axis and $y-$axis, respectively. The two orthogonal sources are in the cavity centre as shown by white arrows; intensity distribution at (E) λ_B^{FDTD} and (F) λ_R^{FDTD}. Both intensity distributions are calculated by the incoherent sum of the intensity distributions from the two source p_{0° and $\vec{p}_{90^\circ}$. Colour scale is logarithmic. Arrows indicate the orientation of the electric field on the reference axes.

2.3.2 Tuning the cavity resonances

The two cavity modes with substantially orthogonal polarizations and spatial distributions are suitable for probing the in-plane anisotropy induced on the DR1M-PPA structure. After background subtraction, the cavity modes are spectrally monitored as shown in Figure 2.9. In Figure 2.15 the time evolution of the spectral position of the cavity modes is illustrated, while the cavity is illuminated with the laser beam in different polarization, as per Fig. 2.14 (laser power 0.16mW,

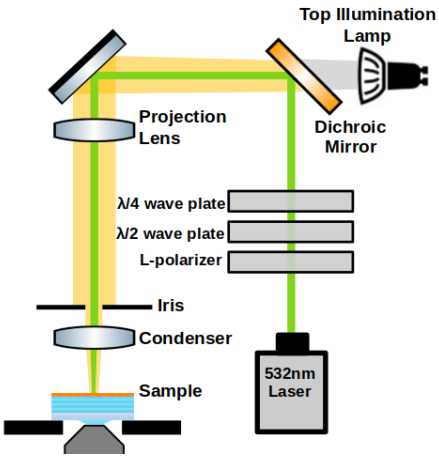

Figure 2.14: Extension of setup in Fig. 2.9, that includes laser illumination and polarization control.

laser spot diameter 50μm). In order to monitor both peaks, no polarization filters have been inserted along the illumination and the collection paths. Figure 2.16a shows a more detailed view of the mode peak positions over time. The opposite spectral shifts of the two modes is evident and can be explained by invoking the mechanism underlying the formation of optical anisotropy previously illustrated. As the laser is linearly polarized along the $x-$direction, the $x-$polarized mode peak blue-shifts because of a smaller extraordinary refractive index induced in that direction. Conversely, the $y-$polarized mode experiences a slight red-shift because more DR1M dipoles tend to be oriented in the $y-$ and $z-$direction. The situation is inverted when the laser polarization is rotated by 90 degrees.

Thanks to the capability of the DR1M-PPA compound to sense the polarization state of the illuminating radiation [71, 72], we detected some asymmetry in the peak shift when a circularly polarized light with opposite handedness is used. This suggests that the laser polarization is likely to be slightly elliptical. When the laser is switched off, the optical anisotropy induced in the DR1M is kept as long as the thermal relaxation process allows it. By looking the relative spectral shift an overall tuning of $\Delta\lambda = 1.5$nm between the two modes is found (Figure 2.16b),

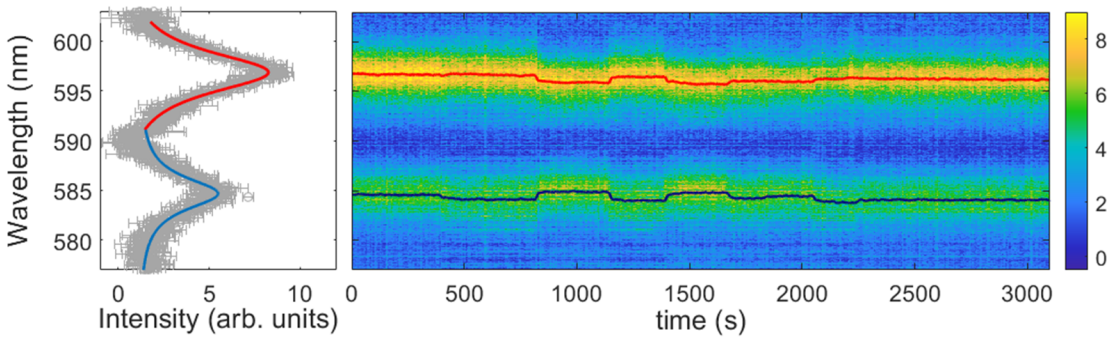

Figure 2.15: Spectral shift of the cavity resonances. On the left, the (background subtracted) measured spectral profiles of the intensity peaks associated to the two resonant modes of Figure 2.10. A Lorentzian fit of the intensity profile is also shown. On the right, time evolution of the resonances during laser irradiation.

with a rather accurate recovery of the initial condition after the laser is switched off. The optical anisotropy here is induced only on a very small area, contrary to the case of BSW propagating on the flat 1DPC with a homogeneous DR1M-PPA coating, where the laser spot covered the full field of view of the collecting objective (because of the BFP-based detection).

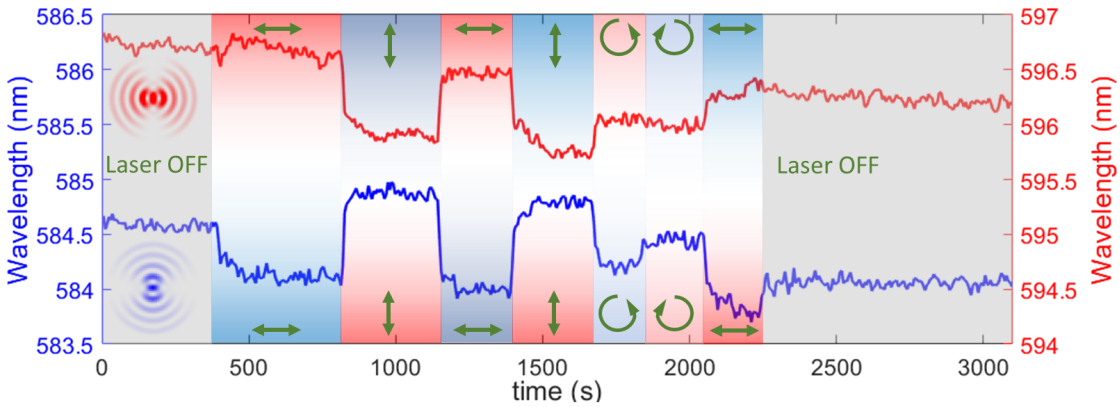

(a)

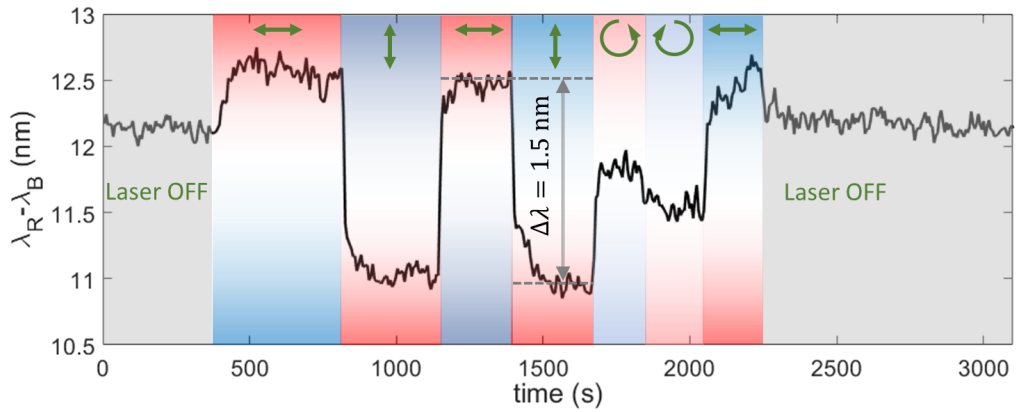

(b)

Figure 2.16: (a) time evolution of the central wavelengths and obtained after fitting. Green arrows indicate the polarization state of the illuminating laser: $y-$oriented (vertical), $x-$oriented (horizontal), left- or right-handed. (b) time evolution of the relative spectral shift of the orthogonal cavity modes ($\lambda_R - \lambda_B$. A tuning over about 1.5nm spectral range is demonstrated.

2.4 Concluding remarks

This chapter presented a hybrid nanophotonic device that combines a dielectric photonic crystal (1DPC) made of amorphous materials with a light-responsive flat-optics structure based on a functionalized polymeric blend. In particular, a resonant cavity for BSWs is nanofabricated into a thin azobenzene-containing polymer layer deposited on top of a high-quality 1DPC via thermal-Scanning Probe Lithography. The photo-switching of the azobenzenes is exploited not only to produce

an overall reversible change of the refractive index but also optically inscribes an optical anisotropy. Differently from other methods exploiting e.g. thermo-optical, mechanical or electro-optical effects [73] the all-optical control allows a precise selection of very localized regions (such as tiny recesses), which makes this approach very attractive for densely packed devices.

By leveraging the ability of the polymeric structure to produce an in-plane anisotropy after proper laser irradiation, the possibility to perform a complex manipulation of the response of resonant structures for surface waves was demonstrated, provided the cavity modes are TE-polarized, as in the case of BSWs. The cavity itself exhibits topographic nanofeatures that make it resonating according to two orthogonally polarized modes, at different energies. The optically-controlled anisotropy of the azobenzenes allows the spectral positions of the resonant modes to be tuned in several ways. For example, an illumination with a circularly polarized laser causes an isotropic decrease of the in-plane refractive index components, so that both modes can be simultaneously blue-shifted, starting from a configuration of zero birefringence. Moreover, the same illumination with a circular polarization can produce a red-shift on one mode and a blue-shift on the other, in case an initial in-plane anisotropy is already inscribed into the polymer. When a linearly polarized laser is used, a strong decrease of refractive index in the polarization direction is observed, thus resulting in a blue-shift of the cavity mode polarized in that direction and a typical red-shift of the orthogonal mode. In conclusion, by using moderate laser power densities, we have shown that the cavity resonance wavelengths can be easily shifted over a range of about 1.5 nm, with time constants of about 10-20 seconds. Potential improvements of this result are expected in case more efficient light-responsive units capable of larger optically-induced birefringence are employed [74].

In a more general perspective, integrating a light-responsive layer within dielectric photonic structures provides an additional degree of freedom for surface

patterning and an optically addressable mean for controlling birefringence without significantly affecting the optical response of the structure underneath. The quality of the surface modes considered here is still rather high, with resonance widths much smaller than many plasmonic counterparts, because of the lower losses. We anticipate that applications of this approach can be particularly foreseen in emitting photonic devices [75] hosting extended [76–79] or single sources [80–85], wherein the photonic modes can be finely adjusted in polarization and energy to match the emitter orientation [86, 87] and wavelength, generally aiming at a coupling optimization.

Chapter 3

Computational modelling of metasurfaces for BSWs diffraction and resonance

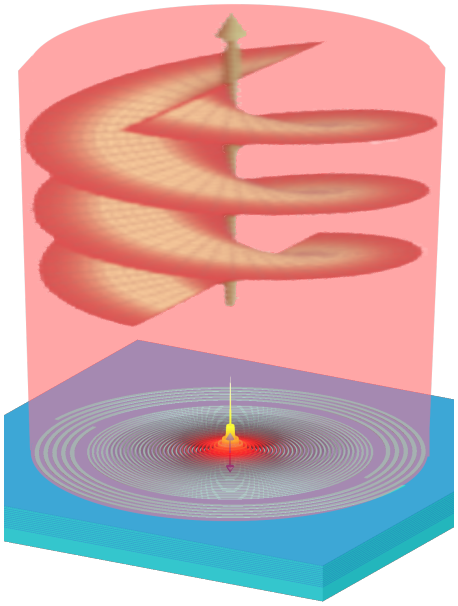

Figure 3.1: Suggestive representation of the device proposed in the present Chapter.

Orbital angular momentum (OAM) has demonstrated significant potential in

communication and information technologies, especially thanks to its inherent ability for multiplexing [88, 89]. Ever since the advent of the OAM-entangled photon pair [90], and with the possibility of generating high dimensional quantum spaces [91], it held promise for applications in quantum technologies [92, 93]. Even applications like optical tweezers [94] and microscopy imaging [95], have made use OAM to improve their abilities.

Various techniques have been developed to generate optical vortices. These include the use of spiral phase plates [96], commonly used to imprint a phase ramp onto an incoming beam; computer-generated holograms [97], by means of phase masks; spatial light modulators [98], used to impose a phase pattern on an incident beam, which can then be converted into an optical vortex; q-plates [99], that use a birefringent material to induce a specific phase shift on an incident beam; and even metasurfaces [6, 7, 100].

However, generating photon sources that emit single photons with orbital angular momentum properties is more challenging, since it requires precise control over the quantum states of individual photons. Additionally, the efficiency of single-photon sources with orbital angular momentum properties is typically much lower than that of conventional single-photon sources. Previous work has explored the use of plasmonic metasurfaces for this purpose [9]. Here, we investigate an optical platform based on an all-dielectric structure hosting Bloch Surface waves, that offers a promising alternative for generating single-photon vortices.

In this chapter, computational analysis is performed with a combination of Finite Difference Time Domain (FDTD) simulations and Transfer Matrix Method (TMM), the former performed either with Lumerical [32] and/or Meep [33], while the latter using a self implemented version written in MATLAB [29].

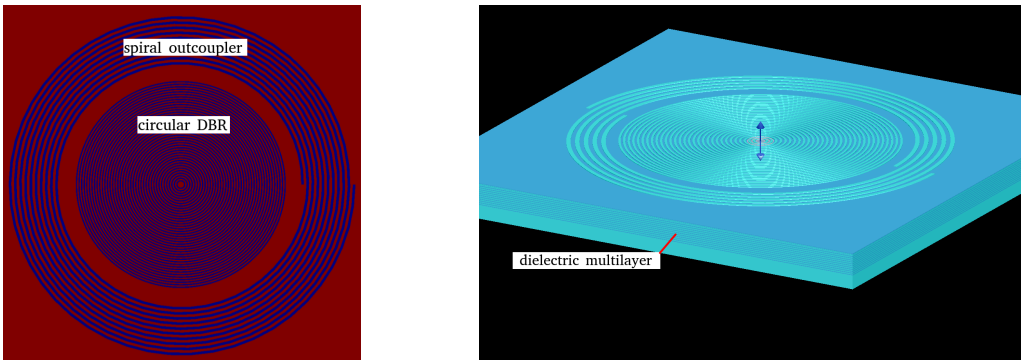

(a) (b)

Figure 3.2: Top view (a) and perspective view (b) of the proposed device where the three main elements are highlighted.

3.1 Design of grating outcouplers for Orbital Angular Momentum generation

In a prior investigation [101], two-dimensional Archimedean spirals possessing intrinsic topological charge were utilized as a mean of imparting orbital angular momentum to circularly polarized laser beams. Building upon this idea, in this chapter, we present and examine a two-dimensional planar structure placed atop a one-dimensional photonic crystal (1DPC) that enables the manipulation of the field generated by a dipole-like emitter source.

The proposed structure is composed of three components:

- a dielectric multilayer supporting a Bloch Surface Wave (BSW);
- a circular Fabry-Pérot resonant cavity;
- a circular diffractive grating.

Figures 3.2a and 3.2b depict the proposed structures.

The emitter is coupled with the BSW by placing it on the surface of the multilayer. The BSW field distribution is predominantly confined between the outermost

layer of the 1DPC and the external medium, resulting in a higher density of optical states at the dipole's location. This favors emission into the BSW, producing a field distribution that propagates in two dimensions from the dipole. To exploit the radial symmetry of the field, the dipole moment must be aligned orthogonally to the multilayer surface. This requires the BSW to be transverse magnetic (TM) to couple properly with the emitter.

The circular resonant structure around the dipole, which is nothing but a distributed Bragg reflector (DBR), is employed to enhance the coupling with the BSW through the Purcell effect, as previously demonstrated by Stella et al. [102].

Finally, the external diffractive grating is utilized to manipulate and decouple the BSW, resulting in an outward-propagating beam with arbitrary OAM properties.

The diffractive grating is the most crucial component for OAM generation. Following the approach taken by Stella et al. [101], we investigate spirally shaped gratings to manipulate a BSW into a vortex beam. As will be shown in subsequent sections, this type of grating is incapable of generating vortex beams with a single polarization. Therefore, in addition to spiral-shaped gratings, we investigate the use of metasurfaces gratings within our structures.

3.2 Orbital Angular Momentum manipulation with grating outcouplers

As previously stated, simulations of the device were conducted using either Meep or Lumerical. In both cases, the simulation domain consisted of the following elements, as depicted in figure 3.3:

- A dielectric multilayer, with the final layer patterned with the outcoupler

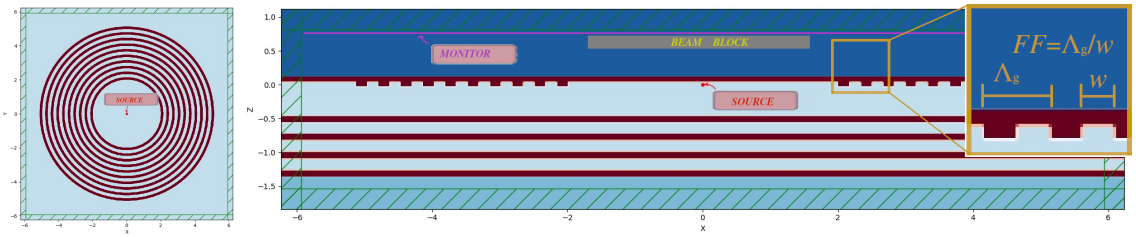

(a) (b)

Figure 3.3: Top view (a) and side view (b) of the simulation domain where the main components of the simulations are highlighted. The inset in (b) highlights the parameters of the grating outcouplers: period Λ_g and fill factor FF.

grating;

- A TM-oriented dipole source located at the center of the grating, positioned in the middle of the last dielectric layer;
- A circular metallic beam blocker situated a few hundred nanometers above the source;
- A near-field monitor positioned above the entire structure to detect the outcoupling field.

More information on the specific multilayer used can be found in Section 3.4.2. For all the presented results, the multilayer parameters can be found in Figure 3.18. The scripts used for generating the simulation domains can be found in [35, 36].

For the purpose of studying the grating outcouplers, it was not necessary to include the circular distributed Bragg reflector (DBR) cavity in the simulation domain. This was because the temporal coherence and coupling on the multilayer could be temporarily neglected by a strategic use of the detectors. In facts, in an FDTD simulation, the temporal coherence determines the duration of the simulation, since this latter is typically interrupted when the fields in the simulation domain have been decayed properly. Since the detector performs a Fourier transform, one doesn't need to simulate a long time, single frequency, simulation, but

a short, pulsed simulation is usually sufficient. The beam blocker, instead, was used specifically to allow the detector to collect radiation emanating mainly from the outcoupled BSW, while avoiding radiation originating directly from the dipole source. It was demonstrated that by increasing the coupling of the source using the DBR cavity, thanks to the Purcell effect, the simulations can produce the same results without the need for the beam blocker.

3.2.1 Circular gratings

In order to comprehend how spiral outcouplers can impart momentum to the field, it is imperative to first analyze circular grating outcouplers.

These gratings can be designed using the rules for standard linear diffraction gratings even though they possess radial symmetry. Which is, in facts, possible due to the radially symmetric field produced by the dipole at the center. Utilizing the effective index approximation proposed in Section 1.5.2 and the knowledge on diffractive gratings from Sections 1.2.3 and 1.4.2, the grating wavevector can be designed such that the Bloch surface wave is diffracted, at the first order, orthogonally with respect to the multilayer surface. The wavevector and period of a grating (K_g and Λ_g) can be related to the wavevector of a BSW (k_{bsw}), as well as the effective index of the BSW (n_{eff}) and the free space wavelength of the energy at which the device is designed (λ_0), through the following equation:

$$K_g = \frac{2\pi}{\Lambda_g} = k_{bsw} = n_{eff}\frac{2\pi}{\lambda_0}. \tag{3.1}$$

However, the effective index of the BSW cannot be uniquely defined in the region of the grating, as it should be defined in a region where the last dielectric layer is uniform. Nonetheless, in that region, one may assume the coexistence of two different effective indices and utilize a weighted average. One associated to the BSW assuming the last layer to be as high as the highest part of the grating

($n_{eff,h}$), and the other one assuming the last layer to be as high as the lowest part of the grating ($n_{eff,l}$). By then taking a weighted average, over the fill factor (FF) one obtains :

$$k_{bsw} = 2\pi \frac{n_{eff,h} \cdot FF + n_{eff,l} \cdot (1 - FF)}{\lambda_0}, \tag{3.2}$$

Using these equations, the grating period can be computed as:

$$\Lambda_g = \frac{\lambda_0}{n_{eff,h} \cdot FF + n_{eff,l} \cdot (1 - FF)} \tag{3.3}$$

From the sketch of a section of the device, shown in Figure 3.3, the behavior of the outcoupled field can be easily understood. The Bloch surface wave propagates on the surface with its electric field perpendicular to the surface. When it reaches the outcoupler, the field is ideally reoriented parallel to the surface, but still perpendicular to the groove lines, and then it propagates freely. Since the grating has a finite size (a finite number of periods), in practice it diffracts in a narrow lobe around the grating normal, the width of which determined by the number of periods. Due to this angular width of the diffraction, in the far field, beams propagating from the left and right sides of the grating overlap, producing a pattern that defines the shape of the propagating beam. Since these two beams originate from BSWs propagating in opposite directions, even if they follow same-length paths, they are phase shifted by π radians from each other. This implies that at the center of the far field the two beams will interfere destructively. For angles slightly off the normal to the multilayer, the difference in path is sufficient to produce constructive interference.

As demonstrated by the results in Figure 3.4, when considering the entire circular outcoupler, the resulting propagating field consists of a doughnut-shaped beam that is propagating in a narrow solid angle, and which polarization is oriented radially with respect to the beam center. The far-field intensity maps were obtained

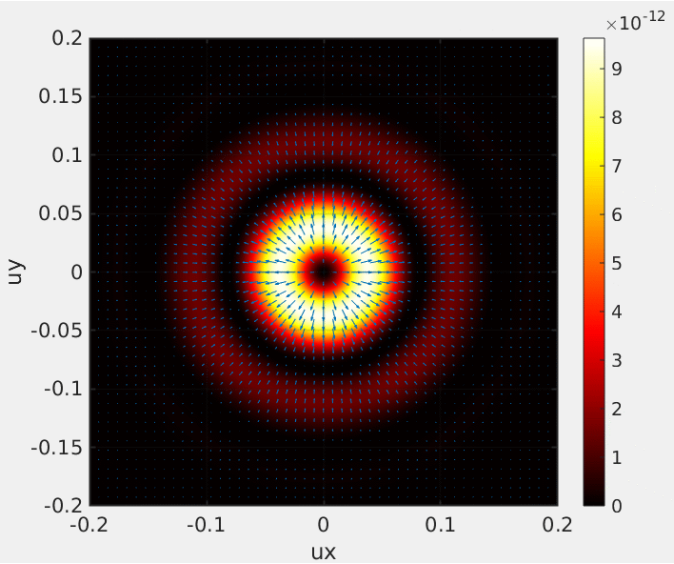

Figure 3.4: Far field intensity map for a circular grating outcoupler. The design parameters are $\Lambda_g = 330\text{nm}$, $FF = 0.5$ for $N = 10$ periods, designed to work at $\approx 570\text{nm}$ of wavelength. The arrows highlight the radial direction of the polarization in the doughnut shaped beam.

using the Rayleigh propagation formula for free-space propagation, starting from the near-field profile (module and phase) obtained from the monitor. The latter was obtained from the FDTD simulation by computing the Fourier transform of the time-evolving field at the monitor coordinates in real-time.

To analyze the angular momentum properties of the beam, it is essential to study its polarization state, thus decompose the field into its orthogonal components. Using the circular polarization base for the decomposition is preferable for obvious reasons. From Figure 3.5, it can be observed that the two polarizations have identical field intensities that overlap, but with different phase profiles.

The helical shape of the latter is particularly evident, indicating the presence of orbital angular momentum (OAM) in both propagating beams. In particular, the two polarizations have opposite OAM, as the two helices have different handedness, with OAM number $l = \pm 1$. Considering that the number of helices in the phase

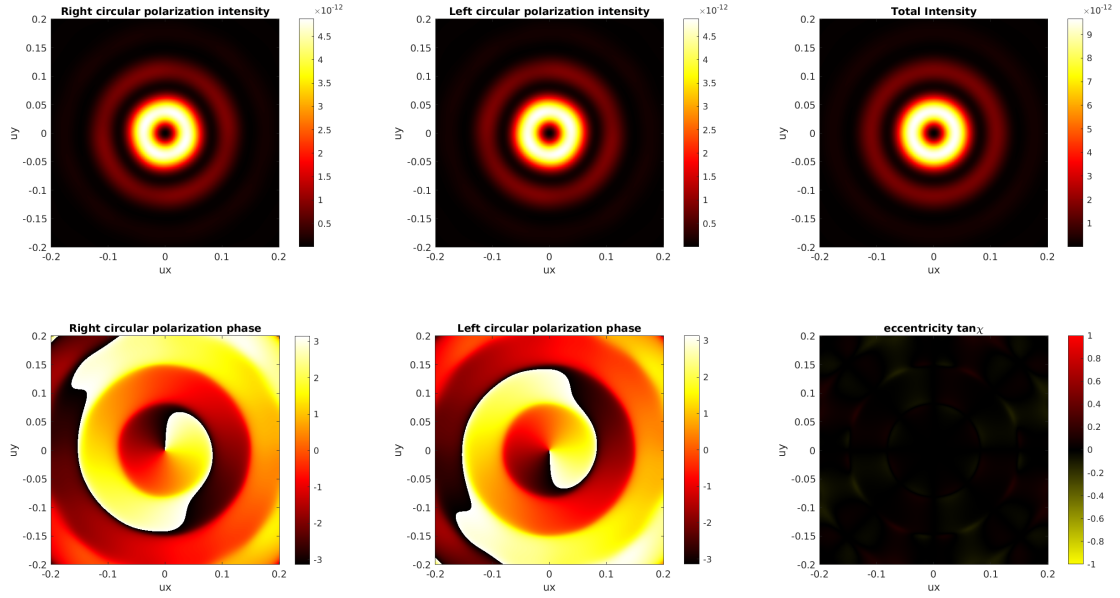

Figure 3.5: Decomposition of the far field for a circular outcoupling grating. From the phase profile the helical shape is proof of presence of orbital angular momentum. The two polarization having OAM number $l = +1$ for LHC and $l = -1$ for RHC.

profile determines the OAM number, while the handedness determines the sign.

The total angular momentum of a photon carried by the radially polarized beam can be computed by adding the polarization momentum with the orbital momentum. To do so, it is necessary to clarify the convention regarding the orientation of the momenta:

- Right handed circular (RHC) polarization rotates in the clockwise direction, with momentum number $\sigma = +1$.
- Left handed circular (LHC) polarization rotates anticlockwise, with momentum number $\sigma = -1$.
- Positive OAM numbers ($l > 0$) refer to an helical phase profile increasing in the clockwise direction.
- Negative OAM numbers ($l < 0$) refer to an anticlockwise increase of the phase.

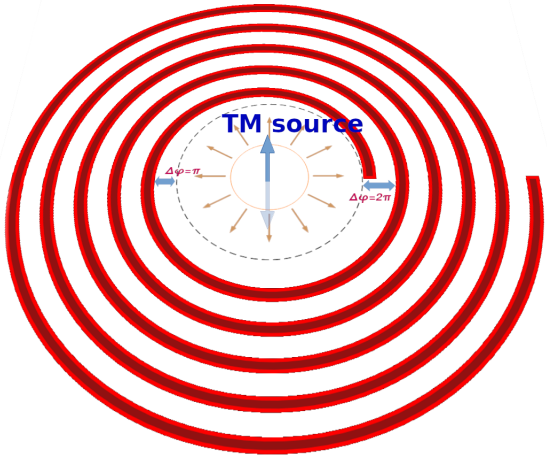

Figure 3.6: Sketch of a spiral grating outcoupler. The spiral shape introduces an angle dependent phase delay to the circular wave originating at the center from an electric dipole.

Observing Figure 3.5 again, it can be concluded that for both polarizations, the total angular momentum (M) is equal to zero:

$$J = \hbar(\sigma + l), \tag{3.4}$$

$$J_{RHC} = \hbar(+1 - 1) = 0, \tag{3.5}$$

$$J_{LHC} = \hbar(-1 + 1) = 0. \tag{3.6}$$

This means that neither LHC nor RHC polarized photons carry angular momentum.

Finally, from the eccentricity plot (in the same figure), it can be observed that the overlapping of LHC and RHC polarizations produces a beam that is locally linearly polarized (null eccentricity everywhere). This observation is consistent with the previous observation of the beam being a radially polarized beam.

3.2.2 Spiral gratings

To manipulate the angular momentum of a free space propagating beam, the azimuthal symmetry of a grating can be broken introducing a chirality into the outcoupling mechanism. A spiral shape can be used to introduce a varying phase delay

along different radial directions, as illustrated in Figure 3.6. Making a comparison with Figure 3.3, Bloch Surface waves propagating in opposite directions are phase shifted by $\pi + \Delta\varphi(\theta)$, where $\Delta\varphi$ is the additional phase delay introduced by the spiral shape, while θ is the azimuthal angle.

Depending on the value of $\Delta\varphi(\theta)$, the far field shape can differ significantly, making predictions less intuitive. It is worth noting that a spiral shape is not the only option for introducing a proper $\Delta\varphi(\theta)$, but its simplicity and elegance make it a perfect candidate for the task.

With a single arm spiral grating, the phase delay can be written as

$$\Delta\varphi(\theta) = k_{bsw} \cdot \left(\frac{\theta}{2\pi}\Lambda_g\right) = \theta\frac{\Lambda_g}{\lambda_{bsw}}. \tag{3.7}$$

From the perspective of the radially propagating BSW, the phase delay is introduced prior to the grating, leading to a λ_{bsw} dependence solely on the effective index $n_{eff,h}$, as opposed to Equation (3.2). However, the difference between the effective indices in the aforementioned equation is very small, allowing us to approximate $\Lambda_g \approx \lambda_{bsw}$ and assume

$$\Delta\varphi(\theta) = \theta. \tag{3.8}$$

Likewise to the circular grating, even with a single-arm spiral grating, we can make some intuitive predictions on the behaviour of the far field. For instance, considering BSWs outcoupling from opposite radial directions, we observe that the difference in phase delay between the two is

$$\Delta\varphi(\theta) - \Delta\varphi(\theta + \pi) = \pi.$$

At the center of the far fields, this results in a difference of 2π radians, with the additional π shift due to the BSWs propagating in opposite directions, leading to

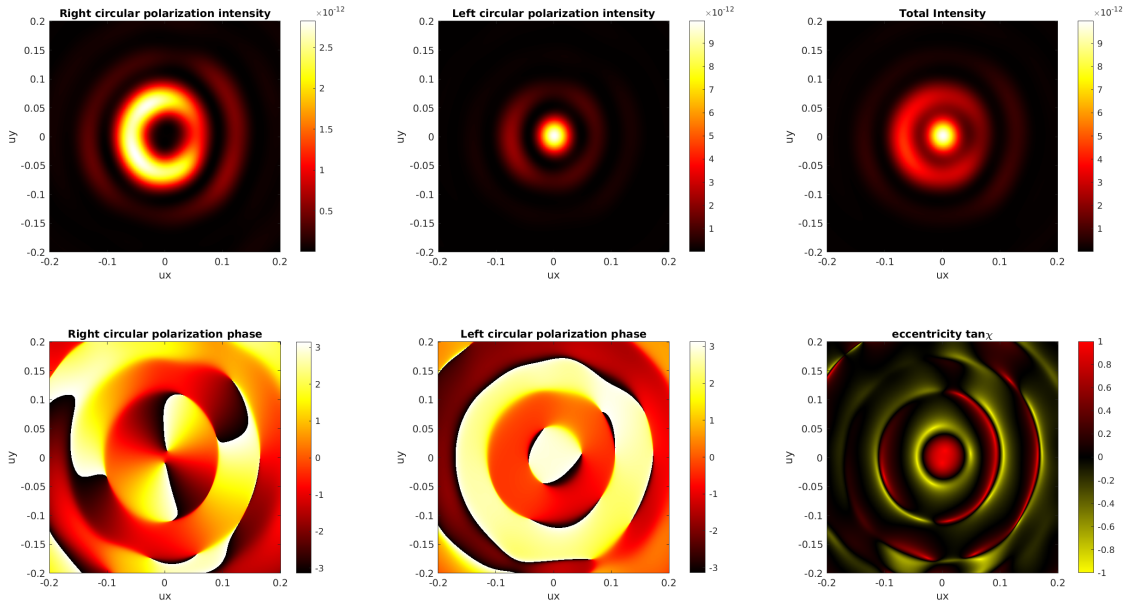

Figure 3.7: Decomposition of the far field for a one-armed, spiral outcoupler. From the phase profile the double helical shape shows an OAM number for RHC polarization $l = -2$. The LHC phase profile is uniform, correspondig to $l = 0$. From the total intensity map and the eccentricity map, it is possible to appreciate the spatial separation between the two polarizations. The grating parameters are the same as per Fig. 3.4.

constructive interference at the center of the generated beam. When considering an orthogonal direction $(\theta + \pi/2)$, the reasoning remains valid, but the resulting far field will be phase shifted from the other direction by $\pi/2$. Given that orthogonal directions correspond to orthogonal polarizations in the far field (for these outcouplers), the polarization will be circular at the center of the outcoupled beam.

Figure 3.7 displays the far-field pattern for a single-arm spiral grating. The beam exhibits a bright, circularly polarized spot at the center, as evidenced by the intensity and eccentricity maps, but it also features an outer ring with the opposite circular polarization.

To better comprehend the grating's impact, it is crucial to analyze the two circular polarizations and investigate their angular momentum. One of the first things to note is that the intensity patterns of the two beams only partially overlap

in space, implying that the two polarizations propagate in two concentric, conic beams. The phase profile of the RHC polarization unmistakably demonstrates the presence of an orbital angular momentum of $l = 2$, whereas the phase of the LHC polarization is uniform, signifying $l = 0$.
Analysing the total angular momentum (J) we get:

$$J = \hbar(\sigma + l), \tag{3.9}$$

$$J_{RHC} = \hbar(+1 - 2) = -\hbar, \tag{3.10}$$

$$J_{LHC} = \hbar(-1 + 0) = -\hbar. \tag{3.11}$$

Once again, it is observed that the total angular momentum of the two polarizations is identical, while their OAM is distinct. However, contrary to the case of circular grating, the difference in OAM results in good spatial separation between the two polarizations.

To better describe the increase in angular momentum, it is helpful to associate a topological charge (m) to the spiral grating. This allows us to express the total angular momentum as

$$J = \hbar(\sigma + l) = \hbar m, \tag{3.12}$$

assigning a topological charge of a single arm spiral a value of $m = \pm 1$. The results presented for a anti-clockwise spiral suggest to associate a positive m if the spiral is clockwise.

Increasing the topological charge

Equation (3.12) can be applied to a circular grating as well, considering its topological charge $m = 0$, since it is an achiral structure. Thus, it is reasonable to associate the topological charge with the number of arms of the spiral. For a

general spiral grating, the relation in Eq. (3.8) would be modified as follows:

$$\Delta\varphi(\theta) = mod_{2\pi}(m\theta), \tag{3.13}$$

and from Eq. (3.12) one can easily predict the OAM number of a general spiral grating in the form

$$l = m - \sigma. \tag{3.14}$$

The validity of the relation described in the previous paragraph was confirmed through experimental testing of spirals with higher values of topological charge. Figures 3.8 present the results for a two-armed spiral and a three-armed spiral, respectively. The intensity profiles clearly demonstrate that the RHC and LHC polarizations propagate in concentric, doughnut-shaped, conic beams, which are typical of vortex beams. The two polarizations again are (partially) spatially separated, with the phase profiles allowing for the determination of the OAM number l and confirming the validity of Eq. (3.12).

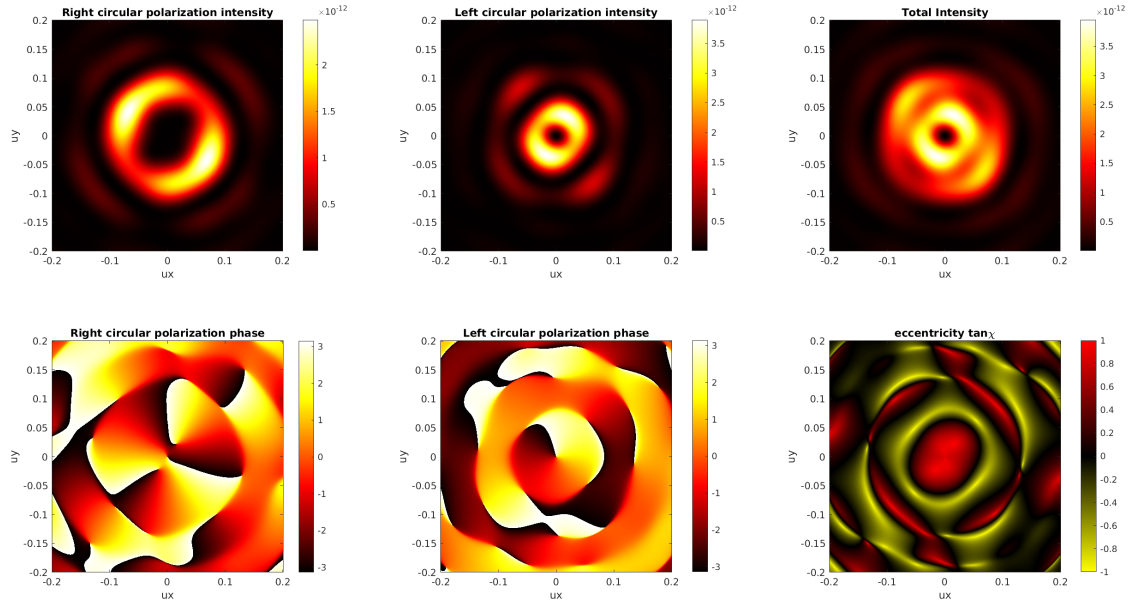

(a)

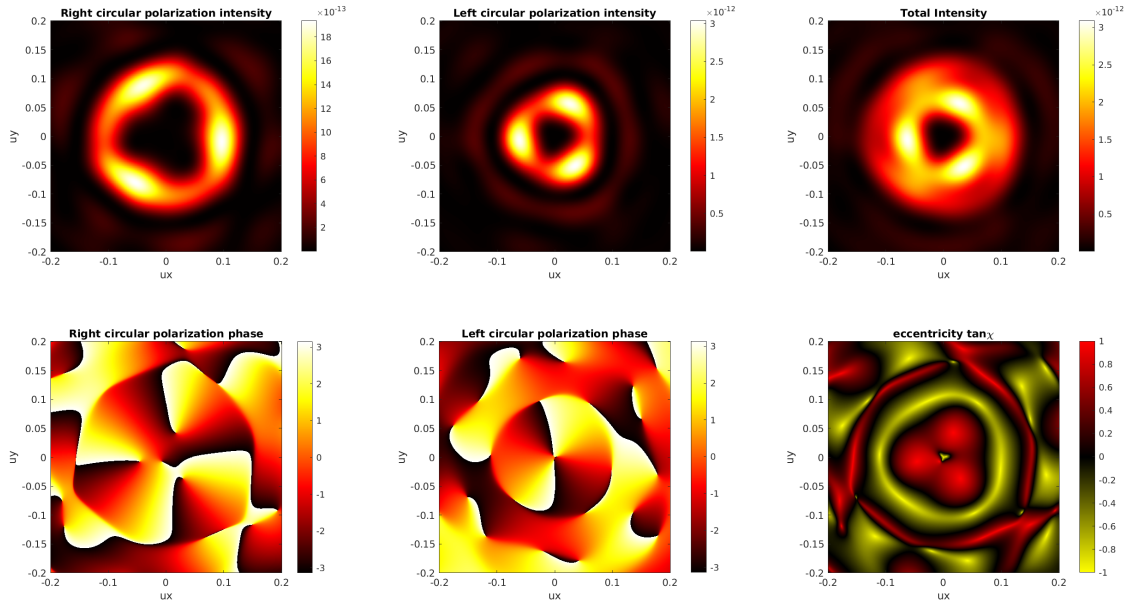

(b)

Figure 3.8: Decomposition of the far field for a two-armed $m = -2$ (a) and three armed $m = -3$ (b) spiral outcoupler, anticlockwise oriented . In (a) the phase profile shows an OAM number for RHC polarization $l = -3$ and for LHC $l = -1$. In (b) the phase profile shows an OAM number for RHC polarization $l = -4$ and for LHC $l = -2$. For both polarizations the sum of spin number with the OAM number equals to the topological charge, in accordance to eq. (3.12). The other grating parameters are the same as per Fig. 3.4.

3.3 Vortex beams with arbitrary spin and OAM

Controlling the phase delay between the grating and the source enabled the manipulation of the angular momentum properties of the generated light beam. However, simulations have indicated that both left and right circular polarizations are affected simultaneously, with a certain degree of spatial separation. Although it might be possible to choose one polarization over the other using physical filters or mirrors, it is not feasible to manipulate only one polarization or exclude the other. To generate a beam with arbitrary OAM and spin, alternative scatterers, particularly metasurfaces, have been investigated.

3.3.1 Anomalous diffraction from phase discontinuities

Metasurfaces are two-dimensional arrays of subwavelength structures that can manipulate light properties, such as polarization, phase, and amplitude [103]. Due to their versatility, they have various applications ranging from planar optics [104] to vortex beam generation [46, 105]. Typically, metasurfaces are used as transmissive optical elements, however, with the appropriate design, they can act as gratings and be combined with surface propagating modes like Bloch surface waves or surface Plasmon polaritons.

In the quest to suppress one of the two polarizations' scattering, we explored phase discontinuity induced chiral sensitive gratings. These gratings are a type of metasurface that is able to diffract different circular polarizations in different directions. Originally introduced in [106], they consist of metallic nanoparticles aligned in lines and oriented in various directions, as depicted in Figure 3.9. The particular arrangement of the nanoparticles causes the light to scatter at the conventional Bragg diffraction angles, determined by the distance between the lines, and at additional diffraction angles, known as extraordinary (or anomalous) diffraction angles, depending on the polarization.

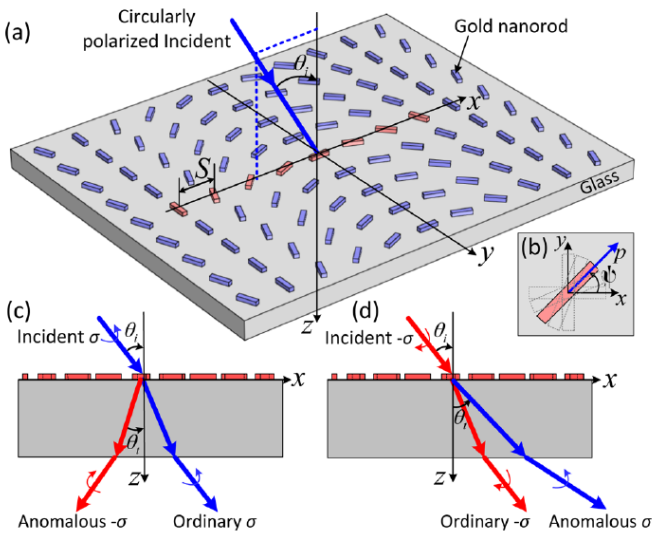

Figure 3.9: Depiction of a typical chiral sensitive metasurface grating. Image taken from [106].

As explained in [106], the extraordinary diffraction mechanism is caused by plasmonic resonances on the nanoscatters, which act as nanoantennas. As from the figure, the scatter are oriented with a gradient of orientation, which introduces a phase delay between the nanoantennas oscillations for different lines, and introduces a phase discontinuity in the diffracted beam. To account for anomalous diffraction, for low incidence angles, the grating wavevector can be corrected in the following way [107]:

$$K_g = m\frac{2\pi}{\Lambda_g} + \sigma\frac{2\Delta\psi}{\Lambda_g}, \tag{3.15}$$

where m is the diffraction order, ψ is the angle difference between two consecutive nanoscatters and σ is the spin number of the polarization (see sec. 3.2.1 for the used convention).

3.3.2 Metasurface enabled vortex beams from single dipole source

Similar to the approach of Section 3.2.1, if we assume Equation (3.15) to be valid for high impinging angles, it can be used to design a metasurface that outcouples the Bloch surface wave into free space. To achieve normal diffraction, we equate the BSW wavevector with the grating wavevector at the first diffraction order. This allows to determine the grating main period:

$$\begin{aligned} k_d &= k_{bsw} - K_{g,\sigma}^{(1)} = 0, \\ k_{bsw} &= K_{g,\sigma}^{(1)} = +\frac{2\pi}{\Lambda_g} + \sigma\frac{2\Delta\psi}{\Lambda_g} = \\ \Lambda_g &= \frac{2\pi(1+\sigma\Delta\psi/\pi)}{k_{bsw}}. \end{aligned}$$

Here k_{bsw} can be computed from Eq. (3.2) by approximating the fill factor as the ratio between the width of the nanoscatter over the period of the grating ($FF \approx w/\Lambda_g$).

It is important to note that once the grating's period is determined to scatter one polarization normally with respect to the surface, the other polarization will scatter at a different angle. Additionally, a residual part of the BSW is still diffracted at the standard Bragg angle, though maintaining linear polarization. For example, if LHC polarized light is designed to scatter normally ($k_{d,-1} = 0$), the RHC and linear polarizations will scatter in the following directions:

$$k_{d,+1} = k_{bsw} - \frac{1+\Delta\psi/\pi}{1-\Delta\psi/\pi}k_{bsw} = -\frac{2\Delta\psi/\pi}{1-\Delta\psi/\pi}k_{bsw}, \tag{3.16}$$

$$k_{d,0} = k_{bsw} - \frac{1}{1-\Delta\psi/\pi}k_{bsw} = \frac{-\Delta\psi/\pi}{1-\Delta\psi/\pi}k_{bsw}, \tag{3.17}$$

where $k_{d,\sigma}$ is the component of the wavevector parallel to the surface for the

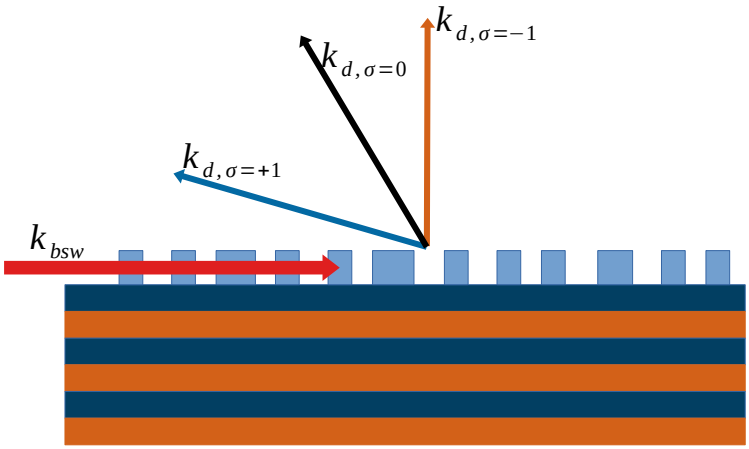

Figure 3.10: Orientation of the ordinary and extraordinary (blue and orange arrows) diffraction orders with respect to the ordinary (black arrow) diffraction order for an exemplary grating designed to diffract a BSW. Diffraction is designed to be normal for the LHC component of the beam.

diffracted light, with $\sigma = 0$ referring to the standard Bragg diffraction. An illustration of diffraction orders is shown in Figure 3.10.

$\Delta\psi$ should be chosen to maximise the separation between the two polarization diffraction orders, while maintaining the chirality of the structure. For instance, $\Delta\psi = \pm\pi/2$ is not a viable option because it breaks the chirality. More precisely, Eq. (3.15) looses validity for greater values of $\Delta\psi$, since it is determined from an ideal case where the phase delay induced by the scatter orientation changes continuously along the grating direction[106, 107] (which is not realistic with these nanoscatters). Interestingly enough, by choosing $\Delta\psi = -\pi/3$ one obtains $k_{d,0} = -k_{bsw}/2$ and

$$k_{d,-1} = -k_{bsw},$$

which describes the reflection of the BSW towards the source. It should be noted that a TM BSW cannot have circular polarization, therefore $k_{d,-1}$ is likely either a non-viable channel of diffraction or it is attenuated. Designing instead for RHC polarization one can rewrite the equations, finding that the "best" choice for the scatter angles is $\Delta\psi = +\pi/3$.

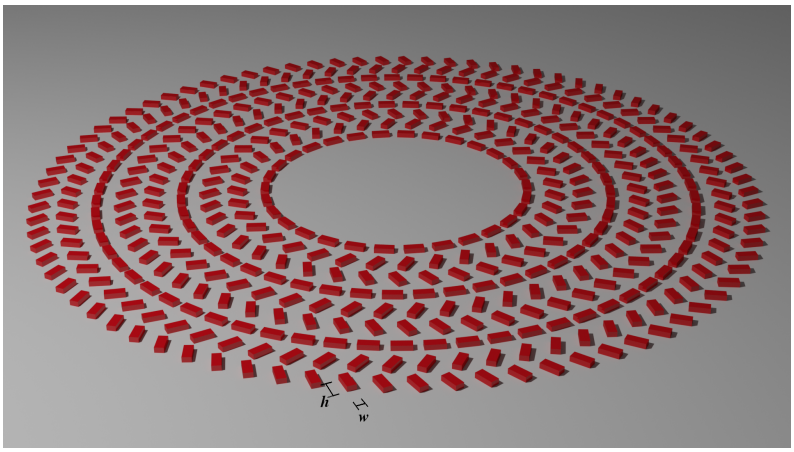

Figure 3.11: Rendering of a circular metasurface grating outcoupler. The design parameters are $\Lambda_g = 220$nm, scatter width $w = 0.3\Lambda_g$, scatter height $h = 0.8\Lambda_g$, $\Delta\psi = -\pi/3$, for $N = 12$ periods.

When transitioning to a circular geometry, arranging the nanoscatters becomes somewhat more complex, as there are multiple options to consider. Ideally, the azimuthal distance between the scatters should not affect the radial propagation of the BSW. Hence, one option is to maintain the radial alignment of the scatters while increasing the azimuthal distance for the outer rings of the grating. However, testing various configurations revealed that tightly packed scatters result in higher diffraction efficiency, even if radial alignment is lost. The proposed design is illustrated in Figure 3.11.

To analyse the behaviour of this grating, we must examine the far-field maps. The residual intensity in the polarization could be attributed to imperfections introduced in the metasurface when adapting it to a circular geometry.

Manipulating the topological charge.

At this juncture, it is feasible to reintroduce the topological charge by implementing an angle-dependent radial phase delay between the source and the grating, as proposed in Section 3.2.2. However, the spiral arrangement becomes impractical since the period of the grating is considerably different from the spatial period of

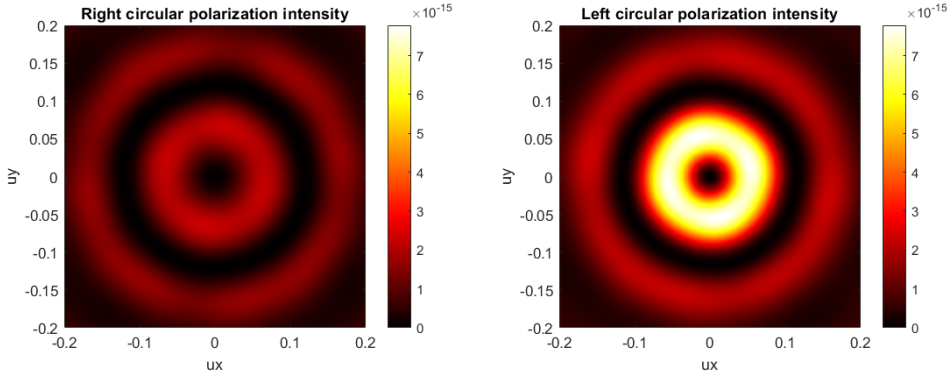

Figure 3.12: Far field intensity maps of the two circular polarizations for a circular metasurface outcoupler with the parameters of Figure 3.11. The attenuation of the LHC polarization is evident, with an overall reduction in intensity of $\approx \frac{1}{3}$ the one of the other polarization.

the Bloch surface wave. Consequently, Equation (3.7) cannot be employed to define the topological charge as in Equation (3.13). Nonetheless, if we consider the latter equation to be a necessary condition to leverage the topological charge to modify the orbital angular momentum, we can establish a phase delay that complies with that precise formula. In other words, we must modulate the distance between the first set of scatters and the source as follows:

$$r = r_0 + \frac{mod_{2\pi}(m\theta)}{2\pi}\lambda_{bsw}, \tag{3.18}$$

where r_0 is an offset from the source, and $\lambda_{bsw} = n_{eff,h} \cdot \lambda_0$. Each subsequent set of scatters will be positioned at a radial distance Λ_g from the previous set.

It is noteworthy that Equation (3.18) can be generally applicable even for continuous gratings. Specifically, for the case when $\lambda_{bsw} \approx \Lambda_g$, as assumed in Equation (3.8), the relation describes a generic Archimedean spiral with a period of Λ_g.

In Figures 3.13, we observe the proposed metasurfaces and the intensity of the far fields. The intensity and phase profiles suggest the presence of vortex beams similar to the previous section, except that one of the two polarizations is now

partially suppressed.

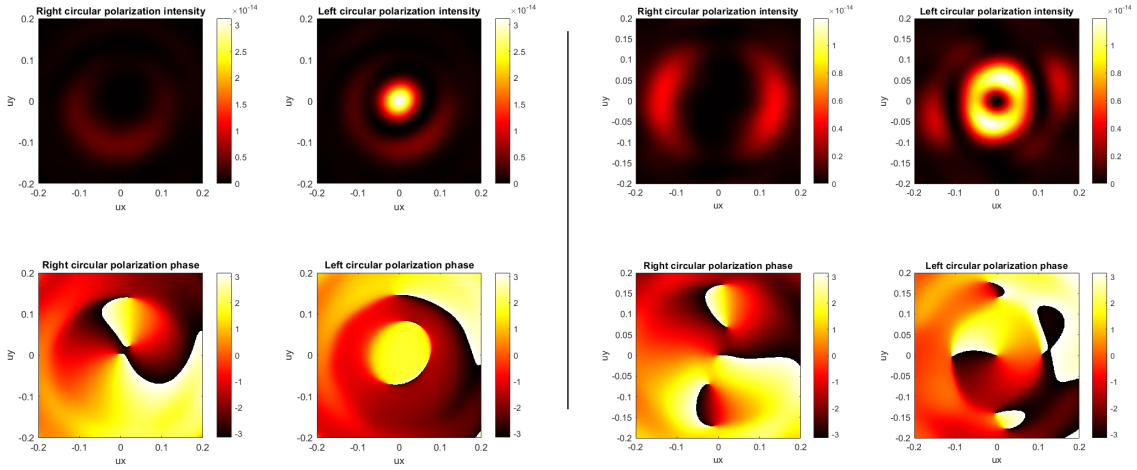

(a) (b)

Figure 3.13: Far field intensity and phase maps of the two circular polarizations for a circular metasurface outcoupler, with the parameters of Figure 3.11 and topological charge $m = -1$ (a) and $m = -2$ (b). The phase maps highlight $l = 0$ (a) and $l = -1$ (a) for the LHC polarization, in agreement with Eq. (3.12).

The complete design

For the sake of completeness, also the complete device, consisting of the circular cavity and metasurface outcoupler was simulated. The simulations are by all means identical, with the only difference being the absence of the beam blocker. The results of these simulations were practically identical to the one already presented, therefore they are not included to avoid redundancy.

Regarding the design of the circular DBR cavity, more information can be found in the following section and in Chapter 2.

3.4 Design of TM Bloch Surfaces waves

The exact values for the Bloch surface wave design were intentionally omitted in all presented results, as they require a dedicated section to explain. The device

was designed to operate in the visible range of the spectrum with real single photon emitters, and therefore the multilayer hosting the BSW was custom-designed. The emitters intended for the task emit at a wavelength of approximately 570nm, therefore such is the wavelength around which the device was designed. Originally the available materials were Silica (SiO_2), Titania (Ti_O2) and Allumina (Al_2O_3). In particular Allumina is used as an etch stop for carving patterns into Silica, therefore one design constrain was to keep an Al_2O_3 layer below the Silica layer hosting the gratings.

The codes used for finding an optimal multilayer design were written in MATLAB and can be found in the git repository [108], where a self implemented version[30] of the transfer matrix method (TMM) is used.

3.4.1 Fabrication constrains

Fabricating a dielectric multilayer stack can be very challenging. Amorphous dielectrics can be very brittle and fragile and the mismatch in the atomic properties of each layer can result in strong stress that can lead to cracks and exfoliation. For these reasons, the number of deposited layers should be reduced as much as possible even though generally a larger number of layer is better for the quality of the hosted BSW. Specifically it was suggested not to exceed twenty alternating dielectric layers.

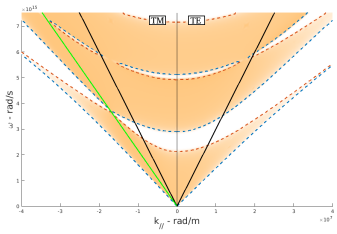

Figure 3.14: Extracted from Fig. 1.5.

An additional problem that comes along with TM modes (and is absent in TE modes), is the presence of the so called Brewster points that close the band gap beyond the vacuum light line, as better shown in Figure 3.14. For a given photonic crystal the Brewster points are located on a line defined by:

$$\omega = c_0 \cdot \beta / (n_1 n_2 / \sqrt{n_1^2 + n_2^2}), \tag{3.19}$$

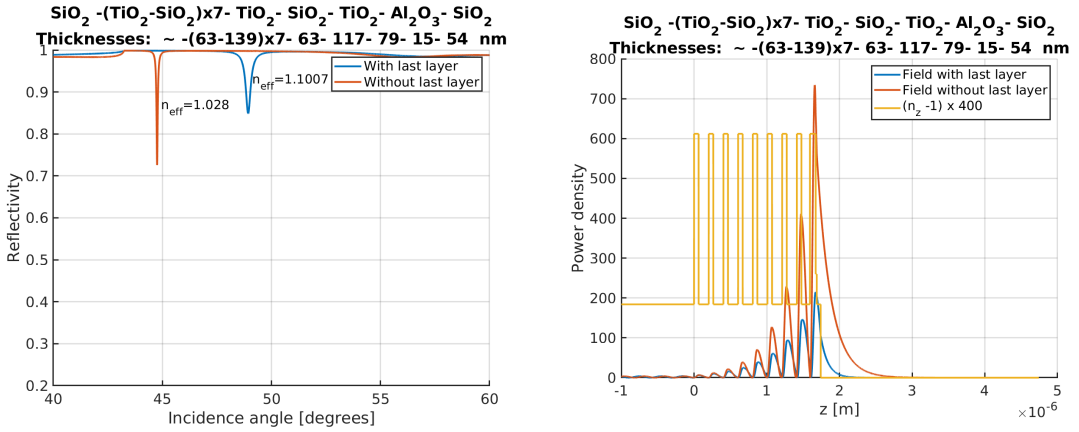

(a) (b)

Figure 3.15: a) Reflectivity of the multilayer at λ =570 nm. (b) Field enhancement distribution for the two BSW lines in figure (a), in terms of magnetic field H. Design description on top.

where β is the transverse wave-vector and n_1, n_2 are the refractive indices of the two material composing the multilayer. This line is referred as Brewster line.

Being bound inside the band gap, the dispersion of the BSW will fade away once it approaches the Brewster points. Remembering that, contrary to an ideal semi-infinite 1DPC, dielectric multilayers do not possess sharp band gap edges, it is evident the presence of the Brewster points reduce drastically the quality of a Bloch surface wave. These effects become more and more evident the smaller is the number of layers used in the multilayer stack.

With a constrain of 20 deposited layers, the best TM design obtained is presented in Figure 3.15. From the reflectance plot it is possible to observe the poor quality of the mode. A 3D simulation with a circular cavity designed to resonate at $\approx 570nm$ is used to test the quality of the multilayer design. A good quality BSW, with a circular cavity with $N > 30$ periods in the distributed Bragg reflector typically resonates with a quality factor $Q > 1000$. The results of Figure 3.16 show a quality much smaller than that one, which would be less then ideal for the final

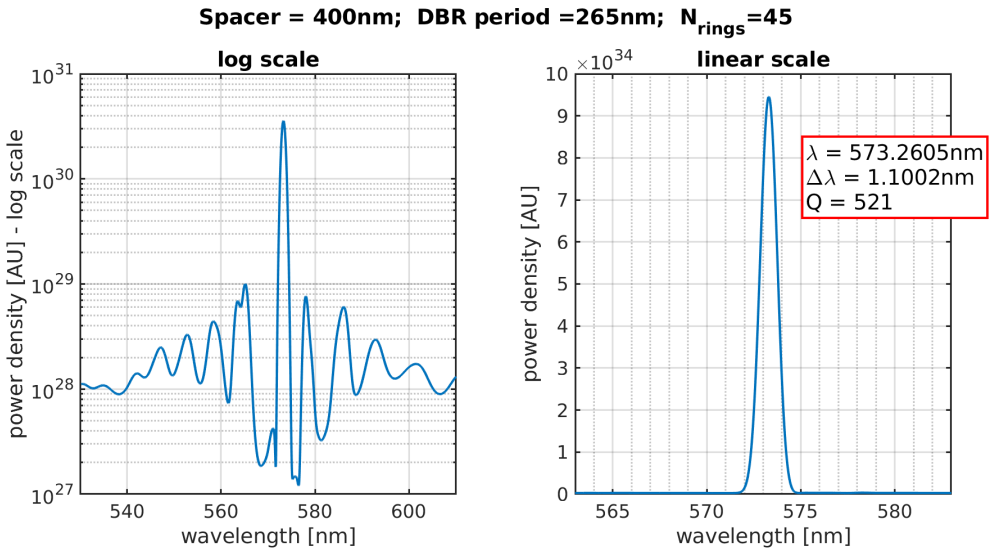

Figure 3.16: Results from a 3D simulation for the multilayer in figure 3.15 with a circular cavity carved into the last layer. Parameters of the cavity are on top of the figure.

device.

3.4.2 Buried structure

One possible solution for the Brewster line problem could be to increase the contrast between the refractive indices in Equation (3.19). This would push the line deeper beyond the vacuum light line, reducing its effect on the band gap in the region of interest. This option is very difficult to pursue, because finding high refractive index materials that are compatible with multimaterial deposition systems is very difficult.

Another interestingly different approach could be to search for the BSW even beyond the Brewster line. Unfortunately the farther from the light line the mode is located, the deeper the field gets confined into the multilayer, increasingly loosing the sensiticity and connection with the surface. Nonetheless it should still be possible to try to optimize the modes so that they are confined closer to the surface and exploit them with the classical surface patterns. Even if these modes may

be originating from the same conditions that produce Bloch surface waves, since they are located beyond the Brewster line, their dispersion cannot be continuously associated to the one of a BSW which dispersion would begin at the light line. For this reason instead of referring to them as BSW, from now on they will be referred as pseudo-surface modes.

In practical terms, these pseudo-surface modes are actually located after the substrate light line. For a single emitter coupling on the surface this is not actually a problem, because it will be able to inject energy in the mode as long as there is sufficiently high Local Density Of States (LDOS). For the computation instead, this fact requires some tricks in the TMM computation. In particular, in order to increase wavevector range of the band diagram, it is necessary to change the refractive index value of the substrate with a fake, higher, value. This allows to probe the multilayer with higher wavevector waves and search for modes even beyond the original substrate light line. For this reason, the dispersion relation of the following designs is computed assuming a substrate with refractive index equal to 2, while in the 3D Lumerical simulation such substrate is reverted back to be made of Silica.

Although they can be exploited in a similar manner for interacting with the structures already mentioned, these pseudo-surfaces mode have some big differences that forces a slight change in approach:

- Since the mode is confined inside the layers the exponential tail present in the air is not sufficient to allow efficient coupling with the source.
- For the same reason, the mode can become less sensitive to a dielectric loading aiming at shifting the effective refractive index of the mode.
- Since the mode is located far from the air line, the effective refractive index is relatively high, which implies much lower spatial frequency; this result in features of the planar structures that can surpass the limits of the lithographic

techniques that would be used when creating such structures.

- High effective refractive index modes are more sensitive to layer thickness fluctuations.

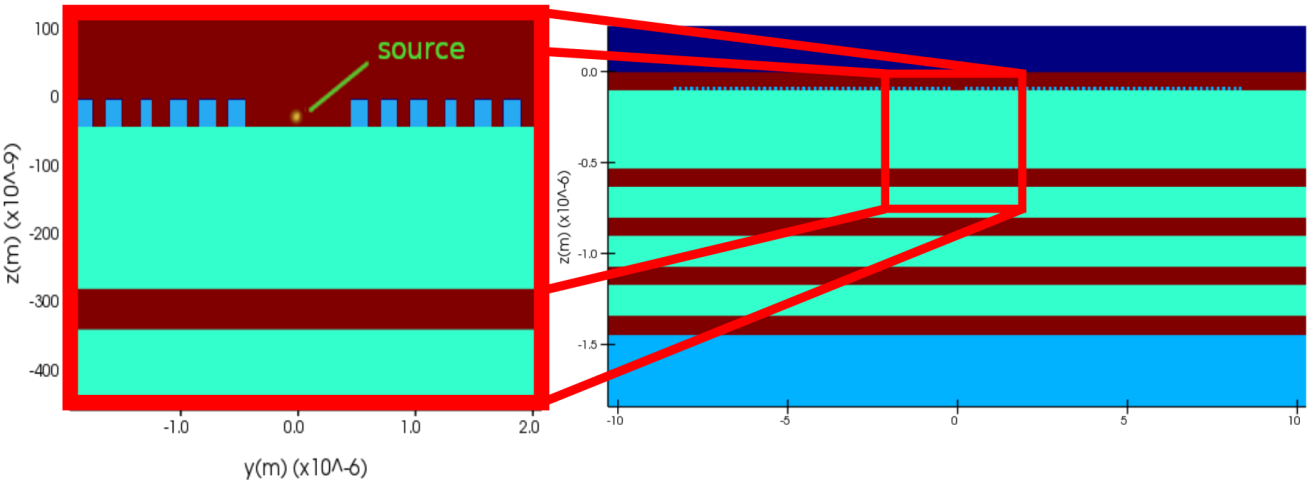

Figure 3.17: Section of the multilayer stack with the structure buried under the last layer.

The first point can be solved by placing the dipole source inside the multilayer, at the interface between the last and the second last layers. The multilayer is thus designed in order to have the maximum of the mode field close to such interface. The second point instead can be solved by shifting the planar structures (circular cavity and spiral) at the same interface in which the dipole is placed. In this way the structures will result to be buried below the last layer.

First design for buried structures

The multilayer structure designed following these guidelines is shown in Figure 3.18. The result from the 3D simulation 3.19 show high resonance quality and it is a very good candidate for the purpose of this study. All the simulations performed in sections 3.2 and 3.3 were using this specific design.

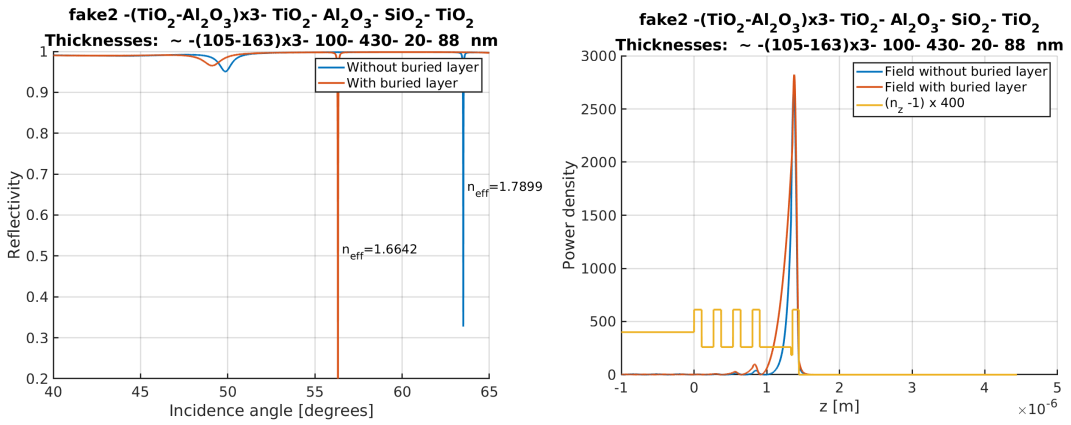

(a) (b)

Figure 3.18: (a) Reflectivity of the multilayer at λ =570 nm. (b) Field enhancement distribution for the two BSW lines in figure (a), in terms of magnetic field H. Design description on top.

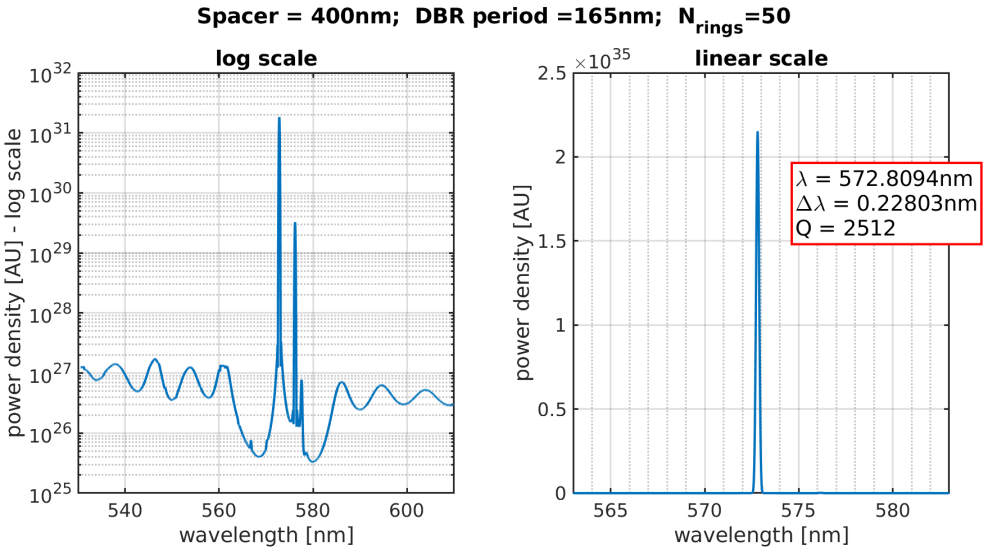

Figure 3.19: Results from a 3D simulation for the multilayer in figure 3.18 with a circular cavity carved into the second last layer. Parameters of the cavity are on top of the figure.

In figure 3.20 the entire dispersion diagram of the proposed multilayer is reported. The dispersion is represented as the reverse of the reflectivity map (i.e. $1 - R$) for better contrast visualisation.

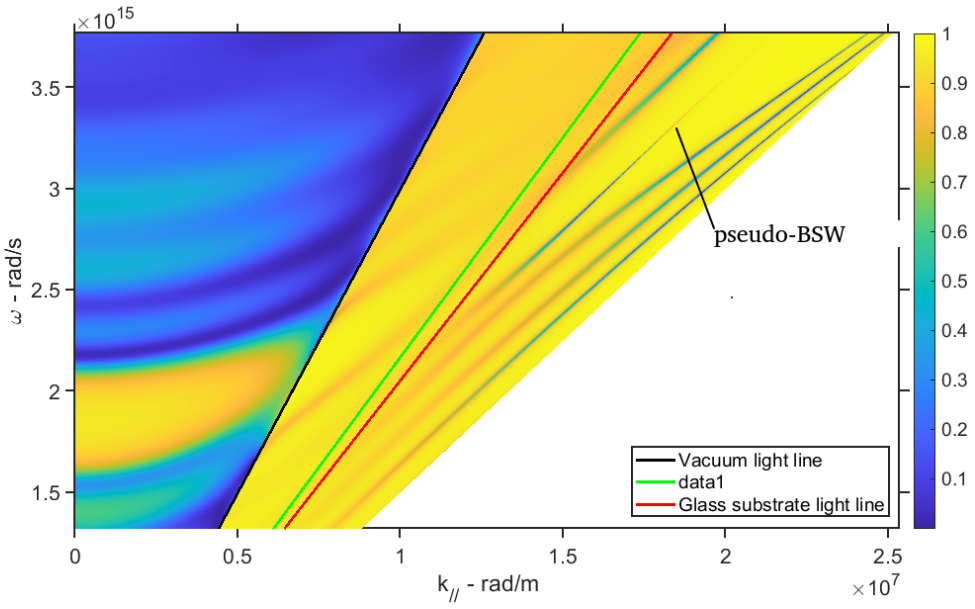

Figure 3.20: Dispersion diagram for the design in figure 3.18. The black, green and red lines represent the air light line, the Brewster line and the substrate light line respectively. The mode dispersion is locate beyond the substrate light line.

Second design for buried structures

Even though the previous design is of good quality and performed well with the metasurface grating outcouplers, its geometrical features will require high resolution lithographic techniques. The size of the scatter would be something like 60nm by 150nm, which trivial for last generation systems, but can be challenging in many less ideal systems. The reason of their small size comes from the high effective refractive index of the pseudo-surface modes involved.

Here a second design is proposed in which Alumina was substituted with Silica, in the attempt of reducing the effective index.

In figure 3.22 we also report the result from the 3D simulation. The quality of the resonance is lower, but still greater than 1000.

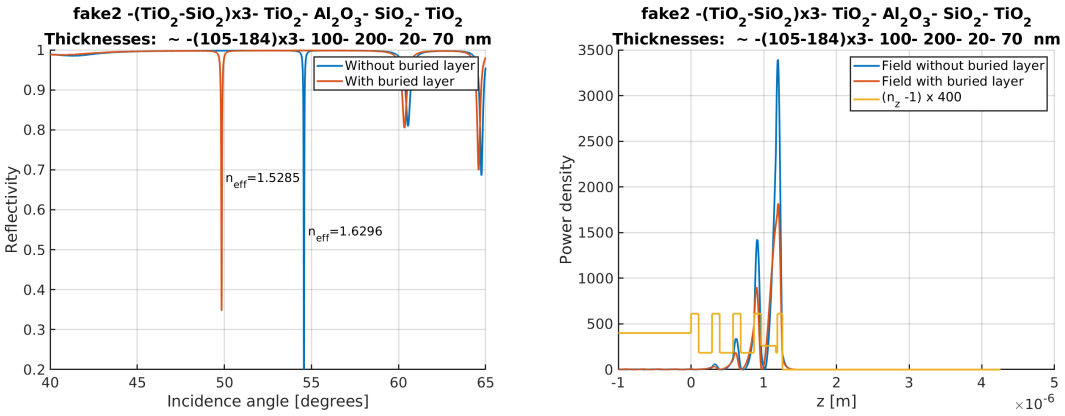

(a) (b)

Figure 3.21: (a) Reflectivity of the multilayer at λ =570 nm. (b) Field enhancement distribution for the two BSW lines in figure (a), in terms of magnetic field H. Design description on top.

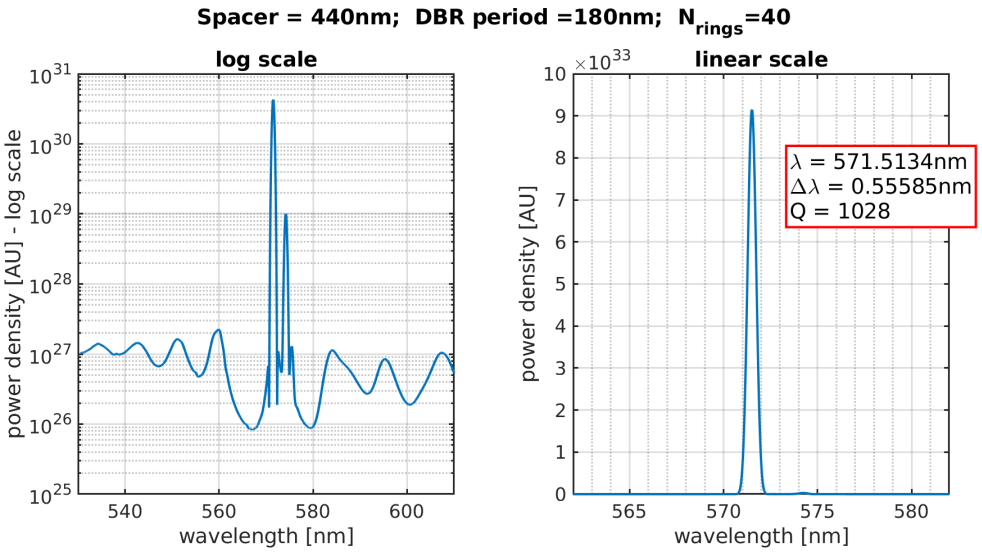

Figure 3.22: Results from a 3D simulation for the multilayer in figure 3.21 with a circular cavity carved into the second last layer. Parameters of the cavity are on top of the figure.

Chapter 4

Single photon emission from 2D materials

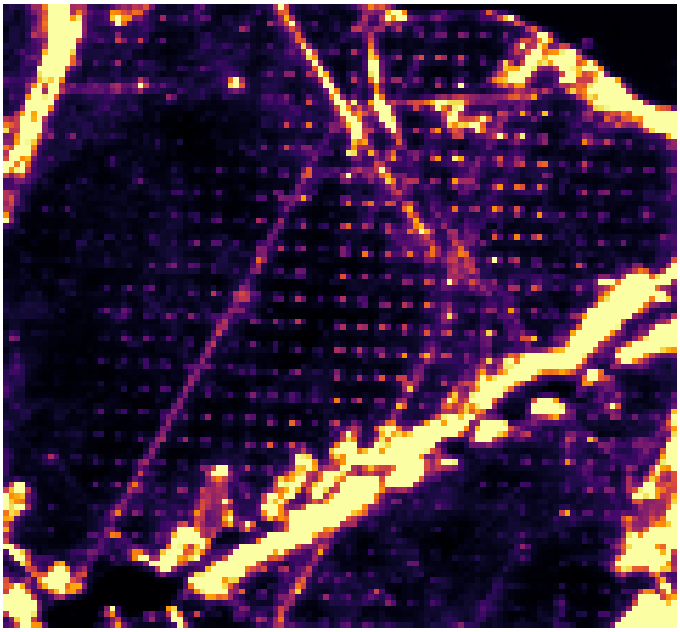

Figure 4.1: Exemplary confocal map of an h-BN flake damaged with a focused ion beam using a dot-matrix array exposure pattern.

With the continuous development of quantum technologies, there is an increasing demand for reliable and easy-to-integrate single-photon emitters (SPEs),

which has led to the exploration of new and sophisticated methods for controlling their generation [109]. While solid state quantum dots [110–112] and Nitrogen vacancies in diamond crystals[113–116] are the most popular types of quantum emitters, other sources such as single molecule emitters[117], cold atoms [118], carbon nanotubes [119, 120] and, more recently, defects in two-dimensional (2D) crystals[121, 122] have also proven successful. In recent years, 2D crystals, particularly Transition Metal Dichalcogenides (TMDs), have gained significant attention due to their ease of fabrication and versatility. TMDs are a type of semiconducting material that exhibit excitonic resonances when fabricated as mono-layers[123–125]. Although it is possible to generate SPEs in TMDs through simple strain[13–15, 126, 127], they require extremely low temperatures (4K) to operate, which can be impractical for certain applications and mass adoption. As an alternative, Hexagonal Boron Nitride (h-BN), another 2D material, has been shown to provide SPEs at room temperature, making it a promising candidate for use inside the metasurface vortex generators presented in the previous chapter.

In this chapter, a study of room-temperature SPE generation in h-BN is presented. The emitters were induced by localized damage using focused ion beam (FIB), followed by thermal annealing, then studied by means of fluorescence and confocal imaging. This study was performed in collaboration with the National Research Council in Lecce (CNR Nanotech) and the National Institute of Metrology (IRIM).

4.1 Hexagonal Boron Nitride for emission sources

Hexagonal Boron Nitride is a compound composed of boron and nitrogen atoms arranged in a hexagonal lattice structure, similar to graphene. Being a wide band gap crystal, it is a good material for electronics and photonics thanks to its high thermal and electrical insulation properties. It is often synthesized by means

of chemical vapor deposition (CVD) [128, 129] or high-pressure high-temperature (HPHT) synthesis [130, 131]. Other techniques are also available, such as low pressure CVD on Germanium [132], hydrothermal synthesis[133] and many others [134]. While h-BN grown by CVD can be fabricated directly on the device of interest, the h-BN produced with HPHT synthesis requires additional steps for the material transfer, but it produces the highest quality crystals.

In the last decade, h-BN has been increasingly explored for the generation of quantum emitters. The origin of these emitters is strongly under debate but is typically associated with defects in the crystal, specifically nitrogen vacancies[20] or interstitial implantation of other species such as Carbon[17]. These defects can introduce localized defect states inside the bandgap, trapping charge carriers and leading to the emission of photons upon recombination. Therefore, to controllably generate quantum emitters, it is necessary to control the creation of defects, or at least their activation, inside the crystal. To achieve this goal, many different methods have been proposed, such as strain from pillar matrices[135], CVD growth on nanopillars[16], localized FIB damaging[136], localized AFM damaging[137], electron beam irradiation[18], and ion irradiation[17, 138, 139]. Unlike TMDs, where the activation of the emitters seems to be bound to the presence of an excitonic state, emitters can be found in hBN of all thicknesses, reducing the stringent requirement of using one or a few layers of material. For the same reason, these emitters in hBN tend to be able to operate in the quantum regime also at room temperature.

With the goal of creating sources to be used in combination with Block surface waves, we attempted to replicate some of the results proposed in literature. Our approach focused on localized FIB damaging, which provides a rather simple method for inducing defects directly at the site where the final emitter is supposed to be located. This is often a critical issue when dealing with other types of quantum emitter providers like quantum dots. We used HPHT synthesized h-BN, processing it in the following way:

- peel h-BN in the form of thin flakes of various thicknesses;
- transfer the proper flake onto a substrate made of silicon or silicon dioxide;
- expose multiple flakes with a dot-matrix pattern using different doses;
- thermally anneal the sample at 850°C to activate the defects.

The flakes were characterized using optical and fluorescence imaging after each step to monitor their effects on the flake.

4.2 FIB induced defects

In a work by Ziegler et al. [136], it was shown that a focused ion beam could be used to carve holes into h-BN flakes in order to induce defect states by means of edge formation. Following this idea, we explored the possibility of using a focused ion beam, working with a standard Gallium source, in order perform as minimal damage as possible to the flake, in the attempt of inducing a single defect state allowing for single photon emission (SPE). More recently similar ideas were proposed in [139] and in [140], although in the former they perform unlocalized exposure, loosing control on the emitters location, and in the latter quantum emission is not archived. Here h-BN flakes of different thicknesses were placed on a Silicon substrate and they were exposed with a dot-matrix pattern array, using different doses, as shown in Figure 4.2. The exposure was performed on a Raith lithographic machine, designed for electron and ion beam lithography. The exposure settings were adjusted in such a way to perform a single exposure for every dot of the matrix, so to avoid proximity effects, while varying the dwell time to test different doses. In particular, each column of the matrix is set to a different dose value and, considering that each time ten doses are tested, these values are periodically repeated every ten columns.

In Figure 4.3 a scanning electron microscope (SEM) image of a flake before and after FIB exposure is shown. The exposed pattern appears as dark spots, darker

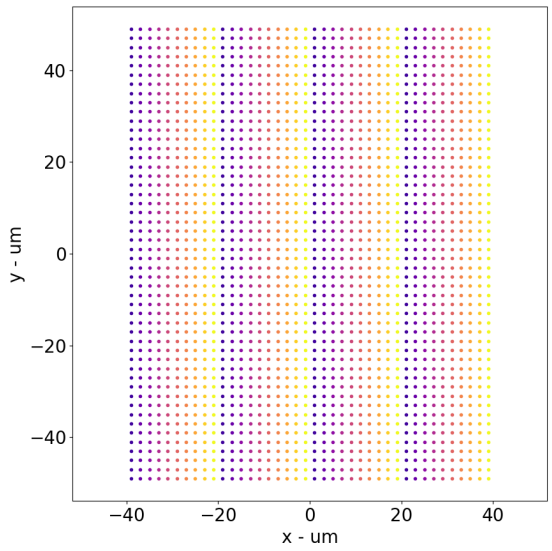

Figure 4.2: Dot-matrix exposure pattern. Each color represent a different exposure dose. The dots are made in the form of circles with a 30nm diameter, and the scan point-to-point distance is set to 100nm, is such a way to include only one exposure point per circle. The circles are 2.5μm distanced apart in both directions.

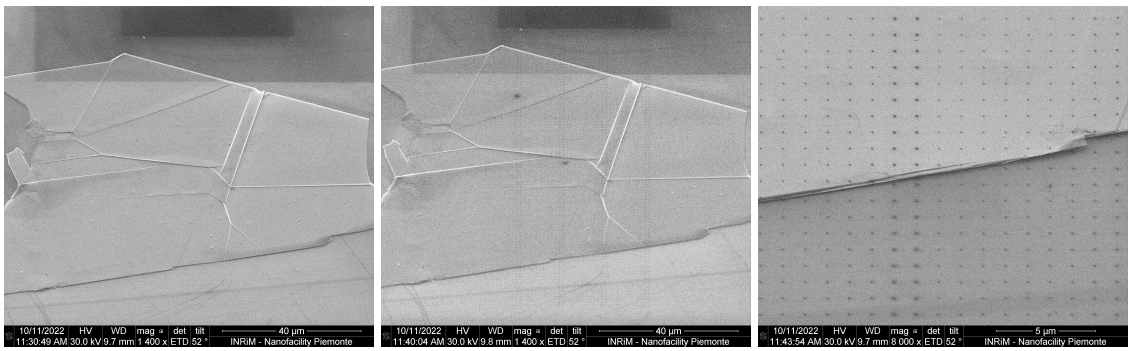

(a) (b) (c)

Figure 4.3: SEM images of an h-BN flake of approximately 150nm thickness (a) before and (b) after the exposure of the pattern in Fig. 4.2. (c) shows a zoom in on the exposed pattern.

where the dose is higher. Later scanning probe microscopy (SPM) analysis revealed these spots to not be holes in the flake (except for the higher dose ones), which suggests to associate the change of colour in the SEM images to a deposition of carbon residuals at the exposed site. These residuals form when contaminants inside the microscope vacuum chamber interact with charged parts of the sample [141–143].

In facts, h-BN is a highly electrically insulating material and a charging effect can occur even with conducting substrates. Unfortunately these carbon residues, even if extremely thin, tend to fluoresce in the same region of the spectrum as the defect states, creating a background disturbance.

After the exposure, the samples are thermally annealed at 850°C in normal atmosphere for 1h, with a 1h ramp up a 3h ramp down. According to multiple sources [16, 17, 20, 136–138], this (relatively) high temperature annealing is necessary in order to activate the defect states and allow for emission in the quantum regime. In practice, spectral analysis prior to this step showed that emission from the damaged site is either absent, or hidden by the background fluorescence caused by carbon residuals. Instead, after the annealing background emission is greatly reduced and fluorescence from the damaged sites becomes more evident. Lower temperature annealing ($300 \div 650$°C) was tested, but it did not reveal formation of good quality emitters, even if the background was removed.

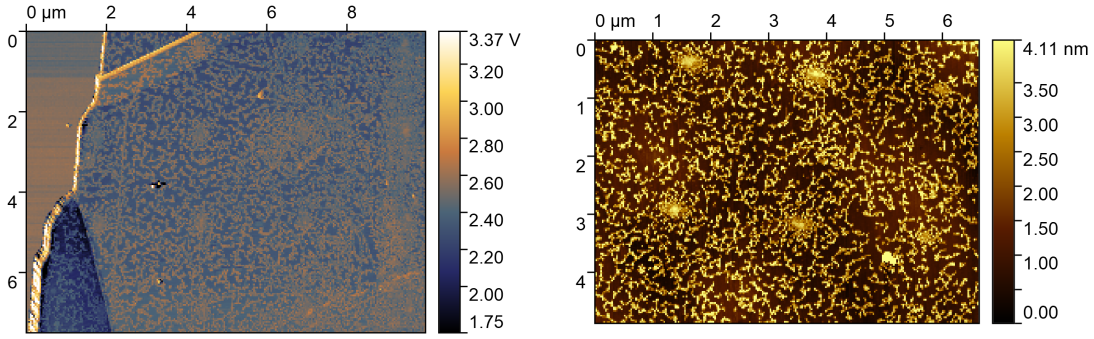

(a) (b)

Figure 4.4: SPM images of an h-BN flake of approximately 100nm thickness after the exposure of the pattern in Fig. 4.2. (a) show the phase map of the flake, allowing to better appreciate the roughness of the surface and the presence of the damaged sites. In (b) the surface thickness maps is shown on a zoomed region.

SPM imaging reveals the nature of the damage. In Figure 4.4 it is possible to

observe a 100nm thick flake, in a region where the spectra presented in the following section where measured. In accordance with what proposed in [140], the damaging of the flake is not sufficient to ablate away the material, but it is enough to brake some crystal bonds and create a small bump on the surface. The height of this bump remains of the order of the surface roughness.

The dose used for the FIB damaging is determined by the acceleration voltage (AV) of the ion gun and by the exposure (dwell) time. Using the highest possible AV is necessary to obtain a better resolution on the beam with a narrower focus spot, but also leads to higher minimal dose. As it will be better shown in the next sections, with an $AV = 30$keV the minimum allowed dwell time ($.2\mu$s) seems to be too high to generate isolated defect states and obtain single photon emission. Although it is still possible to create emission centers with determined spectral characteristics. Unfortunately, due to the very low yield of formation of good quality emitters, it was not possible to associate an optimal dose to the generation of SPEs. Nonetheless emitters were obtained by using $AV = 20$keV, with a dwell time ranging from (100μs and 300μs).

4.2.1 Room temperature spectral measurement

Single photon emitters are typically characterized by a narrow emission spectrum, since the electronic transition typically happens between well defined energy levels. At room temperature the width of the emission line can increase greatly, but is still at a well defined energy and can often be distinguished from other types of incoherent multiphoton emission sources. For this reason, in order to analyse the quality of the emitters, the samples are first studied by means of spectral analysis, which is much faster than cross correlation analysis. For instance, in the samples we prepared almost all the ion exposed areas showed fluorescent emission, with most of them presenting a very wide emission spectrum. Using a very low exposure dose

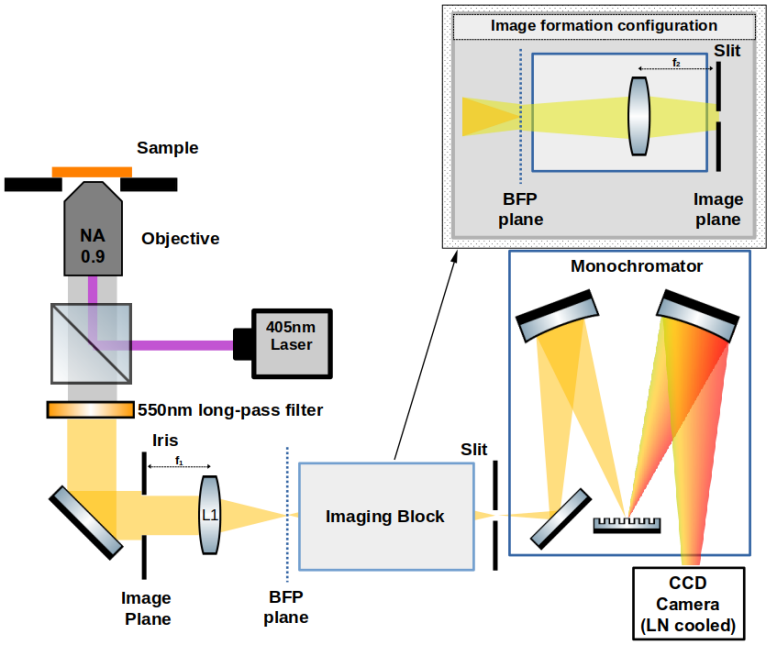

Figure 4.5: Scheme of the optical setup used for spectral analysis. Fluorescence of the sample is excited with a 405nm laser. The collected signal is filterer with a dichroic 550nm long pass filter and fed to a monocromator. A LN cooled CCD camera is used for the detection of the signal.

though changed the spectral behaviour and increased the probability of obtaining well defined spectral peaks, which may be associated to the presence of quantum emitters.

Measurement of the spectra was performed with an inverted fluorescence microscope in combination with a monochromator and a liquid Nitrogen (LN) cooled CCD camera as shown in Figure 4.5. Photoluminescence is excited by means of a 405nm unfocused laser (quantum TM) with variable power ($5 \div 50$mW) that, through a 550nm long pass dichroic filter, reaches the sample from the objective. The fluorescent image is therefore collected through the same objective (Nikon x100, NA 0.9) and projected on the entrance slit of a monochromator. By aligning the exposure pattern with the slit, it is possible to image on the collection CCD multiple exposed spots simultaneously, together with their respective spectra thanks to a rotation of the monochromator grating.

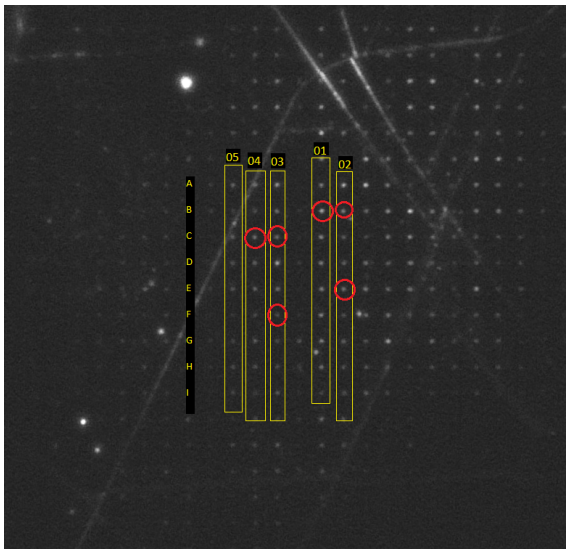

Figure 4.6: Fluorencence image of a flake where the exposed pattern is well visible. The image was taken using a laser power of $10mW$, unfocused on an area of $\approx 40x40\mu m^2$. Acquisition is performed over a 10s period. The yellow rectangles highlight the regions were spectral analysis was performed and the red circles highlight the emission centers with characteristic spectral profiles.

In Figure 4.6 the fluorescent image for a flake of 200nm thickness are shown. The exposure was performed with an acceleration voltage of 30keV and a dwell time ranging from (2μs and 100μs). The image reveals fluorescence from the exposed dot-matrix array and from other parts like flake edges and imperfections. Here different columns correspond to different doses, that are analysed one at a time with the monochromator. In the image, the rectangular yellow regions represent the portion of the image that has been fed to the monochromator slit. The spectral images of Figures 4.8 and 4.9 reveal the presence of multiple emission peaks. Most of the fluorescent spots appear as bright lines in the images, emitting with wide emission spectra below 700nm (much like the background fluorescence). Nonetheless, there are few spots where the emission is localised in narrower peaks, which position varies between $570 \div 640$nm and which width varies between $5 \div 20$nm. These can be better appreciated in Figure 4.7.

Unfortunately, due to a not sufficient sensitivity of the Nitrogen cooled CCD,

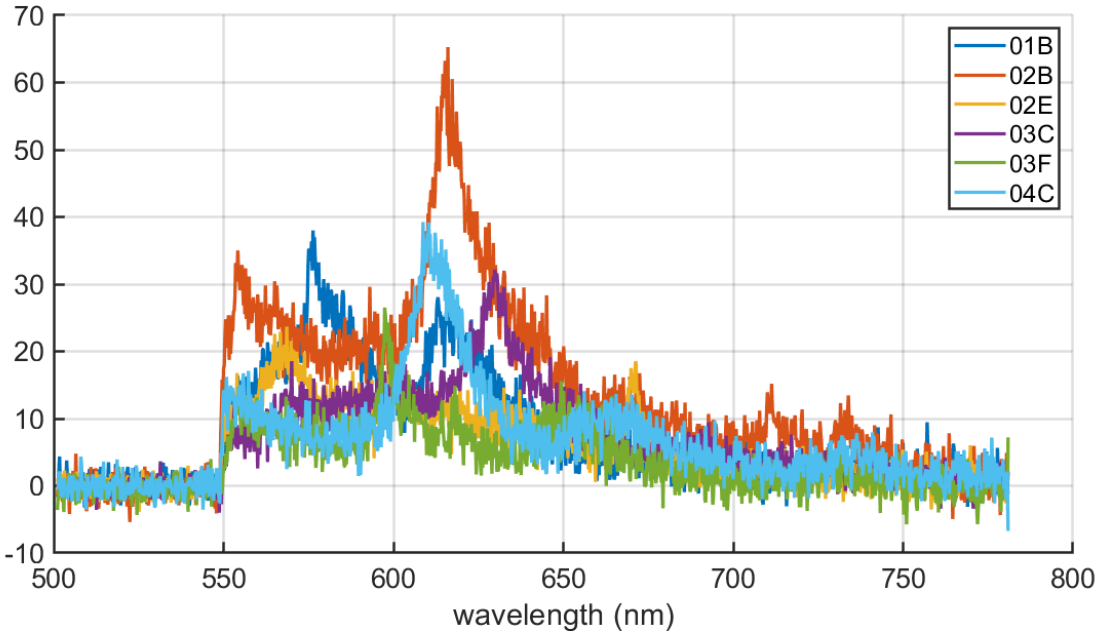

Figure 4.7: Intensity of the emission centers highlighted with red circles in Fig. 4.6. The emission peak are localized between $570 \div 640$nm. The intensity profile are extracted from the data in Figure 4.9

the fluorescence from samples exposed with a lower dose could not be measured with this setup.

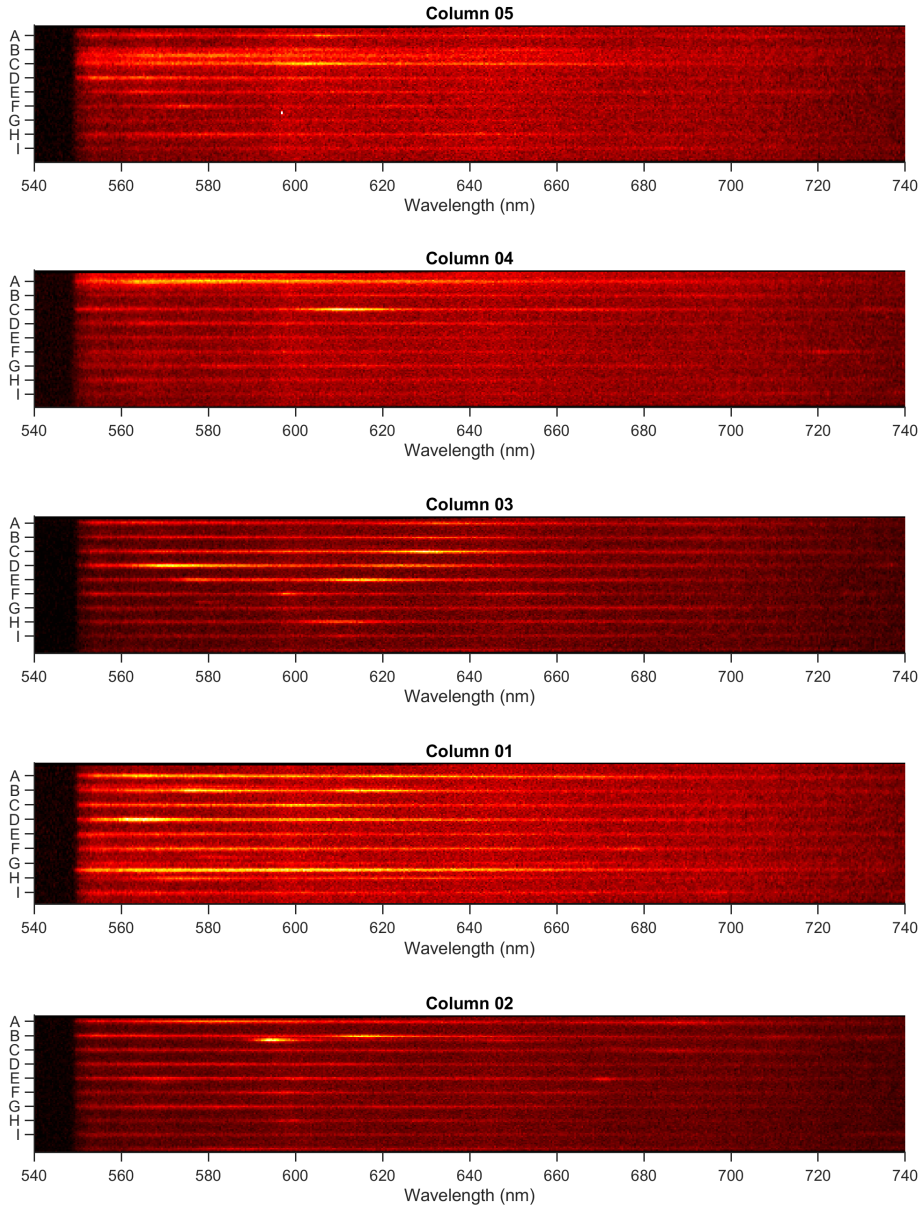

Figure 4.8: Row spectral measurements obtained on the CCD upon dispersion of the image of the dot-matrix in Figure 4.6. Each map represents a different column in Fig. 4.6, which correspond to a different exposure dose, here reported in increasing order from top to bottom.

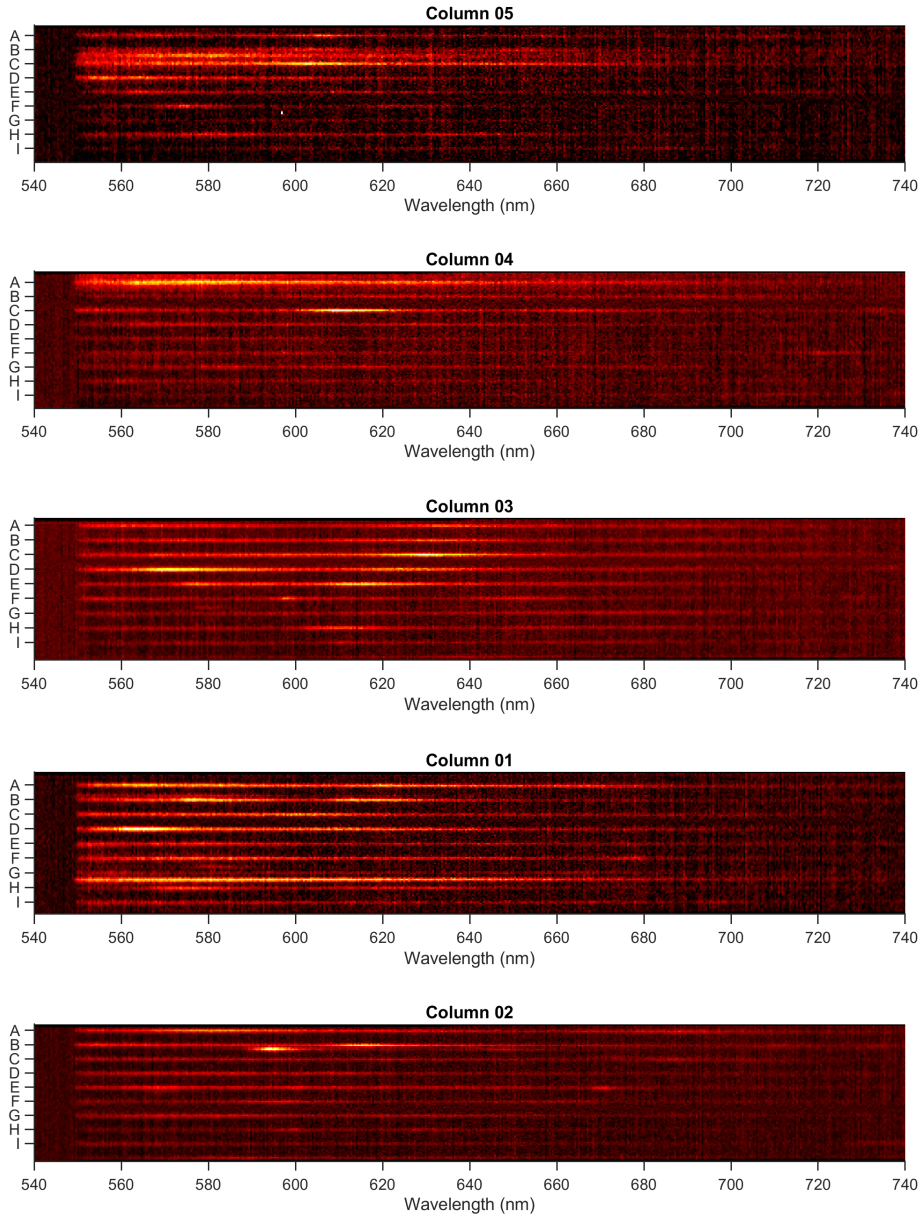

Figure 4.9: Row spectral measurements obtained on the CCD upon dispersion of the image of the dot-matrix in Figure 4.6. The maps here reported have been background filtered by subtracting the intensity measured in the regions outside the emission centers. Each map represents a different column in Fig. 4.6, which correspond to a different exposure dose, here reported in increasing order from top to bottom.

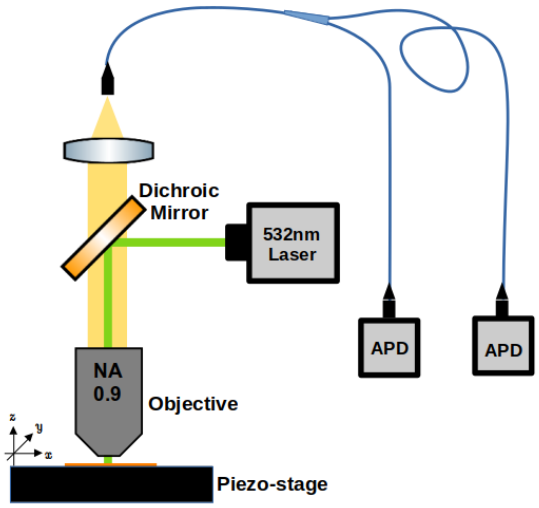

Figure 4.10: Optical setup for autocorrelation measurements

4.2.2 Room temperature confocal scanning for Autocorrelation Measurements

Autocorrelation measurements are a common method for characterizing the temporal properties of single-photon emission sources. In this technique, the emitted photons are sent through a beamsplitter and into two detectors, which are placed at a specific distance apart. The signals from the two detectors are then correlated as a function of the time delay between them. If the signal comes from a source emitting one photon at a time, then a dip in the correlation can be observed. Autocorrelation measurements are important because they allow to understand if a particular source is able to emit in the single-photon regime and they are also able to provide information about the coherence time and spectral linewidth of the emitted photons.

The autocorrelation measurements were performed in collaboration with the italian Institute of Metrology (INRIM). The setup used for this is presented in Figure 4.10 and consists of a piezoelectric, triaxis, translational stage, with some collection optics and an optical fiber that connects to two avalanche photodiods

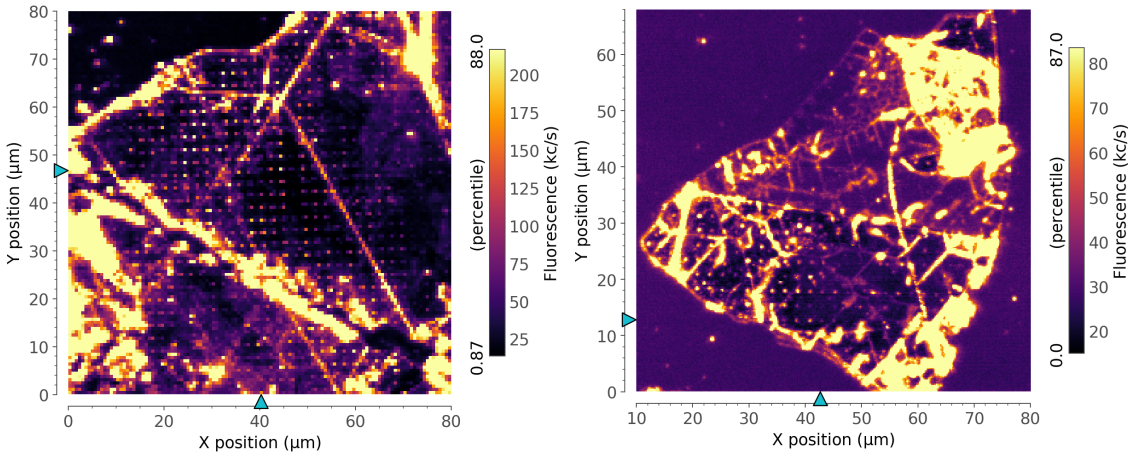

(a) (b)

Figure 4.11: Confocal maps of two hBN flakes. (a) shows the same flake analysed in Section 4.6. (b) shows a flake where presence of single photon emitters was detected. The red circle highlights the SPE reported in Figure 4.12.

(APD) detectors, one of which connected through a fiber splitter to a longer optical path. The two APD are connected to an a acquisition board, that records the arrival time of the detected photons. Then a software precesses these data, analysing the statistics of the difference in arrival time between the two detectors. This system allows to illuminate the sample with a focused laser, map the photoluminescence with very high precision and perform autocorrelation measurement in any of the scanned points.

Photoluminescence maps show again the presence of emission from most of the FIB exposed spots as well as from the edges and wrinkles of the flake. In Figure 4.11b, where the maps for a flake with different thicknesses is shown, it is possible to observe that the thinner part of the flake does not show any sign of fluorescence. This behaviour was confirmed from many other measurements where exposing very thin flakes of h-BN (few layers) did not produce any apparent luminescence. The flakes shown in the figure were exposed using $AV = 20$keV, with a dwell time ranging from (100μs and 300μs). Before

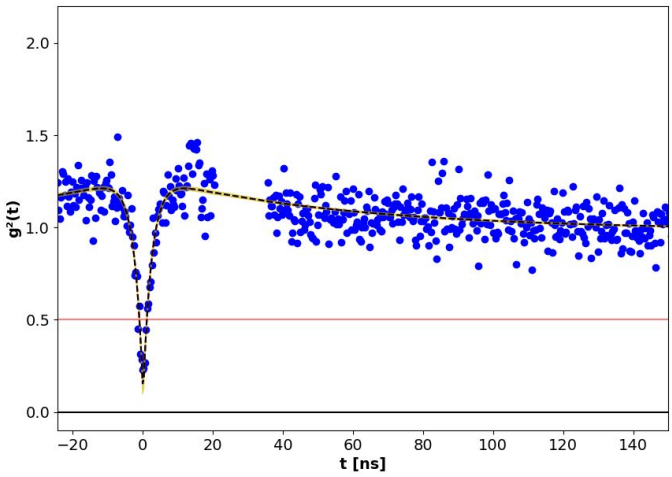

Figure 4.12: Single photon emission recorder on an h-BN flake after exposure with a Gallium FIB.

When measuring the second order correlation function $G^{(2)}$, it was found that many of the induced emitter present a dip in the recorded signal, but most of those did not reach a value lower that 0.25, which is commonly accepted to be the signature of single photon emission. Many other emitters instead, even though were promising, presented a very short lifespan, which was not sufficient to collect enough statistics. Nonetheless, few emitters showed a single photon behaviour. The $G^{(2)}$ measurement is presented in Figure 4.12.

For the sake of clarity, the model used for fitting the $G^{(2)}$ is presented:

$$G^{(2)} = I(1 - a \cdot e^{-\lambda_1|\tau-\tau_0|} + b \cdot e^{-\lambda_2|\tau-\tau_0|}), \tag{4.1}$$

This model assumes that the emission has two decay channels with characteristic decay times of λ_1 and λ_2, and with amplitudes a and b, respectively. The factor I represents the overall intensity of the emission. τ is the time delay between the detection of a photon arrival on the first detector and the following arrival on the other detector, therefore τ_0 is a the time length difference between the two

optical path to the two detectors. The first term in the parentheses represents the uncorrelated background contribution to the signal, while the second and third terms represent the correlated signal due to the two decay channels.

The choice of a double exponential model over a single exponential model is usually motivated by the desire to capture the multi-exponential decay behavior of the single-photon emitter. In some cases, a single exponential decay model may be sufficient to fit the data, but in other cases, the decay behavior may be more complex and require a double exponential model to accurately capture the decay dynamics.

4.3 The Flake Transfer

The initial and crucial step towards utilizing h-BN is the peeling and transfer of thin flakes from bulky crystal forms. The usability of the flakes in a device is highly dependent on their quality and size, in terms of thickness and area. For instance, for nanophotonic structures etched on top of dielectric multilayers, the flakes should be wider than the structures and as thin as possible to minimize the dielectric loading and the impact on design. On the other hand, for the generation of quantum emitters, unlike TMDs, it appears that using monolayer flakes is not strictly necessary.

The HPHT synthesis method produces crystals made of stacked bidimensional atomic layers held together by Wander Val forces, which can be easily overcome to separate the layers. The most commonly used method for obtaining flakes from bulky crystals is scotch tape peeling. This technique is akin to the one used for graphene and involves exploiting the adhesion forces of an adhesive tape to stick different sides of the bulky crystal and rip it in parts by stretching them apart. Repeating this process several times can yield flakes of various thicknesses, with

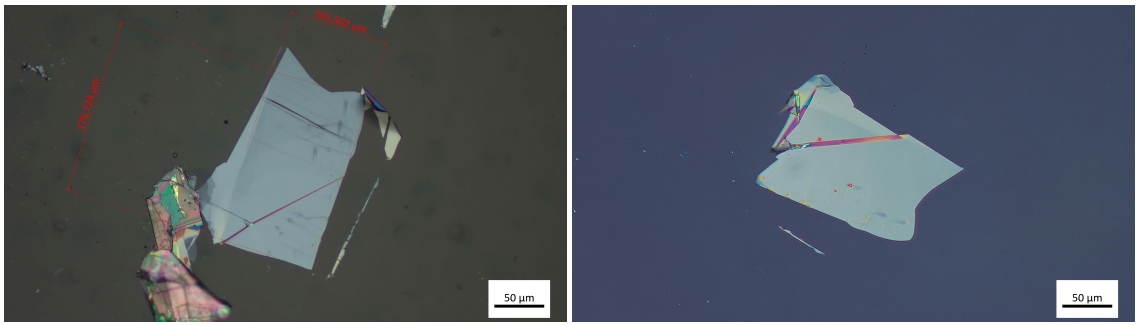

(a) (b)

Figure 4.13: Bright field images of a flake on Gelfilm (a) before the transfer and on Silicon wafer (b) after the transfer.

the quality of the peeling process determining the precision of the flakes obtained. After peeling, the flakes are typically transferred on the desired substrate by means of a transparent cantilever and an optical alignment setup [144].

In our specific case, the flakes were peeled from commercial h-BN crystals, first on a stronger adhesive PDMS tape by simply placing the material in between two tape slabs, then transferred on a weaker tape by means of simple contact. On this secondary tape, namely Gelfilm by Gel-pak®, the flakes are searched upon with the help of an optical microscope that allows to also approximately estimate their thickness by means contrast and colour analysis. Indeed, on a reflection optical microscope, h-BN appears with a wide variation of colours depending on their thickness [145, 146] and with a transmission microscope, possibly upon calibration, it is even possible to distinguish a monolayer from a bilayer flake while they are still on the tape. Gelfilm is a specific tape made of a thin PDMS slab sandwiched between a protective thin layer and a rigid, thicker and transparent plastic layer. Before interacting with h-BN, the tape is cut into a rectangular shape and only the protective layer is removed.

Once the desired flake is selected the tape is fixed on the border of a rigid cantilever, in such a way to expose the flake outside of the cantilever and this latter is placed on the alignment stage In Figure 4.14 it is possible to understand the tools

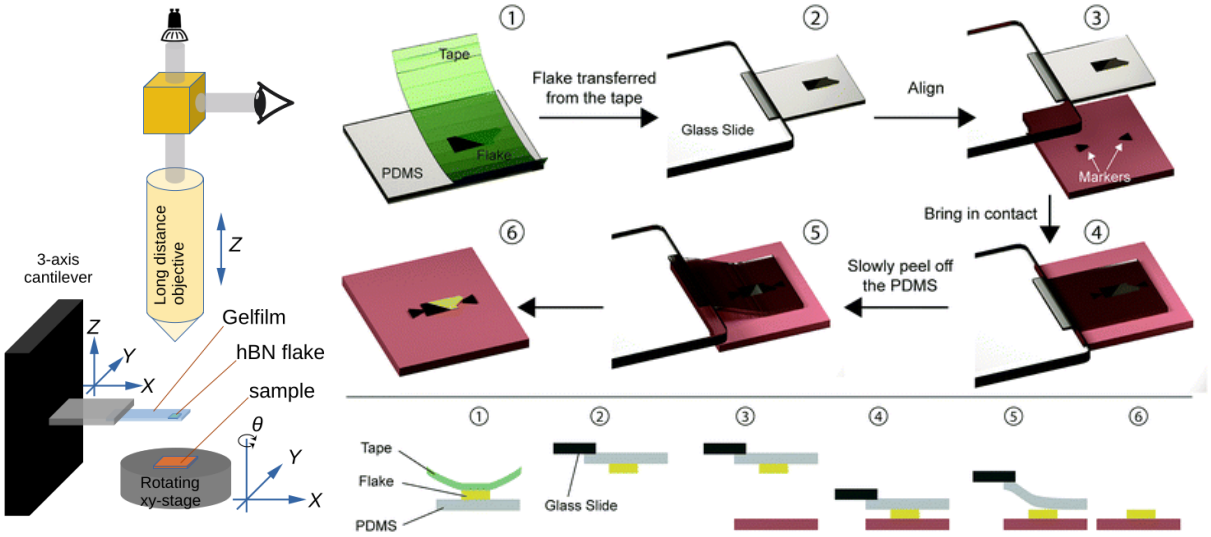

(a) (b)

Figure 4.14: (a) Scheme of the setup built to perform the flake transfer. (b) Scheme of the sequence of steps required to perform the flake transfer; image taken from [147].

that allow for aligning the Gelfilm tape with the sample. This latter is placed on a two axis translational stage in combination with a planar rotating stage. Above this the cantilever is placed on a triaxis translational stage, with the flake facing the sample. On top of both stages a long working distance objective is placed together with few optical elements to allow for image formation, with the objective combined with a single axis translational stage in order to adjust the focus. Upon adjustment of this latter stage, the objective is able to image the both flakes, through the rigid plastic layer of the tape, and the sample. With this setup the alignment can be achieved with few tens of microns precision.

4.4 Concluding remarks

In this chapter, we have investigated the potential of ion irradiation to generate single photon emitters (SPEs) in hexagonal boron nitride (hBN). Using an approach similar to [136] and [140], we showed that SPE can be induce in localized regions by controlling the dose of the ion exposure. While further work is required to

fully characterize the optimal conditions for SPE generation, this study provides compelling evidence for the feasibility of this approach.

The necessity of thermal annealing for the activation of the emitters is a critical part of this process. In particular, it can be detrimental to multilayered structures such as the dielectric multilayers that host Bloch surface waves discussed in previous chapters. High temperature can cause the formation of cracks and wrinkles on the structures due to the differences in expansion coefficients of the materials involved. To overcome this issue, one possibility is to explore the use of rapid thermal annealing (RTA) which may reduce the stress on the sample. Alternatively, thicker substrates for the multilayers could be used to avoid the formation of wrinkles and cracks, but this would prevent the use of oil immersion objectives and related measurement techniques, like the ones described in Chapter 2. Another option may be to use the nanopfrazor (a thermal SPM technique) presented in Chapter 2 for extremely localized thermal annealing. The tip of this machine can reach temperatures up to 1000°C, but it is unclear if the contact with an ion-exposed area could be sufficient to activate the emitters. Finally, high energy plasma treatments could be worth exploring to test their effects on these types of defects.

Another critical aspect of this process is the use of the focused ion beam on insulating substrates. In facts, multiple tests with thermally oxidized $Si/SiO2$ wafers and glass substrates have found very difficult to use the ion beam to damage the flake, due to a stronger charging effect. To overcome this issue, a few alternatives could be explored. One possibility is the use of charge compensation with simultaneous exposure to an electron beam. This method was tested but it has not produced any characteristic spectral signatures or single photon emissions. Another possibility worth exploring could be the use of metallic coatings to create a very thin conductive layer that would completely remove the charging problem. However, the removal of the metal may carry the hBN flake with it, which would present another challenge.

Chapter 5

Summary and perspectives

In this thesis a number of different ways for controlling nanophotonic devices has been explored. The results presented in Chapter 2 offer an intriguing approach for controlling resonant nanocavities by means of optically induced anisotropies. The method can be potentially applied to all sorts of nanophotonic devices, ranging from Silica waveguides to surface plasmon polaritons (SPPs), but, in order develop this approach further, new techniques for the fabrication of the polymeric layers should be tested. In facts, the main challenge of this work came from the introduction of the azopolymer into the lithographic polymer, which disrupted the normal working mechanism of the latter, rendering the lithographic process more cumbersome. An interesting approach could be to develop a lift-off process or a masked etching process, to inscribe the various patterns on the polymer without the need of directly exposing the modified polymer. Of course this would come with its own challenges, like the aspect ratio of the features to be inscribed and the selectivity of the solvents towards the polymer. Finally, it would be interesting to test new kinds of structures, such as integrated beam splitters and multiplexer either designed for BSWs or even SOI, to see if a variation in the dielectric properties of the material could be exploited to obtain a high level of control over such devices.

The numerical results presented in Chapter 3 have shown a promising future for

metasurface gratings. The ability to fully control the angular momentum of photons emitted by a SPE is intriguing, but there are still many challenges to overcome. The main of which is obviously the ability to place the SPE at the center of the structures, and the research presented in Chapter 4 works in that direction. In order to overcome the fabrication problems that dielectric multilayers present, an alternative design to a standard BSW was proposed, with the nanopatterned layer buried below the last dielectric layer. Although this design seems promising, it would be interesting to test the same metasurfaces also on silica slab waveguides or even on SOI waveguides designed to work in the infrared.

Finally, in Chapter 4 some advancements in the fabrication of room temperature SPEs were presented. Following the most recent developments of this field, h-BN was explored as an ideal candidate for the generation of on-demand SPEs. In the attempt of replicating some of the results of the literature, FIB damaging was addressed as the most promising approach. Although the presented results are not mature enough to allow for the implementation of h-BN into the metasurface gratings of Chapter 3, it was shown that that a FIB exposure followed by a thermal annealing is able to induce a SPEs that work at room temperature. Being an early result, the future of this activity is straight forward, as there are many possibilities for improvements, already discussed at the end of Chapter 4. Amongst the topics researched in the thesis, this is probably the one with most potential, since SPEs can find applications in any sort of nanophotonic device, especially with the advent of quantum technologies.

Overall the research presented in this thesis offered an interesting perspective on the possibilities offered by Bloch surface waves and dielectric multilayers, while laying some foundational work for the development of new nanophotonic devices.

Author's Contribution

The research presented in this thesis is an original work carried on by the author. In general, unless specified otherwise, the presented work was carried out by the author himself. That applies both to the creation of the experimental setup, together with the consequent measurements, the fabrication processes and to all the simulations. Important external contributions to be highlighted are from Marina Giordano and her collaborators, who fabricated the devices presented in Chapter 2; from the researchers at the CNR of Lecce, who helped in the initial fabrication of the h-BN SPEs; from researches at INRIM, who performed the autocorrelation measurements presented in Chapter 4; and from Emiliano Descrovi who supervised and helped the whole activity, both from a theoretical and an experimental standpoint.

Bibliography

[1] C. Fedele, P. A. Netti, and S. Cavalli. "Azobenzene-based polymers: emerging applications as cell culture platforms". In: *Biomaterials Science* 6.5 (May 1, 2018), pp. 990–995. ISSN: 2047-4849. DOI: 10.1039/C8BM00019K. (Visited on 09/11/2020).

[2] Angelo Angelini et al. "Reconfigurable elastomeric graded-index optical elements controlled by light". In: *Light: Science & Applications* 7.1 (May 23, 2018), p. 7. ISSN: 2047-7538. DOI: 10.1038/s41377-018-0005-1. (Visited on 07/06/2020).

[3] Kanishk Mehta et al. "Design and applications of light responsive liquid crystal polymer thin films". In: *Applied Physics Reviews* 7.4 (Nov. 5, 2020), p. 041306. ISSN: 1931-9401. DOI: 10.1063/5.0014619. (Visited on 11/15/2020).

[4] Marina Pilz da Cunha et al. "A Soft Transporter Robot Fueled by Light". In: *Advanced Science* 7.5 (Mar. 2020), p. 1902842. ISSN: 2198-3844, 2198-3844. DOI: 10.1002/advs.201902842. (Visited on 09/20/2020).

[5] Alberto Puliafito et al. "Driving Cells with Light-Controlled Topographies". In: *Advanced Science* 6.14 (2019), p. 1801826. ISSN: 2198-3844. DOI: 10.1002/advs.201801826. (Visited on 07/06/2020).

[6] Heng Zhou et al. "Spatial light modulator-based programmable J-plate for the arbitrary spin-to-orbital angular momentum conversion of lights". In:

Applied Physics B 125.3 (Feb. 14, 2019), p. 42. ISSN: 1432-0649. DOI: 10.1007/s00340-019-7162-7. (Visited on 09/28/2020).

[7] Robert C. Devlin et al. "Arbitrary spin-to–orbital angular momentum conversion of light". In: *Science* 358.6365 (Nov. 17, 2017), pp. 896–901. ISSN: 0036-8075, 1095-9203. DOI: 10.1126/science.aao5392. (Visited on 09/28/2020).

[8] Kévin G. Cognée et al. "Generation of Pure OAM Beams with a Single State of Polarization by Antenna-Decorated Microdisk Resonators". In: *ACS Photonics* 7.11 (Nov. 18, 2020), pp. 3049–3060. DOI: 10.1021/acsphotonics.0c01081. (Visited on 12/07/2020).

[9] Domitille Schanne et al. "Spontaneous Emission of Vector Vortex Beams". en. In: *Phys. Rev. Applied* 14.6 (Dec. 2020). Publisher: American Physical Society, p. 064077. ISSN: 2331-7019. DOI: 10.1103/PhysRevApplied.14.064077. URL: https://link.aps.org/doi/10.1103/PhysRevApplied.14.064077 (visited on 02/09/2021).

[10] P. Törmä and W. L. Barnes. "Strong coupling between surface plasmon polaritons and emitters: a review". In: *Reports on Progress in Physics* 78.1 (Dec. 2014), p. 013901. ISSN: 0034-4885. DOI: 10.1088/0034-4885/78/1/013901. (Visited on 08/25/2021).

[11] Yinhui Kan et al. "Metasurface-Enabled Generation of Circularly Polarized Single Photons". In: *Advanced Materials* 32.16 (2020). ISSN: 1521-4095. DOI: 10.1002/adma.201907832. (Visited on 09/11/2020).

[12] Thibault Chervy et al. "Room Temperature Chiral Coupling of Valley Excitons with Spin-Momentum Locked Surface Plasmons". In: *ACS Photonics* 5.4 (Apr. 18, 2018). Publisher: American Chemical Society, pp. 1281–1287. DOI: 10.1021/acsphotonics.7b01032. (Visited on 08/25/2021).

[13] S. Kumar, A. Kaczmarczyk, and B. D. Gerardot. "Strain-Induced Spatial and Spectral Isolation of Quantum Emitters in Mono- and Bilayer WSe2". In: *Nano Letters* 15.11 (Nov. 11, 2015), pp. 7567–7573. ISSN: 1530-6984. DOI: 10.1021/acs.nanolett.5b03312. (Visited on 05/10/2021).

[14] Carmen Palacios-Berraquero et al. "Large-scale quantum-emitter arrays in atomically thin semiconductors". In: *Nature Communications* 8.1 (May 22, 2017), p. 15093. ISSN: 2041-1723. DOI: 10.1038/ncomms15093. (Visited on 05/10/2021).

[15] Artur Branny et al. "Deterministic strain-induced arrays of quantum emitters in a two-dimensional semiconductor". In: *Nature Communications* 8.1 (May 22, 2017), p. 15053. ISSN: 2041-1723. DOI: 10.1038/ncomms15053. (Visited on 05/10/2021).

[16] Chi Li et al. "Scalable and Deterministic Fabrication of Quantum Emitter Arrays from Hexagonal Boron Nitride". In: *Nano Lett.* 21.8 (Apr. 2021). Publisher: American Chemical Society, pp. 3626–3632. ISSN: 1530-6984. DOI: 10.1021/acs.nanolett.1c00685. URL: https://doi.org/10.1021/acs.nanolett.1c00685 (visited on 06/08/2021).

[17] Noah Mendelson et al. "Identifying carbon as the source of visible single-photon emission from hexagonal boron nitride". In: *Nature Materials* 20.3 (Mar. 2021), pp. 321–328. ISSN: 1476-4660. DOI: 10.1038/s41563-020-00850-y. (Visited on 07/26/2021).

[18] Clarisse Fournier et al. "Position-controlled quantum emitters with reproducible emission wavelength in hexagonal boron nitride". en. In: *Nat Commun* 12.1 (June 2021). Bandiera_abtest: a Cc_license_type: cc_by Cg_type: Nature Research Journals Number: 1 Primary_atype: Research Publisher:

Nature Publishing Group Subject_term: Single photons and quantum effects;Two-dimensional materials Subject_term_id: single-photons-and-quantum-effects;two-dimensional-materials, p. 3779. ISSN: 2041-1723. DOI: 10.1038/s41467-021-24019-6. URL: https://www.nature.com/articles/s41467-021-24019-6 (visited on 07/09/2021).

[19] Yongliang Chen et al. "Generation of High-Density Quantum Emitters in High-Quality, Exfoliated Hexagonal Boron Nitride". In: *ACS Applied Materials & Interfaces* (Sept. 22, 2021). ISSN: 1944-8244. DOI: 10.1021/acsami.1c14863. (Visited on 09/24/2021).

[20] Toan Trong Tran et al. "Quantum emission from hexagonal boron nitride monolayers". In: *Nature Nanotechnology* 11.1 (Jan. 2016), pp. 37–41. ISSN: 1748-3395. DOI: 10.1038/nnano.2015.242. (Visited on 06/08/2021).

[21] Toan Trong Tran et al. "Robust Multicolor Single Photon Emission from Point Defects in Hexagonal Boron Nitride". In: *ACS Nano* 10.8 (Aug. 2016). Publisher: American Chemical Society, pp. 7331–7338. ISSN: 1936-0851. DOI: 10.1021/acsnano.6b03602. URL: https://doi.org/10.1021/acsnano.6b03602 (visited on 07/09/2021).

[22] Gabriele Grosso et al. "Tunable and high-purity room temperature single-photon emission from atomic defects in hexagonal boron nitride". en. In: *Nat Commun* 8.1 (Sept. 2017). Number: 1 Publisher: Nature Publishing Group, p. 705. ISSN: 2041-1723. DOI: 10.1038/s41467-017-00810-2. URL: https://www.nature.com/articles/s41467-017-00810-2/briefing/signup/ (visited on 06/08/2021).

[23] E-karimi. *Left and right handed circular polarization*. 2011. URL: https://en.wikipedia.org/wiki/File:Sam_v1.png.

[24] E-karimi. *Helical beam with different topological charge*. 2011. URL: https://en.wikipedia.org/wiki/File:Helix_oam.png.

[25] Katsunari Okamoto. *Fundamentals of optical waveguides*. 2nd ed. Amsterdam ; Boston: Elsevier, 2006. ISBN: 978-0-12-525096-2.

[26] Eli Yablonovitch. "Inhibited Spontaneous Emission in Solid-State Physics and Electronics". In: *Phys. Rev. Lett.* 58.20 (May 1987). Publisher: American Physical Society, pp. 2059–2062. DOI: 10.1103/PhysRevLett.58.2059. URL: https://link.aps.org/doi/10.1103/PhysRevLett.58.2059 (visited on 04/13/2023).

[27] Sajeev John. "Strong localization of photons in certain disordered dielectric superlattices". In: *Phys. Rev. Lett.* 58.23 (June 1987). Publisher: American Physical Society, pp. 2486–2489. DOI: 10.1103/PhysRevLett.58.2486. URL: https://link.aps.org/doi/10.1103/PhysRevLett.58.2486 (visited on 04/13/2023).

[28] Igor A. Sukhoivanov and Igor V. Guryev. *Photonic Crystals: Physics and Practical Modeling*. en. Vol. 152. Springer Series in Optical Sciences. Berlin, Heidelberg: Springer Berlin Heidelberg, 2009. ISBN: 978-3-642-02645-4 978-3-642-02646-1. DOI: 10.1007/978-3-642-02646-1. URL: https://link.springer.com/10.1007/978-3-642-02646-1 (visited on 04/14/2023).

[29] Massachusetts: The MathWorks Inc. Natick. *MATLAB, version R2019+*.

[30] Niccolò Marcucci. *Repository containing functions for multilayer analysis in TMM*. 2020. URL: https://github.com/Niccolo-Marcucci/Lumerical-Objects/tree/master/multilayer_design/functions.

[31] Niccolò Marcucci. *Repository for meep, python simulations codes*. 2022. URL: https://github.com/Niccolo-Marcucci/meep_objects.

[32] Lumerical Inc. *Lumerical DEVICE Multiphysics Simulation Suit, FDTD, version 2019/21*.

[33] Ardavan F Oskooi et al. "MEEP: A flexible free-software package for electromagnetic simulations by the FDTD method". In: *Computer Physics Communications* 181.3 (2010), pp. 687–702. DOI: 10.1016/j.cpc.2009.11.008.

[34] Niccolò Marcucci. *Repository for Lumerical 2D simulations of circular cavities*. 2020. URL: https://github.com/Niccolo-Marcucci/2D-circular_cavity.

[35] Niccolò Marcucci. *Repository for Lumerical full 3D simulations*. 2020. URL: https://github.com/Niccolo-Marcucci/Circular_cavity_with_spiral_outcoupler.

[36] Niccolò Marcucci. *Repository for meep, python simulations codes*. 2022. URL: https://github.com/Niccolo-Marcucci/Nanophotonics-meep.

[37] Mohammad Taghinejad and Wenshan Cai. "All-Optical Control of Light in Micro- and Nanophotonics". en. In: *ACS Photonics* 6.5 (May 2019). Number: 5, pp. 1082–1093. ISSN: 2330-4022, 2330-4022. DOI: 10.1021/acsphotonics.9b00013. URL: https://pubs.acs.org/doi/10.1021/acsphotonics.9b00013 (visited on 08/25/2022).

[38] Yuhao Wu et al. "Zinc oxide (ZnO) hybrid metasurfaces exhibiting broadly tunable topological properties". en. In: *Nanophotonics* 11.17 (Aug. 2022). Number: 17, pp. 3933–3942. ISSN: 2192-8614. DOI: 10.1515/nanoph-2022-0115. URL: https://www.degruyter.com/document/doi/10.1515/nanoph-2022-0115/html (visited on 08/24/2022).

[39] Joo Hwan Ko et al. "A review of tunable photonics: Optically active materials and applications from visible to terahertz". en. In: *iScience* 25.8 (Aug. 2022). Number: 8, p. 104727. ISSN: 25890042. DOI: 10.1016/j.isci.2022.104727. URL: https://linkinghub.elsevier.com/retrieve/pii/S2589004222009993 (visited on 09/25/2022).

[40] Florica Adriana Jerca, Valentin Victor Jerca, and Richard Hoogenboom. "Advances and opportunities in the exciting world of azobenzenes". In: *Nature Reviews Chemistry* 6.1 (Jan. 2022). Number: 1, pp. 51–69. ISSN: 2397-3358. DOI: 10.1038/s41570-021-00334-w. URL: https://doi.org/10.1038/s41570-021-00334-w.

[41] Dasari Venkatakrishnarao et al. "Photonic Microrods Composed of Photoswitchable Molecules: Erasable Heterostructure Waveguides for Tunable Optical Modulation". en. In: *Advanced Optical Materials* 3.8 (Aug. 2015). Number: 8, pp. 1035–1040. ISSN: 21951071. DOI: 10.1002/adom.201500106. URL: https://onlinelibrary.wiley.com/doi/10.1002/adom.201500106 (visited on 09/25/2022).

[42] S. De Martino, F. Mauro, and P. A. Netti. "Photonic applications of azobenzene molecules embedded in amorphous polymer". en. In: *Riv. Nuovo Cim.* 43.12 (Dec. 2020), pp. 599–629. ISSN: 1826-9850. DOI: 10.1007/s40766-021-00014-x. URL: https://doi.org/10.1007/s40766-021-00014-x (visited on 05/30/2022).

[43] Andre Kovach et al. "Optically tunable microresonator using an azobenzene monolayer". In: *AIP Advances* 10.4 (Apr. 2020). Publisher: American Institute of Physics, p. 045117. DOI: 10.1063/1.5143253. URL: https://aip.scitation.org/doi/10.1063/1.5143253 (visited on 09/29/2020).

[44] Jinghan He et al. "All-optical reversible control of integrated resonant cavity by a self-assembled azobenzene monolayer". EN. In: *Opt. Express, OE* 28.15 (July 2020). Publisher: Optical Society of America, pp. 22462–22477. ISSN: 1094-4087. DOI: 10.1364/OE.397776. URL: https://www.osapublishing.org/oe/abstract.cfm?uri=oe-28-15-22462 (visited on 09/25/2020).

[45] Edgar O. Owiti et al. "Polarization Converter with Controllable Birefringence Based on Hybrid All-Dielectric-Graphene Metasurface". en. In: *Nanoscale*

Res Lett 13.1 (Dec. 2018). Number: 1, p. 38. ISSN: 1931-7573, 1556-276X. DOI: 10.1186/s11671-017-2413-1. URL: https://nanoscalereslett.springeropen.com/articles/10.1186/s11671-017-2413-1 (visited on 09/26/2022).

[46] Yadong Deng et al. "Recent progress in metasurface-enabled optical waveplates". en. In: *Nanophotonics* 11.10 (May 2022). Number: 10, pp. 2219–2244. ISSN: 2192-8614. DOI: 10.1515/nanoph-2022-0030. URL: https://www.degruyter.com/document/doi/10.1515/nanoph-2022-0030/html (visited on 09/26/2022).

[47] Niccolò Marcucci et al. "Spectral tuning of Bloch Surface Wave resonances by light-controlled optical anisotropy:" en. In: *Nanophotonics* 12.6 (Mar. 2023). Publisher: De Gruyter, pp. 1091–1104. ISSN: 2192-8614. DOI: 10.1515/nanoph-2022-0609. URL: https://www.degruyter.com/document/doi/10.1515/nanoph-2022-0609/html (visited on 04/02/2023).

[48] Edoardo Albisetti et al. "Thermal scanning probe lithography". en. In: *Nat Rev Methods Primers* 2.1 (May 2022). Number: 1 Publisher: Nature Publishing Group, pp. 1–21. ISSN: 2662-8449. DOI: 10.1038/s43586-022-00110-0. URL: http://www.nature.com/articles/s43586-022-00110-0 (visited on 05/31/2022).

[49] Nolan Lassaline et al. "Optical Fourier surfaces". en. In: *Nature* 582.7813 (June 2020). Number: 7813, pp. 506–510. ISSN: 0028-0836, 1476-4687. DOI: 10.1038/s41586-020-2390-x. URL: http://www.nature.com/articles/s41586-020-2390-x (visited on 09/19/2022).

[50] D. G. Zhang et al. "Active control of surface plasmon polaritons by optical isomerization of an azobenzene polymer film". en. In: *Appl. Phys. Lett.* 95.10 (Sept. 2009). Number: 10, p. 101102. ISSN: 0003-6951, 1077-3118. DOI: 10.

1063/1.3225156. URL: http://aip.scitation.org/doi/10.1063/1.3225156 (visited on 11/04/2020).

[51] Tatiana Kovalevich et al. "Experimental evidence of Bloch surface waves on photonic crystals with thin-film LiNbO_3 as a top layer". en. In: *Photon. Res.* 5.6 (Dec. 2017). Number: 6, p. 649. ISSN: 2327-9125. DOI: 10.1364/PRJ.5.000649. URL: https://opg.optica.org/abstract.cfm?URI=prj-5-6-649 (visited on 08/02/2022).

[52] Jacques Delaire and Keitaro Nakatani. "Linear and Nonlinear Optical Properties of Photochromic Molecules and Materials". In: *Chemical reviews* 100 (June 2000), pp. 1817–1846. DOI: 10.1021/cr980078m.

[53] Maria-Melanie Russew and Stefan Hecht. "Photoswitches: From Molecules to Materials". In: *Advanced Materials* 22.31 (2010), pp. 3348–3360. DOI: 10.1002/adma.200904102.

[54] G. Sudesh Kumar and D. C. Neckers. "Photochemistry of azobenzene-containing polymers". In: *Chemical Reviews* 89.8 (1989), pp. 1915–1925. DOI: 10.1021/cr00098a012.

[55] Ruxue Wang et al. "Bloch surface waves confined in one dimension with a single polymeric nanofibre". eng. In: *Nat Commun* 8 (Feb. 2017), p. 14330. ISSN: 2041-1723. DOI: 10.1038/ncomms14330.

[56] Kyung Min Lee et al. "Phototriggered Depolymerization of Flexible Poly(phthalaldehyde) Substrates by Integrated Organic Light-Emitting Diodes". In: *ACS Appl. Mater. Interfaces* 10.33 (Aug. 2018). Publisher: American Chemical Society, pp. 28062–28068. ISSN: 1944-8244. DOI: 10.1021/acsami.8b08181. URL: https://doi.org/10.1021/acsami.8b08181 (visited on 07/19/2022).

[57] P. Rochon et al. “Guided mode resonance filters using polymer films”. en. In: *Appl. Phys. Lett.* 71.8 (Aug. 1997). Number: 8, pp. 1008–1010. ISSN: 0003-6951, 1077-3118. DOI: 10.1063/1.119710. URL: http://aip.scitation.org/doi/10.1063/1.119710 (visited on 08/07/2022).

[58] F. Lagugné-Labarthet et al. “Chromophore Orientations in a Nonlinear Optical Azopolymer Diffraction Grating: Even and Odd Order Parameters from Far-Field Raman and Near-Field Second Harmonic Generation Microscopies”. en. In: *J. Phys. Chem. B* 108.44 (Nov. 2004). Number: 44, pp. 17059–17068. ISSN: 1520-6106, 1520-5207. DOI: 10.1021/jp047117k. URL: https://pubs.acs.org/doi/10.1021/jp047117k (visited on 08/24/2022).

[59] Ipsita Chakraborty and Hiroshi Kano. “Microscopic-characterization of photo-induced birefringence of azo-polymer thin film by focused surface plasmon”. en. In: *Optics & Laser Technology* 147 (Mar. 2022), p. 107673. ISSN: 0030-3992. DOI: 10.1016/j.optlastec.2021.107673. URL: https://www.sciencedirect.com/science/article/pii/S0030399221007611 (visited on 06/09/2022).

[60] Almeria Natansohn and Paul Rochon. “Photoinduced Motions in Azo-Containing Polymers”. en. In: *Chem. Rev.* 102.11 (Nov. 2002). Number: 11, pp. 4139–4176. ISSN: 0009-2665, 1520-6890. DOI: 10.1021/cr970155y. URL: https://pubs.acs.org/doi/10.1021/cr970155y (visited on 10/01/2020).

[61] F. Lagugné Labarthet, T. Buffeteau, and C. Sourisseau. “Azopolymer Holographic Diffraction Gratings: Time Dependent Analyses of the Diffraction Efficiency, Birefringence, and Surface Modulation Induced by Two Linearly Polarized Interfering Beams”. In: *J. Phys. Chem. B* 103.32 (Aug. 1999). Publisher: American Chemical Society, pp. 6690–6699. ISSN: 1520-6106. DOI:

10.1021/jp990752j. URL: https://doi.org/10.1021/jp990752j (visited on 07/19/2022).

[62] David J. McGee et al. "Photo-induced refractive index and topographical surface gratings in functionalized nanocarbon solid film". en. In: *Appl. Phys. Lett.* 107.18 (Nov. 2015). Number: 18, p. 181102. ISSN: 0003-6951, 1077-3118. DOI: 10.1063/1.4934864. URL: http://aip.scitation.org/doi/10.1063/1.4934864 (visited on 08/25/2022).

[63] Evgeni A. Bezus, Dmitry A. Bykov, and Leonid L. Doskolovich. "Integrated diffraction gratings on the Bloch surface wave platform supporting bound states in the continuum". en. In: *Nanophotonics* 10.17 (Nov. 2021). Number: 17, pp. 4331–4340. ISSN: 2192-8614. DOI: 10.1515/nanoph-2021-0352. URL: https://www.degruyter.com/document/doi/10.1515/nanoph-2021-0352/html (visited on 05/30/2022).

[64] Michele Scaravilli et al. "Grating-coupling-based excitation of Bloch surface waves for lab-on-fiber optrodes". en. In: *Opt. Express* 24.24 (Nov. 2016). Number: 24, p. 27771. ISSN: 1094-4087. DOI: 10.1364/OE.24.027771. URL: https://opg.optica.org/abstract.cfm?URI=oe-24-24-27771 (visited on 08/26/2022).

[65] Tatiana Kovalevich et al. "Polarization controlled directional propagation of Bloch surface wave". en. In: *Opt. Express* 25.5 (Mar. 2017). Number: 5, p. 5710. ISSN: 1094-4087. DOI: 10.1364/OE.25.005710. URL: https://opg.optica.org/abstract.cfm?URI=oe-25-5-5710 (visited on 08/26/2022).

[66] Kirill R. Safronov et al. "Miniature Otto Prism Coupler for Integrated Photonics". en. In: *Laser & Photonics Reviews* (Jan. 2022), p. 2100542. ISSN: 1863-8880, 1863-8899. DOI: 10.1002/lpor.202100542. URL: https://

onlinelibrary.wiley.com/doi/10.1002/lpor.202100542 (visited on 01/31/2022).

[67] Dmitry N. Gulkin et al. "Mie-driven directional nanocoupler for Bloch surface wave photonic platform". en. In: *Nanophotonics* 10.11 (Aug. 2021). Number: 11, pp. 2939–2947. ISSN: 2192-8614. DOI: 10.1515/nanoph-2021-0295. URL: https://www.degruyter.com/document/doi/10.1515/nanoph-2021-0295/html (visited on 09/08/2021).

[68] Yifeng Xiang et al. "Trapping metallic particles using focused Bloch surface waves". In: *Nanoscale* 12.3 (2020). Number: 3 Publisher: The Royal Society of Chemistry, pp. 1688–1696. ISSN: 2040-3364. DOI: 10.1039/C9NR08399E. URL: http://dx.doi.org/10.1039/C9NR08399E.

[69] Tommaso Perani, Daniele Aurelio, and Marco Liscidini. "Bloch-surface-wave photonic crystal nanobeam cavity". en. In: *Opt. Lett.* 44.21 (Nov. 2019). Number: 21, p. 5133. ISSN: 0146-9592, 1539-4794. DOI: 10.1364/OL.44.005133. URL: https://www.osapublishing.org/abstract.cfm?URI=ol-44-21-5133 (visited on 01/21/2022).

[70] Maria Caterina Giordano et al. "Deterministic Thermal Sculpting of Large-Scale 2D Semiconductor Nanocircuits". In: *arXiv e-prints* (Sept. 2022), arXiv:2209.11090. URL: https://ui.adsabs.harvard.edu/abs/2022arXiv220911090C.

[71] F. Lagugné-Labarthet, T. Buffeteau, and C. Sourisseau. "Inscription of holographic gratings using circularly polarized light: influence of the optical set-up on the birefringence and surface relief grating properties". en. In: *Applied Physics B: Lasers and Optics* 74.2 (Feb. 2002). Number: 2, pp. 129–137. ISSN: 0946-2171, 1432-0649. DOI: 10.1007/s003400100786. URL: http://link.springer.com/10.1007/s003400100786 (visited on 08/25/2022).

[72] P. Pagliusi et al. "Tunable Surface Patterning of Azopolymer by Vectorial Holography: The Role of Photoanisotropies in the Driving Force". In: *ACS*

Appl. Mater. Interfaces 11.37 (Sept. 2019). Number: 37 Publisher: American Chemical Society, pp. 34471–34477. ISSN: 1944-8244. DOI: 10.1021/acsami.9b12624. URL: https://doi.org/10.1021/acsami.9b12624.

[73] Liliana Moscardi et al. "Stimuli-Responsive Photonic Crystals". en. In: *Applied Sciences* 11.5 (Feb. 2021). Number: 5, p. 2119. ISSN: 2076-3417. DOI: 10.3390/app11052119. URL: https://www.mdpi.com/2076-3417/11/5/2119 (visited on 09/02/2022).

[74] Arri Priimagi et al. "Hydrogen-Bonded PolymerAzobenzene Complexes: Enhanced Photoinduced Birefringence with High Temporal Stability through Interplay of Intermolecular Interactions". In: *Chem. Mater.* 20.20 (Oct. 2008). Number: 20 Publisher: American Chemical Society, pp. 6358–6363. ISSN: 0897-4756. DOI: 10.1021/cm800908m. URL: https://doi.org/10.1021/cm800908m.

[75] Zhiyuan Qian et al. "Spontaneous emission in micro- or nanophotonic structures". en. In: *PhotoniX* 2.1 (Dec. 2021). Number: 1, p. 21. ISSN: 2662-1991. DOI: 10.1186/s43074-021-00043-z. URL: https://photoniX.springeropen.com/articles/10.1186/s43074-021-00043-z (visited on 03/09/2022).

[76] Loreta A. Muscarella et al. "Nanopatterning of Perovskite Thin Films for Enhanced and Directional Light Emission". en. In: *ACS Appl. Mater. Interfaces* 14.33 (Aug. 2022). Number: 33, pp. 38067–38076. ISSN: 1944-8244, 1944-8252. DOI: 10.1021/acsami.2c09643. URL: https://pubs.acs.org/doi/10.1021/acsami.2c09643 (visited on 09/02/2022).

[77] Leonid Yu. Beliaev et al. "Photoluminescence control by hyperbolic metamaterials and metasurfaces: a review". en. In: *OEA* 4.8 (2021). Number: 8, pp. 210031–210031. ISSN: 2096-4579. DOI: 10.29026/oea.2021.210031.

URL: http://www.oejournal.org/article/doi/10.29026/oea.2021.210031 (visited on 09/07/2021).

[78] Vincenzo Ardizzone et al. "Emerging 2D materials for room-temperature polaritonics". en. In: *Nanophotonics* 8.9 (July 2019). Number: 9, pp. 1547–1558. ISSN: 2192-8614. DOI: 10.1515/nanoph-2019-0114. URL: https://www.degruyter.com/document/doi/10.1515/nanoph-2019-0114/html (visited on 09/07/2021).

[79] Kirill R. Safronov et al. "Efficient Emission Outcoupling from Perovskite Lasers into Highly Directional and Long-Propagation-Length Bloch Surface Waves". en. In: *Laser & Photonics Reviews* 16.6 (June 2022). Number: 6, p. 2100728. ISSN: 1863-8880, 1863-8899. DOI: 10.1002/lpor.202100728. URL: https://onlinelibrary.wiley.com/doi/10.1002/lpor.202100728 (visited on 09/02/2022).

[80] Cuo Wu et al. "Room-temperature on-chip orbital angular momentum single-photon sources". en. In: *Sci. Adv.* 8.2 (Jan. 2022). Number: 2, eabk3075. ISSN: 2375-2548. DOI: 10.1126/sciadv.abk3075. URL: https://www.science.org/doi/10.1126/sciadv.abk3075 (visited on 03/28/2022).

[81] Richard Waltrich et al. "High-purity single photons obtained with moderate-NA optics from SiV center in nanodiamonds on a bullseye antenna". en. In: *New J. Phys.* 23.11 (Nov. 2021). Number: 11, p. 113022. ISSN: 1367-2630. DOI: 10.1088/1367-2630/ac33f3. URL: https://iopscience.iop.org/article/10.1088/1367-2630/ac33f3 (visited on 03/09/2022).

[82] P. Lombardi et al. "Photostable Molecules on Chip: Integrated Sources of Nonclassical Light". en. In: *ACS Photonics* 5.1 (Jan. 2018). Number: 1, pp. 126–132. ISSN: 2330-4022, 2330-4022. DOI: 10.1021/acsphotonics.7b00521. URL: https://pubs.acs.org/doi/10.1021/acsphotonics.7b00521 (visited on 09/30/2020).

[83] Yueyang Chen et al. “Deterministic Positioning of Colloidal Quantum Dots on Silicon Nitride Nanobeam Cavities”. en. In: *Nano Lett.* 18.10 (Oct. 2018). Number: 10, pp. 6404–6410. ISSN: 1530-6984, 1530-6992. DOI: 10.1021/acs.nanolett.8b02764. URL: https://pubs.acs.org/doi/10.1021/acs.nanolett.8b02764 (visited on 03/09/2022).

[84] Luca Sapienza et al. “Nanoscale optical positioning of single quantum dots for bright and pure single-photon emission”. en. In: *Nature Communications* 6.1 (July 2015). Number: 1 Publisher: Nature Publishing Group, p. 7833. ISSN: 2041-1723. DOI: 10.1038/ncomms8833. URL: https://www.nature.com/articles/ncomms8833 (visited on 09/11/2020).

[85] Alexander Eich et al. “Single-Photon Emission from Individual Nanophotonic-Integrated Colloidal Quantum Dots”. In: *ACS Photonics* 9.2 (Feb. 2022). Publisher: American Chemical Society, pp. 551–558. DOI: 10.1021/acsphotonics.1c01493. URL: https://doi.org/10.1021/acsphotonics.1c01493 (visited on 03/31/2023).

[86] Inhee Chung, Ken T. Shimizu, and Moungi G. Bawendi. “Room temperature measurements of the 3D orientation of single CdSe quantum dots using polarization microscopy”. en. In: *Proc. Natl. Acad. Sci. U.S.A.* 100.2 (Jan. 2003). Number: 2, pp. 405–408. ISSN: 0027-8424, 1091-6490. DOI: 10.1073/pnas.0133507100. URL: https://pnas.org/doi/full/10.1073/pnas.0133507100 (visited on 08/25/2022).

[87] Anton Matthijs Berghuis et al. “Light–Matter Coupling Strength Controlled by the Orientation of Organic Crystals in Plasmonic Cavities”. en. In: *J. Phys. Chem. C* 124.22 (June 2020). Number: 22, pp. 12030–12038. ISSN: 1932-7447, 1932-7455. DOI: 10.1021/acs.jpcc.0c00692. URL: https://pubs.acs.org/doi/10.1021/acs.jpcc.0c00692 (visited on 09/02/2022).

[88] Graham Gibson et al. “Free-space information transfer using light beams carrying orbital angular momentum”. en. In: (2004), p. 9.

[89] Nippon Telegraph and Telephone Corporation. *NTT successfully demonstrates 100 Gbps wireless transmission using a new principle (OAM multiplexing) as a world's first*. en. URL: http://www.ntt.co.jp/news2018/1805e/180515a.html (visited on 10/14/2021).

[90] Alois Mair et al. “Entanglement of the orbital angular momentum states of photons”. en. In: *Nature* 412.6844 (July 2001). Number: 6844 Publisher: Nature Publishing Group, pp. 313–316. ISSN: 1476-4687. DOI: 10.1038/35085529. URL: https://www.nature.com/articles/35085529 (visited on 04/01/2023).

[91] Gabriel Molina-Terriza, Juan P. Torres, and Lluis Torner. “Twisted photons”. en. In: *Nature Phys* 3.5 (May 2007). Number: 5 Publisher: Nature Publishing Group, pp. 305–310. ISSN: 1745-2481. DOI: 10.1038/nphys607. URL: https://www.nature.com/articles/nphys607 (visited on 04/01/2023).

[92] Manuel Erhard et al. “Twisted photons: new quantum perspectives in high dimensions”. en. In: *Light Sci Appl* 7.3 (Mar. 2018). Number: 3, pp. 17146–17146. ISSN: 2047-7538. DOI: 10.1038/lsa.2017.146. URL: http://www.nature.com/articles/lsa2017146 (visited on 04/25/2021).

[93] Yijie Shen et al. “Optical vortices 30 years on: OAM manipulation from topological charge to multiple singularities”. en. In: *Light Sci Appl* 8.1 (Dec. 2019), p. 90. ISSN: 2047-7538. DOI: 10.1038/s41377-019-0194-2. URL: http://www.nature.com/articles/s41377-019-0194-2 (visited on 10/26/2020).

[94] L. Paterson et al. “Controlled Rotation of Optically Trapped Microscopic Particles”. In: *Science* 292.5518 (May 2001). Publisher: American Association for the Advancement of Science, pp. 912–914. DOI: 10.1126/science.

1058591. URL: https://www-science-org.ezproxy.biblio.polito.it/doi/10.1126/science.1058591 (visited on 04/01/2023).

[95] Severin Fürhapter et al. "Spiral phase contrast imaging in microscopy". eng. In: *Opt Express* 13.3 (Feb. 2005), pp. 689–694. ISSN: 1094-4087. DOI: 10.1364/opex.13.000689.

[96] J. Arlt and K. Dholakia. "Generation of high-order Bessel beams by use of an axicon". en. In: *Optics Communications* 177.1 (Apr. 2000), pp. 297–301. ISSN: 0030-4018. DOI: 10.1016/S0030-4018(00)00572-1. URL: https://www.sciencedirect.com/science/article/pii/S0030401800005721 (visited on 04/01/2023).

[97] N. R. Heckenberg et al. "Generation of optical phase singularities by computer-generated holograms". EN. In: *Opt. Lett., OL* 17.3 (Feb. 1992). Publisher: Optica Publishing Group, pp. 221–223. ISSN: 1539-4794. DOI: 10.1364/OL.17.000221. URL: https://opg.optica.org/ol/abstract.cfm?uri=ol-17-3-221 (visited on 04/01/2023).

[98] Mark T. Gruneisen et al. "Holographic generation of complex fields with spatial light modulators: application to quantum key distribution". EN. In: *Appl. Opt., AO* 47.4 (Feb. 2008). Publisher: Optica Publishing Group, A32–A42. ISSN: 2155-3165. DOI: 10.1364/AO.47.000A32. URL: https://opg.optica.org/ao/abstract.cfm?uri=ao-47-4-A32 (visited on 04/01/2023).

[99] Ebrahim Karimi et al. "Efficient generation and sorting of orbital angular momentum eigenmodes of light by thermally tuned q-plates". In: *Appl. Phys. Lett.* 94.23 (June 2009). Publisher: American Institute of Physics, p. 231124. ISSN: 0003-6951. DOI: 10.1063/1.3154549. URL: https://aip-scitation-org.ezproxy.biblio.polito.it/doi/full/10.1063/1.3154549 (visited on 04/01/2023).

[100] Amir Arbabi et al. “Dielectric metasurfaces for complete control of phase and polarization with subwavelength spatial resolution and high transmission”. en. In: *Nature Nanotech* 10.11 (Nov. 2015). Number: 11 Publisher: Nature Publishing Group, pp. 937–943. ISSN: 1748-3395. DOI: 10.1038/nnano.2015.186. URL: https://www.nature.com/articles/nnano.2015.186 (visited on 04/01/2023).

[101] Ugo Stella et al. “Vortex Beam Generation by Spin-Orbit Interaction with Bloch Surface Waves”. In: *ACS Photonics* 7.3 (2020), pp. 774–783. DOI: 10.1021/acsphotonics.9b01625. URL: https://doi.org/10.1021/acsphotonics.9b01625.

[102] Ugo Stella et al. “Enhanced Directional Light Emission Assisted by Resonant Bloch Surface Waves in Circular Cavities”. In: *ACS Photonics* 6.8 (2019), pp. 2073–2082. DOI: 10.1021/acsphotonics.9b00570. URL: https://doi.org/10.1021/acsphotonics.9b00570.

[103] Patrice Genevet et al. “Recent advances in planar optics: from plasmonic to dielectric metasurfaces”. In: *Optica* 4.1 (Jan. 2017), pp. 139–152. DOI: 10.1364/OPTICA.4.000139. URL: https://opg.optica.org/optica/abstract.cfm?URI=optica-4-1-139.

[104] Alexander V. Kildishev, Alexandra Boltasseva, and Vladimir M. Shalaev. “Planar Photonics with Metasurfaces”. In: *Science* 339.6125 (Mar. 2013). Publisher: American Association for the Advancement of Science, p. 1232009. DOI: 10.1126/science.1232009. URL: https://www-science-org.ezproxy.biblio.polito.it/doi/full/10.1126/science.1232009 (visited on 03/17/2023).

[105] Nanfang Yu et al. “Light Propagation with Phase Discontinuities: Generalized Laws of Reflection and Refraction”. In: *Science* 334.6054 (Oct. 2011). Publisher: American Association for the Advancement of Science, pp. 333–

337. DOI: 10.1126/science.1210713. URL: https://www-science-org.ezproxy.biblio.polito.it/doi/10.1126/science.1210713 (visited on 03/16/2023).

[106] Lingling Huang et al. "Dispersionless Phase Discontinuities for Controlling Light Propagation". In: *Nano Lett.* 12.11 (Nov. 2012). Publisher: American Chemical Society, pp. 5750–5755. ISSN: 1530-6984. DOI: 10.1021/nl303031j. URL: https://doi.org/10.1021/nl303031j (visited on 08/25/2021).

[107] Lingling Huang et al. "Helicity dependent directional surface plasmon polariton excitation using a metasurface with interfacial phase discontinuity". en. In: *Light Sci Appl* 2.3 (Mar. 2013). Bandiera_abtest: a Cg_type: Nature Research Journals Number: 3 Primary_atype: Research Publisher: Nature Publishing Group, e70–e70. ISSN: 2047-7538. DOI: 10.1038/lsa.2013.26. URL: http://www.nature.com/articles/lsa201326 (visited on 08/25/2021).

[108] Niccolò Marcucci. *Repository for Lumerical and multilayer design codes.* 2020. URL: https://github.com/Niccolo-Marcucci/Lumerical-Objects.

[109] Igor Aharonovich, Dirk Englund, and Milos Toth. "Solid-state single-photon emitters". en. In: *Nature Photon* 10.10 (Oct. 2016). Number: 10 Publisher: Nature Publishing Group, pp. 631–641. ISSN: 1749-4893. DOI: 10.1038/nphoton.2016.186. URL: https://www.nature.com/articles/nphoton.2016.186 (visited on 04/02/2023).

[110] Juan C. Loredo et al. "Scalable performance in solid-state single-photon sources". EN. In: *Optica, OPTICA* 3.4 (Apr. 2016). Publisher: Optica Publishing Group, pp. 433–440. ISSN: 2334-2536. DOI: 10.1364/OPTICA.3.000433. URL: https://opg.optica.org/optica/abstract.cfm?uri=optica-3-4-433 (visited on 04/02/2023).

[111] N. Somaschi et al. “Near-optimal single-photon sources in the solid state”. en. In: *Nature Photon* 10.5 (May 2016). Number: 5 Publisher: Nature Publishing Group, pp. 340–345. ISSN: 1749-4893. DOI: 10.1038/nphoton.2016.23. URL: https://www.nature.com/articles/nphoton.2016.23 (visited on 04/02/2023).

[112] Sumin Choi et al. “Single photon emission from ZnO nanoparticles”. In: *Appl. Phys. Lett.* 104.26 (June 2014). Publisher: American Institute of Physics, p. 261101. ISSN: 0003-6951. DOI: 10.1063/1.4872268. URL: https://aip-scitation-org.ezproxy.biblio.polito.it/doi/full/10.1063/1.4872268 (visited on 04/02/2023).

[113] A. Sipahigil et al. “Indistinguishable Photons from Separated Silicon-Vacancy Centers in Diamond”. In: *Phys. Rev. Lett.* 113.11 (Sept. 2014). Publisher: American Physical Society, p. 113602. DOI: 10.1103/PhysRevLett.113.113602. URL: https://link.aps.org/doi/10.1103/PhysRevLett.113.113602 (visited on 04/02/2023).

[114] A. Sipahigil et al. “Quantum Interference of Single Photons from Remote Nitrogen-Vacancy Centers in Diamond”. In: *Phys. Rev. Lett.* 108.14 (Apr. 2012). Publisher: American Physical Society, p. 143601. DOI: 10.1103/PhysRevLett.108.143601. URL: https://link.aps.org/doi/10.1103/PhysRevLett.108.143601 (visited on 04/02/2023).

[115] V. M. Acosta et al. “Dynamic Stabilization of the Optical Resonances of Single Nitrogen-Vacancy Centers in Diamond”. In: *Phys. Rev. Lett.* 108.20 (May 2012). Publisher: American Physical Society, p. 206401. DOI: 10.1103/PhysRevLett.108.206401. URL: https://link.aps.org/doi/10.1103/PhysRevLett.108.206401 (visited on 04/02/2023).

[116] Igor Aharonovich and Elke Neu. “Diamond Nanophotonics”. en. In: *Advanced Optical Materials* 2.10 (2014), pp. 911–928. ISSN: 2195-1071. DOI:

10.1002/adom.201400189. URL: https://onlinelibrary.wiley.com/doi/abs/10.1002/adom.201400189 (visited on 04/02/2023).

[117] Xiao-Liu Chu, Stephan Götzinger, and Vahid Sandoghdar. "A single molecule as a high-fidelity photon gun for producing intensity-squeezed light". en. In: *Nature Photon* 11.1 (Jan. 2017). Number: 1 Publisher: Nature Publishing Group, pp. 58–62. ISSN: 1749-4893. DOI: 10.1038/nphoton.2016.236. URL: https://www.nature.com/articles/nphoton.2016.236 (visited on 04/02/2023).

[118] Axel Kuhn, Markus Hennrich, and Gerhard Rempe. "Deterministic Single-Photon Source for Distributed Quantum Networking". In: *Phys. Rev. Lett.* 89.6 (July 2002). Publisher: American Physical Society, p. 067901. DOI: 10.1103/PhysRevLett.89.067901. URL: https://link.aps.org/doi/10.1103/PhysRevLett.89.067901 (visited on 04/02/2023).

[119] Xuedan Ma et al. "Room-temperature single-photon generation from solitary dopants of carbon nanotubes". en. In: *Nature Nanotech* 10.8 (Aug. 2015). Number: 8 Publisher: Nature Publishing Group, pp. 671–675. ISSN: 1748-3395. DOI: 10.1038/nnano.2015.136. URL: https://www.nature.com/articles/nnano.2015.136 (visited on 04/02/2023).

[120] A. Jeantet et al. "Widely Tunable Single-Photon Source from a Carbon Nanotube in the Purcell Regime". In: *Phys. Rev. Lett.* 116.24 (June 2016). Publisher: American Physical Society, p. 247402. DOI: 10.1103/PhysRevLett.116.247402. URL: https://link.aps.org/doi/10.1103/PhysRevLett.116.247402 (visited on 04/02/2023).

[121] Shuliang Ren, Qinghai Tan, and Jun Zhang. "Review on the quantum emitters in two-dimensional materials". en. In: *J. Semicond.* 40.7 (July 2019). Publisher: Chinese Institute of Electronics, p. 071903. ISSN: 1674-4926. DOI:

10.1088/1674-4926/40/7/071903. URL: https://dx.doi.org/10.1088/1674-4926/40/7/071903 (visited on 04/02/2023).

[122] Milos Toth and Igor Aharonovich. "Single Photon Sources in Atomically Thin Materials". en. In: *Annu. Rev. Phys. Chem.* 70.1 (June 2019), pp. 123–142. ISSN: 0066-426X, 1545-1593. DOI: 10.1146/annurev-physchem-042018-052628. URL: https://www.annualreviews.org/doi/10.1146/annurev-physchem-042018-052628 (visited on 04/02/2023).

[123] Kin Fai Mak et al. "Atomically Thin ${\mathrm{MoS}}_{2}$: A New Direct-Gap Semiconductor". In: *Phys. Rev. Lett.* 105.13 (Sept. 2010). Publisher: American Physical Society, p. 136805. DOI: 10.1103/PhysRevLett.105.136805. URL: https://link.aps.org/doi/10.1103/PhysRevLett.105.136805 (visited on 04/02/2023).

[124] Andrea Splendiani et al. "Emerging Photoluminescence in Monolayer MoS2". In: *Nano Lett.* 10.4 (Apr. 2010). Publisher: American Chemical Society, pp. 1271–1275. ISSN: 1530-6984. DOI: 10.1021/nl903868w. URL: https://doi.org/10.1021/nl903868w (visited on 04/02/2023).

[125] Alexey Chernikov et al. "Exciton Binding Energy and Nonhydrogenic Rydberg Series in Monolayer ${\mathrm{WS}}_{2}$". In: *Phys. Rev. Lett.* 113.7 (Aug. 2014). Publisher: American Physical Society, p. 076802. DOI: 10.1103/PhysRevLett.113.076802. URL: https://link.aps.org/doi/10.1103/PhysRevLett.113.076802 (visited on 04/02/2023).

[126] Oliver Iff et al. "Purcell-Enhanced Single Photon Source Based on a Deterministically Placed WSe2 Monolayer Quantum Dot in a Circular Bragg Grating Cavity". In: *Nano Lett.* (May 2021). Publisher: American Chemical Society. ISSN: 1530-6984. DOI: 10.1021/acs.nanolett.1c00978. URL: https://doi.org/10.1021/acs.nanolett.1c00978 (visited on 05/30/2021).

[127] Oliver Iff et al. “Deterministic coupling of quantum emitters in WSe_2 monolayers to plasmonic nanocavities”. EN. In: *Opt. Express, OE* 26.20 (Oct. 2018). Publisher: Optical Society of America, pp. 25944–25951. ISSN: 1094-4087. DOI: 10.1364/OE.26.025944. URL: https://www.osapublishing.org/oe/abstract.cfm?uri=oe-26-20-25944 (visited on 06/08/2021).

[128] Myron J. Rand and James F. Roberts. “Preparation and Properties of Thin Film Boron Nitride”. en. In: *J. Electrochem. Soc.* 115.4 (Apr. 1968). Publisher: IOP Publishing, p. 423. ISSN: 1945-7111. DOI: 10.1149/1.2411238. URL: https://iopscience.iop.org/article/10.1149/1.2411238/meta (visited on 04/02/2023).

[129] Yumeng Shi et al. “Synthesis of Few-Layer Hexagonal Boron Nitride Thin Film by Chemical Vapor Deposition”. In: *Nano Lett.* 10.10 (Oct. 2010). Publisher: American Chemical Society, pp. 4134–4139. ISSN: 1530-6984. DOI: 10.1021/nl1023707. URL: https://doi.org/10.1021/nl1023707 (visited on 04/02/2023).

[130] Kenji Watanabe, Takashi Taniguchi, and Hisao Kanda. “Direct-bandgap properties and evidence for ultraviolet lasing of hexagonal boron nitride single crystal”. en. In: *Nature Mater* 3.6 (June 2004). Number: 6 Publisher: Nature Publishing Group, pp. 404–409. ISSN: 1476-4660. DOI: 10.1038/nmat1134. URL: https://www.nature.com/articles/nmat1134 (visited on 04/02/2023).

[131] H. Tracy Hall. “Ultra-High-Pressure, High-Temperature Apparatus: the “Belt””. In: *Review of Scientific Instruments* 31.2 (Feb. 1960). Publisher: American Institute of Physics, pp. 125–131. ISSN: 0034-6748. DOI: 10.1063/1.1716907. URL: https://aip-scitation-org.ezproxy.biblio.polito.it/doi/10.1063/1.1716907 (visited on 04/02/2023).

[132] Jun Yin et al. "Aligned Growth of Hexagonal Boron Nitride Monolayer on Germanium". In: *Small* 11.40 (2015), pp. 5375–5380. ISSN: 1613-6829. DOI: 10.1002/smll.201501439. URL: https://onlinelibrary.wiley.com/doi/abs/10.1002/smll.201501439 (visited on 04/02/2023).

[133] Kanika Sharma and Nitin K. Puri. "Enhanced Electrochemical Performance of Hydrothermally Exfoliated Hexagonal Boron Nitride Nanosheets for Applications in Electrochemistry". en. In: *J. Electrochem. Soc.* 168.5 (May 2021). Publisher: IOP Publishing, p. 056512. ISSN: 1945-7111. DOI: 10.1149/1945-7111/abfe41. URL: https://dx.doi.org/10.1149/1945-7111/abfe41 (visited on 04/02/2023).

[134] J. Marcelo J. Lopes. "Synthesis of hexagonal boron nitride: From bulk crystals to atomically thin films". en. In: *Progress in Crystal Growth and Characterization of Materials* 67.2 (May 2021), p. 100522. ISSN: 0960-8974. DOI: 10.1016/j.pcrysgrow.2021.100522. URL: https://www.sciencedirect.com/science/article/pii/S0960897421000012 (visited on 04/02/2023).

[135] Nicholas V. Proscia et al. "Near-deterministic activation of room-temperature quantum emitters in hexagonal boron nitride". EN. In: *Optica, OPTICA* 5.9 (Sept. 2018). Publisher: Optical Society of America, pp. 1128–1134. ISSN: 2334-2536. DOI: 10.1364/OPTICA.5.001128. URL: https://www-osapublishing-org.ezproxy.biblio.polito.it/optica/abstract.cfm?uri=optica-5-9-1128 (visited on 07/12/2021).

[136] Joshua Ziegler et al. "Deterministic Quantum Emitter Formation in Hexagonal Boron Nitride via Controlled Edge Creation". In: *Nano Lett.* 19.3 (Mar. 2019). Publisher: American Chemical Society, pp. 2121–2127. ISSN: 1530-6984. DOI: 10.1021/acs.nanolett.9b00357. URL: https://doi.org/10.1021/acs.nanolett.9b00357 (visited on 09/15/2021).

[137] Xiaohui Xu et al. "Creating Quantum Emitters in Hexagonal Boron Nitride Deterministically on Chip-Compatible Substrates". In: *Nano Lett.* 21.19 (Oct. 2021). Publisher: American Chemical Society, pp. 8182–8189. ISSN: 1530-6984. DOI: 10.1021/acs.nanolett.1c02640. URL: https://doi.org/10.1021/acs.nanolett.1c02640 (visited on 07/12/2022).

[138] M. Fischer et al. "Controlled generation of luminescent centers in hexagonal boron nitride by irradiation engineering". In: *Science Advances* 7.8 (Feb. 2021). Publisher: American Association for the Advancement of Science, eabe7138. DOI: 10.1126/sciadv.abe7138. URL: https://www-science-org.ezproxy.biblio.polito.it/doi/10.1126/sciadv.abe7138 (visited on 01/18/2023).

[139] Nai-Jie Guo et al. "Generation of Spin Defects by Ion Implantation in Hexagonal Boron Nitride". In: *ACS Omega* 7.2 (Jan. 2022). Publisher: American Chemical Society, pp. 1733–1739. DOI: 10.1021/acsomega.1c04564. URL: https://doi.org/10.1021/acsomega.1c04564 (visited on 04/28/2022).

[140] Evgenii Glushkov et al. "Engineering Optically Active Defects in Hexagonal Boron Nitride Using Focused Ion Beam and Water". In: *ACS Nano* 16.3 (Mar. 2022). Publisher: American Chemical Society, pp. 3695–3703. ISSN: 1936-0851. DOI: 10.1021/acsnano.1c07086. URL: https://doi.org/10.1021/acsnano.1c07086 (visited on 04/28/2022).

[141] Michael. T. Postek. "An approach to the reduction of hydrocarbon contamination in the scanning electron microscope". en. In: *Scanning* 18.4 (1996). _eprint: https://onlinelibrary.wiley.com/doi/pdf/10.1002/sca.1996.4950180402, pp. 269–274. ISSN: 1932-8745. DOI: 10.1002/sca.1996.4950180402. URL: https://onlinelibrary.wiley.com/doi/abs/10.1002/sca.1996.4950180402 (visited on 04/03/2023).

[142] Andras E. Vladar, Michael T. Postek Jr., and Ronald Vane. "Active monitoring and control of electron-beam-induced contamination". en. In: ed. by Neal T. Sullivan. Santa Clara, CA, Aug. 2001, p. 835. DOI: 10.1117/12.436724. URL: http://proceedings.spiedigitallibrary.org/proceeding.aspx?doi=10.1117/12.436724 (visited on 04/03/2023).

[143] A Vladar and M Postek. "Electron Beam-Induced Sample Contamination in the SEM". en. In: *MAM* 11.S02 (Aug. 2005). ISSN: 1431-9276, 1435-8115. DOI: 10.1017/S1431927605507785. URL: https://academic.oup.com/mam/article/11/S02/764/6915203 (visited on 04/03/2023).

[144] Andres Castellanos-Gomez et al. "Deterministic transfer of two-dimensional materials by all-dry viscoelastic stamping". en. In: *2D Mater.* 1.1 (Apr. 2014). Publisher: IOP Publishing, p. 011002. ISSN: 2053-1583. DOI: 10.1088/2053-1583/1/1/011002. URL: https://dx.doi.org/10.1088/2053-1583/1/1/011002 (visited on 04/03/2023).

[145] Yuto Anzai et al. "Broad range thickness identification of hexagonal boron nitride by colors". en. In: *Appl. Phys. Express* 12.5 (Apr. 2019). Publisher: IOP Publishing, p. 055007. ISSN: 1882-0786. DOI: 10.7567/1882-0786/ab0e45. URL: https://doi.org/10.7567/1882-0786/ab0e45 (visited on 06/28/2021).

[146] Satoru Masubuchi et al. "Deep-learning-based image segmentation integrated with optical microscopy for automatically searching for two-dimensional materials". en. In: *npj 2D Mater Appl* 4.1 (Mar. 2020). Number: 1 Publisher: Nature Publishing Group, pp. 1–9. ISSN: 2397-7132. DOI: 10.1038/s41699-020-0137-z. URL: https://www.nature.com/articles/s41699-020-0137-z (visited on 03/15/2022).

[147] Riccardo Frisenda et al. "Recent progress in the assembly of nanodevices and van der Waals heterostructures by deterministic placement of 2D materials".

en. In: *Chemical Society Reviews* 47.1 (2018). Publisher: Royal Society of Chemistry, pp. 53–68. DOI: 10.1039/C7CS00556C. URL: https://pubs.rsc.org/en/content/articlelanding/2018/cs/c7cs00556c (visited on 04/03/2023).

This Ph.D. thesis has been typeset by means of the TEX-system facilities. The typesetting engine was pdfLATEX. The document class was `toptesi`, by Claudio Beccari, with option `tipotesi=scudo`. This class is available in every up-to-date and complete TEX-system installation.